MANUFACTURING ^{48}V TARGET FOR NEUTRON REACTION CROSS-SECTION MEASUREMENTS

By

Scott David Essenmacher

A DISSERTATION

Submitted to
Michigan State University
in partial fulfillment of the requirements
for the degree of

Chemistry – Doctor of Philosophy

2023

ABSTRACT

Many areas in nuclear science utilize simulation models of neutron reaction networks to predict the outcomes of chaotic events, such as stellar nucleosynthesis and nuclear detonations. The fidelity of these predictions can be improved by obtaining accurate nuclear reaction cross-section data. Much of the cross-section data on radioactive nuclei has not been measured before and performing these measurements would be beneficial for end users of evaluated nuclear data. Obtaining accurate nuclear reaction measurements of ^{48}V, a radioisotope of V ($t_{1/2}$ = 15.974(3) days), would be advantageous for the United States Stockpile Stewardship program as that data can enhance the fidelity of simulation models on neutron reaction networks and ultimately lead to better validation of the United States nuclear stockpile.

Although there are many different types of nuclear reactions that can occur, the two reactions that dominate the destruction pathway for ^{48}V with low energy neutrons are the ^{48}V(n, γ)^{49}V and ^{48}V(n, p)^{49}V reactions. Measuring total cross-section for the ^{48}V(n, γ)^{49}V reaction can be accomplished using the activation method, while a direct measurement technique that allows for the detection of outgoing protons and neutron energy (via neutron time-of-flight measurements) would be the best method for determining the ^{48}V(n, p)^{49}V cross-section. Both techniques require the fabrication of a stationary ^{48}V target (containing mCi quantities of ^{48}V) that meets specific purity, geometric, and stability requirements. In general, these targets need to be physically stable during the irradiation, free of impurities that would be detrimental for the measurement, uniform, and of the appropriate thickness to allow for accurate measurements to be made. The most important requirement for the target being measured via the activation method is the isotopic purity of the ^{48}V, specifically with respect to ^{49}V (>10^4 atoms of ^{48}V/atom of ^{49}V), while the ^{48}V target for direct neutron-induced charged particle reaction measurements must be

thin and uniform to minimize the attenuation of outgoing protons and the measurement time and error.

To produce ^{48}V in high isotopic purity and manufacture a thin and uniform ^{48}V target, an isotope production method and a target fabrication method must be identified. Two different isotope production methods were investigated to discern the best method for producing ^{48}V in high isotopic purity relative to ^{49}V: a conventional α irradiation of natural Sc foil method and a novel method called isotope harvesting that focused on harvesting ^{48}Cr from the aqueous beam dump at the Facility for Rare Isotope Beams and setting up a ^{48}Cr/^{48}V generator for pure ^{48}V production. Isotope harvesting was found to be the best method for producing mCi quantities of ^{48}V that meet or exceed the purity requirements for a ^{48}V target to be used in neutron activation studies. Meanwhile, two ^{48}V target manufacturing techniques were also examined: a conventional electrodeposition technique and a novel method called microjet printing. The electrodeposition method was found to be extremely pH dependent and would be challenging to use to produce a radioactive target, while microjet printing has the highest potential at being the most effective method for fabricating thin and relatively uniform ^{48}V targets. Overall, a recommended thin ^{48}V target manufacturing protocol was identified and covers all the steps from the in the process to produce mCi levels of ^{48}V in high isotopic purity relative to ^{49}V along with those necessary for the fabrication of a thin and uniform ^{48}V target for neutron-induced reaction studies.

ACKNOWLEDGEMENTS

Much of the work in this dissertation would not be possible without the help and support of many people to whom I am indebted to. I would like to start by thanking my advisor, Greg, for providing me with the opportunity to do my research at Michigan State University and advising me on my graduate school journey. I would also like to thank my committee members for their valuable constructive feedback on my work from time to time.

Being a part of the isotope harvesting group gave me the opportunity to refine my scientific acumen through many experiences with excellent people and I am grateful to have worked alongside them. I would really like to thank a few of these people in particular. Chloe, Samridhi, and Vlad, thank you for assisting me with various experiments. Especially those that lasted many, many hours or had a short turnaround. Kathi also helped with some of those experiments, and I learned many skills pertinent to radiochemistry from her. She also read and provided feedback on this manuscript. I would like to thank her for all that and our many discussions on various topics. Chirag and I did many experiments early on together and had numerous conversations during my time at Michigan State. I learned a lot from those experiences and really appreciated our conversations on topics involving nuclear chemistry and nuclear science in general. He also found some time in his busy schedule to read and provide comments on this manuscript. I thank Chirag for that and for teaching me how to be a better scientist overall.

Some of the work in this dissertation required working with groups outside of Michigan State and I would like to thank the people in those groups as well. I am grateful for the help Graham and his group, particularly Tony and John, at the University of Notre Dame provided by performing the scandium foil irradiation. I would also like to thank the many scientists, postdocs, and laboratory personnel in the Chemistry and Physics Divisions for helping me with various tasks

at the Los Alamos National Laboratory. I am especially thankful for Hye Young, Etienne, Veronika, and Thanos for taking time out of their day to guide me while I performed work at a national lab. I learned a lot from that experience.

Finally, none of this would even be possible without the continuous support from my family and friends. They have been supporting and encouraging me from the first day and I am really grateful for them.

TABLE OF CONTENTS

LIST OF TABLES

LIST OF FIGURES

CHAPTER 1: INTRODUCTION

Unstable nuclides are important for a wide variety of fields, including fundamental chemical and physical sciences, nuclear medicine, geology, and astrophysics. Some crucial radionuclides include ^{238}Pu as a source for radioisotope thermoelectric generators for United States spacecraft [1], ^{7}Be and ^{137}Cs as radiotracers to monitor soil erosion and deposition [2], ^{18}F, ^{99}Tc, and ^{68}Ga for medical diagnostics [3–5], and ^{131}I, ^{223}Ra, and ^{177}Lu for cancer treatments [6–8]. Research on radionuclides, their applications, and production methods is ongoing. Each application requires radionuclides of a certain chemical and/or isotopic purity and in a particular phase (typically liquid or solid) with the capability of being produced in sufficient quantities. This dissertation focuses on the examination of the necessary protocols to produce ^{48}V ($t_{1/2}$ = 15.974(3) days [9]) in a solid form with excellent chemical and isotopic purity. No accurate neutron-induced reaction cross-section data for ^{48}V is currently available and having the capability to obtain this data is important for various areas of fundamental and applied nuclear science.

1.1 Nuclear Data Needs for ^{48}V

Obtaining accurate reaction cross-section data would improve the fidelity of simulation models and predictive calculations used to simulate nuclear reaction networks for applications in fundamental and applied nuclear science [10–12]. A program that would benefit from accurate nuclear reaction cross-section measurements of ^{48}V is the Science-Based Stockpile Stewardship program, which is run by the Department of Energy's National Laboratories to monitor and maintain confidence in the United States nuclear weapons stockpile [13,14]. By enhancing the fidelity of simulation models for neutron reaction networks, the neutron flux in nuclear detonations can be more accurately predicted, leading to better validation of the United States nuclear stockpile [15].

The best method for obtaining highly accurate data on neutron reaction cross-sections is to perform direct measurements on stationary targets. In these measurements, both the outgoing reaction products and incident neutron energies (via neutron time-of-flight measurements) are measured. Thus, a function for a reaction cross-section in terms of incident neutron energy, also known as an excitation function, can be obtained. For total cross-sections, an alternative technique, the activation method, can be used to perform measurements on solid targets and requires less sophisticated equipment. Activation measurements with a radioactive target require inserting a neutron flux monitor with the target and measuring the activity in the target prior to and after the target is irradiated. The neutron flux monitor should be material that has a well-known neutron-induced reaction cross-section and would be used to determine the neutron flux the radioactive target was exposed to in a nuclear reactor. The combination of the neutron flux along with the initial and final target activities would be used to calculate the total cross-section for the reaction of interest.

Regardless of the measurement technique, the manufactured targets need to be free of any chemical and isotopic impurities that can significantly affect the experimental results [11,15]. This issue is exemplified by neutron capture reaction cross-section measurements performed on ^{90}Zr by the n_TOF collaboration, where reactions with even trace amounts (<0.01%) of impurities appeared in the measurements [16]. For experiments performed with the activation method, the presence of impurities becomes a problem if a neutron reaction produces a relatively long-lived radionuclide that is difficult to quantify. This is the case with the ^{48}V(n, γ)^{49}V reaction because the residual nucleus that is formed in this reaction, ^{49}V, is relatively long-lived ($t_{1/2}$ = 330(15) days [17]). Therefore, the ^{48}V in a target for neutron activation measurements must be high in isotopic purity with respect to ^{49}V.

So far, ^{48}V has no experimentally measured neutron reaction cross-sections. The activation method is a relatively simple experiment that allows for the measurement of a total reaction cross-section and the (n, γ) reaction cross-section is of high importance for stockpile stewardship science [15], so a major goal of this dissertation is to determine how to fabricate a ^{48}V target of high isotopic purity so that the ^{48}V(n, γ)^{49}V reaction cross-section can be accurately measured using the activation method. Meanwhile, theoretical values determined by Kelley et al. suggest that the ^{48}V(n, p)^{48}Ti cross-section should dominate the destruction pathway for low energy neutrons, as cross-section for the other major destruction channel in this energy window (<8 MeV), ^{48}V(n, γ)^{49}V, is expected to be roughly two orders of magnitude lower [18]. Measurements of neutron-induced charged particle reactions require detecting the prompt emission of outgoing charged particles, which can be easily attenuated and stopped within target material [19]. Based on these conditions, direct measurement studies of the (n, p) reaction on ^{48}V require the utilization of a thin ^{48}V target, which is a requirement that is not crucial for neutron activation measurements. As a result, ^{48}V targets should be thin and high in isotopic purity to allow for accurate measurements of (n, γ) and (n, p) reaction cross-sections.

The isotopic purity of ^{48}V for activation targets influences the precision of the measurement. To accurately estimate the quantity of ^{49}V that is produced during a week-long irradiation of a ^{48}V target containing 10^{11} atoms of ^{48}V with a flux of 10^{14} neutrons/s·cm^2 at the Missouri Research Reactor (MURR), the initial amount of ^{49}V, all the possible production and destruction pathways, the decay of ^{49}V, and all those same variables for any nuclide that can undergo a reaction to produce ^{49}V need to be considered. This would involve mapping out the full reaction network and the rate of change in the number of atoms of ^{49}V, $\frac{dN_{49V}}{dt}$, can be generalized as shown in the following set of equations on the next page:

$$\frac{dN_{49_V}(t,E)}{dt} = \alpha + \mathrm{B} + \Gamma + \Delta \quad (1.1)$$

$$\mathrm{A} = N_{48_V}(\mathrm{t},\mathrm{E})\Phi(t,E)\sigma_{(n,\gamma)}(E) + N_{49_{Cr}}(\mathrm{t},\mathrm{E})\Phi(t,E)\sigma_{(n,p)}(E) + N_{50_V}(\mathrm{t},\mathrm{E})\Phi(t,E)\sigma_{(n,2n)}(E) + \cdots \quad (1.2)$$

$$\mathrm{B} = \lambda_{49_{Cr}} N_{49_{Cr}}(t,E) \quad (1.3)$$

$$\Gamma = -N_{49_V}(\mathrm{t},\mathrm{E})\Phi(t,E)\sigma_{(n,\gamma)}(E) - N_{49_V}(\mathrm{t},\mathrm{E})\Phi(t,E)\sigma_{(n,p)}(E) - \mathbb{N}_{49_V}(\mathrm{t},\mathrm{E})\Phi(t,E)\sigma_{(n,np)}(E) - \cdots \quad (1.4)$$

$$\Delta = -\lambda_{49_V} N_{49_V}(t,E) \quad (1.5)$$

where the terms in A include all production channels for ^{49}V or reactions that lead to the production of ^{49}V, the terms in B include all destruction channels for ^{49}V or reactions with ^{49}V that produce another nuclide, N_i is the atoms of nuclide i, Φ is the neutron flux in neutrons/s·cm^2, σ_k is the cross-section for reaction k a target nuclide, λ_i is the decay constant for nuclide i, E is the energy of the incident neutrons, and t is the irradiation time. The following assumptions can be made to simplify the equation: ^{48}V and ^{49}V are the only nuclides present in the target at the start of the irradiation, the neutron flux is constant independent of time, and all terms beyond the first two in both the production channel and destruction channel contributions to the equation are negligible because they only become the more prominent reactions at high incident neutron energies (>10 MeV) [18] and most neutrons at MURR will be less than 10 MeV [20]. The result of these assumptions is both the ^{49}Cr decay term and the ^{49}V production channel term that depends on target ^{49}Cr atoms being present are zero, which simplifies Equation 1.1 to the following:

$$\frac{dN_{49_V}(t,E)}{dt} = N_{48_V}(\mathrm{t},\mathrm{E})\Phi(E)\sigma_{(n,\gamma)}(E) - N_{49_V}(\mathrm{t},\mathrm{E})\Phi(E)\left(\sigma_{(n,\gamma)}(E) + \sigma_{(n,p)}(E)\right) - \lambda_{49_V} N_{49_V}(t,E) \quad (1.6)$$

To obtain a rough estimate for how much ^{49}V impurity can be present in the target at the start of the irradiation for a ^{48}V(n, γ)^{49}V cross-section measurement with a precision of 10 barns, two more assumptions can be made. One is the second term in Equation 1.6 is negligible because the average cross-sections for the ^{49}V(n, γ)^{50}V and ^{49}V(n, p)^{49}Ti reactions respectively are about four and two orders of magnitude less than 10 barns. The other assumption is ^{48}V does not decay significantly

over the course of the irradiation and is independent of time (i.e. is treated as stable or non-radioactive). Applying these assumptions and integrating the simplified equation, results in the following [21]:

$$N_{49_V}(E) = \frac{N_{48_V}(E)\Phi(E)\sigma_{(n,\gamma)}(E)}{\lambda_{49_V}}\left(1 - e^{-\lambda_{49_V} t}\right) \quad (1.7)$$

where N_{49_V} is the atoms of ^{49}V produced. The function for the cross-section of the ^{48}V(n, γ)^{49}V reaction, $\sigma_{(n,\gamma)}(E)$, would be the total cross-section for that reaction over all neutron energies in MURR, σ_γ. Meanwhile, the average neutron flux, Φ, over all incident neutron energies can be used in place of the neutron flux function $\Phi(E)$. Applying these assumptions allows for the total number of ^{49}V atoms that can be produced with a one-week irradiation to be determined. Also, because a one-week irradiation is much shorter than the half-life of ^{49}V ($t_{1/2}$ = 330 days), the exponential term can be simplified using a Taylor series expansion where the third and ensuing terms are negligible. This results in the simplified equation of

$$N_{49_V} = N_{48_V}\Phi\sigma_\gamma \mathrm{t} \quad (1.8)$$

Assuming a cross-section of 10 barns (10^{-23} cm^2) and plugging in the previously mentioned values for N_{48_V}, Φ, and t, results in N_{49_V} = 6 x 10^7 atoms of ^{49}V. To confidently observe the produced ^{49}V quantity after the irradiation (assuming the limit of detection for ^{49}V when using a liquid scintillation counter is about 0.5 Bq or 2 x 10^7 atoms of ^{49}V), the initially present ^{49}V in the ^{48}V target must be less than 10^8 atoms. As such, any produced ^{48}V for neutron capture reaction studies performed via the activation method should have at least 10^4 atoms of ^{48}V per atom of ^{49}V to obtain a precision on the order of 10 barns in the total cross-section measurement.

If the ^{48}V(n, γ)^{49}V reaction has an actual total average cross-section of 100 barns, then the amount of ^{48}V needed to produce a sufficient quantity of ^{49}V over the course of a 1-week irradiation, assuming the assumptions described above are true, would be 0.2 μCi. More ^{48}V would

be required if the actual cross-section is lower than 100 barns (note that the theoretical cross-section for the neutron capture reaction ^{48}V with thermal neutrons of 0.025 eV is approximately 14 barns [22], but other values were chosen in these examples to highlight the differences in the required quantities and purities as far as the feasibility and resolution of the measurement are concerned). For example, 2 mCi of ^{48}V would be needed to measure a ^{48}V(n, γ)^{49}V reaction cross-section on the order of 10 millibarns. In this example, a resolution on the order of 1 millibarn or less would be desirable. To attain this resolution, the ^{48}V isotopic purity needs to be at least 10^8 atoms of ^{48}V per atom of ^{49}V. This suggests that even though a major goal for this dissertation work was to identify an isotope production method for ^{48}V that can produce ^{48}V with an isotopic purity of $>10^4$ atoms of ^{48}V/atom of ^{49}V, it would be ideal if this method could also produce mCi levels of ^{48}V with an isotopic purity of $>10^8$ atoms of ^{48}V/atom of ^{49}V.

1.2 Isotope Harvesting

The conventional method for producing ^{48}V involves irradiating both natural and enriched Ti foils with protons [23–25]. The ^{48}Ti(p, n)^{48}V reaction allows for the production of ^{48}V and has a cross-section peak of approximately 500 millibarns for incident proton energies around 11 MeV [26]. However, significant amounts of ^{49}V are co-produced as well, even with enriched ^{48}Ti foils. Enriched ^{48}Ti foils contain considerable amounts of ^{49}Ti (e.g. enriched $^{48}TiO_2$ from ISOFLEX USA contains 96.2% ^{48}Ti and 0.81% ^{49}Ti [27]). With the ^{49}Ti(p, n)^{49}V cross-section being approximately 500 millibarns for an incident proton energy of 6 MeV [28] and its excitation function having a theoretical peak of nearly 700 millibarns for about 10 MeV protons [29] (see Figure 1.1 on the next page, which includes this data along with additional experimental data from Johnson et al. [30] for the ^{49}V(p, n)^{48}V reaction), the ^{48}V produced during proton-irradiation of

enriched ^{48}Ti would encompass ~10^2 atoms of ^{48}V/atom of ^{49}V and not meet the required isotopic purity of the desired >10^4 ratio.

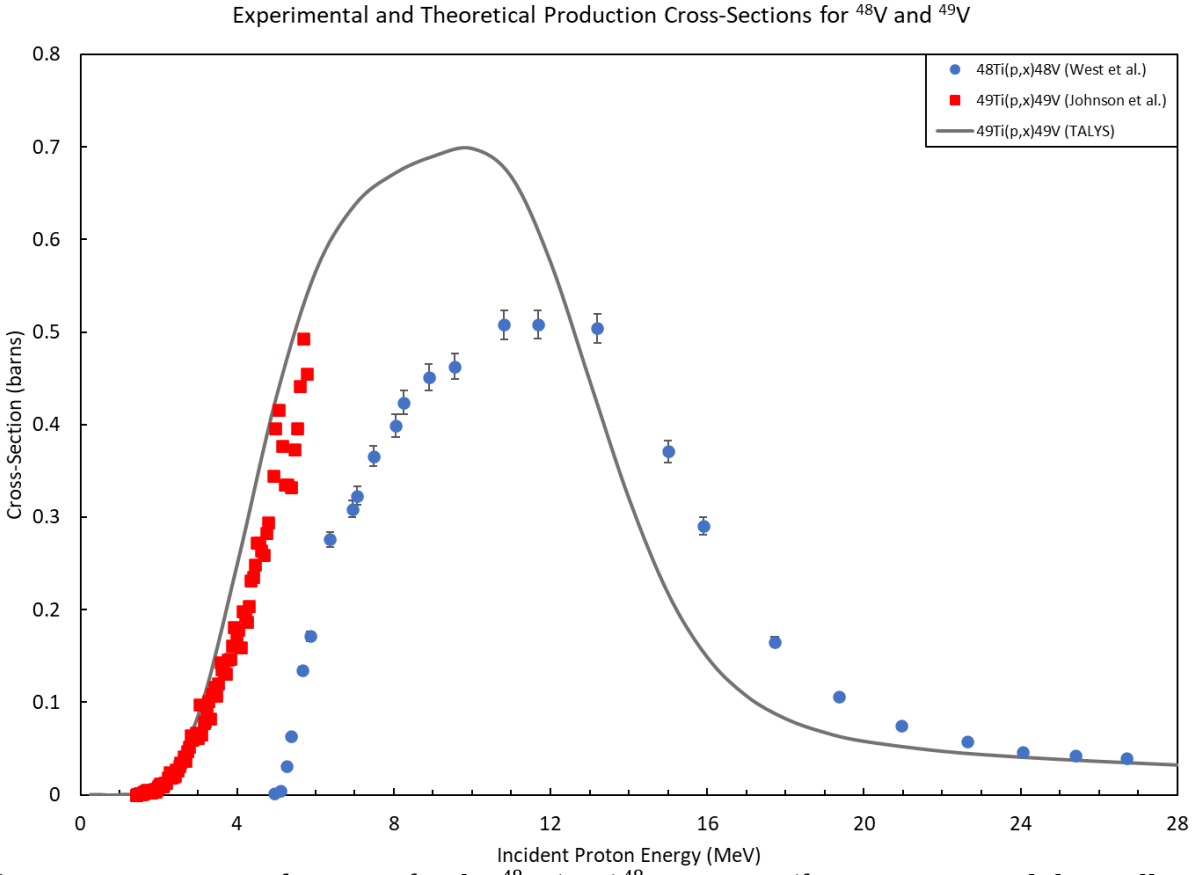

Figure 1.1: Excitation functions for the ^{48}Ti(p, n)^{48}V reaction (from experimental data collected by West et al. [26]) and the ^{49}Ti(p, n)^{49}V reaction (from experimental data collected by Johnson et al. [28,30] along with theoretical data calculated using the TALYS reaction code [29]. With the ^{49}Ti(p, n)^{49}V reaction having a lower threshold and higher maximum cross-section than the ^{48}Ti(p, n)^{48}V reaction, it will be unlikely for ^{48}V to be produced in quantities 10^4 times larger than any ^{49}V. Even with a ^{48}Ti containing less than 1% of ^{49}Ti.

To overcome this limitation, an alternative production method could be producing ^{48}V by bombarding a ^{nat}Sc foil with α particles. Natural Sc is 100% ^{45}Sc, so isotopic enrichment is not necessary. For α-irradiation of ^{45}Sc, the ^{45}Sc(α, n)^{48}V cross-section has been measured in numerous studies and the maximum cross-section appears to be nearly 450 millibarns for an incident α energy of 12 MeV [31–36]. However, the ^{45}Sc(α, γ)^{49}V reaction cross-section has not been experimentally determined. The predicted excitation function for the ^{45}Sc(α, γ)^{49}V reaction has a peak of approximately 0.15 millibarns for about 10.5 MeV α particles [29]. Considering these values, the

atomic $^{48}V/^{49}V$ ratio for ^{48}V produced with this production method would be $>10^3$. Although, this is less than the desired $>10^4$ ratio, the error in this prediction could be large enough that the actual ratio does meet this purity requirement. To determine this, an experiment was performed as part of this dissertation and more discussion on this technique can be found in Chapter 3.

Another production method that might be able to produce ^{48}V in high enough isotopic purity with respect to ^{49}V involves producing ^{48}Cr through α-irradiation of ^{nat}Ti and followed by the set-up of a $^{48}Cr/^{48}V$ generator to generate pure ^{48}V. However, this would require a high energy cyclotron as the α-particle energy would need to be > 80 MeV and the production cross-section is very small (~ 1 millibarn). To be able to use a lower energy cyclotron, the beam would have to be ^3He. But, the production cross-section for ^{48}V with ^3He and ^{nat}Ti is also very small (up to ~10 millibarns for ^3He incident energies of approximately 40 MeV) [37]. These techniques will not be viable for producing pure ^{48}V for neutron reaction studies due to their low yields. However, the production of ^{48}Cr could be a potential method to produce pure ^{48}V by setting up a $^{48}Cr/^{48}V$ generator. This strategy is very promising as the other chromium isotopes are either stable or short-lived (see Table 1.1). The only isotope that has a longer half-life than ^{48}Cr is ^{51}Cr, which decays via electron capture into ^{51}V, which is a stable isotope of vanadium. With the proper timing, only ^{48}Cr and ^{51}Cr will be left after a first chemical separation of Cr from V (including both existing V and all of the decayed Cr), and the purified ^{48}Cr will generate high purity ^{48}V containing only ^{51}V as the primary isotopic impurity. The best scenario for testing this case would be utilizing a production method that would allow for ^{48}Cr to be produced in sufficient quantities.

Table 1.1: Isotopes of chromium with half-lives longer than 1 minute. Where m is minutes, h is hours, d is days, and e.c. is electron capture.

	^{48}Cr [9]	^{49}Cr [17]	^{50}Cr	^{51}Cr [38]	^{52}Cr	^{53}Cr	^{54}Cr	^{55}Cr [39]	^{56}Cr [40]
Half-life	21.56 h	42 m	Stable	27.704 d	Stable	Stable	Stable	3.5 m	5.94 m
Decay Type(s)	β^+ or e.c.	β^+ or e.c.	Stable	e.c.	Stable	Stable	Stable	β^-	β^-

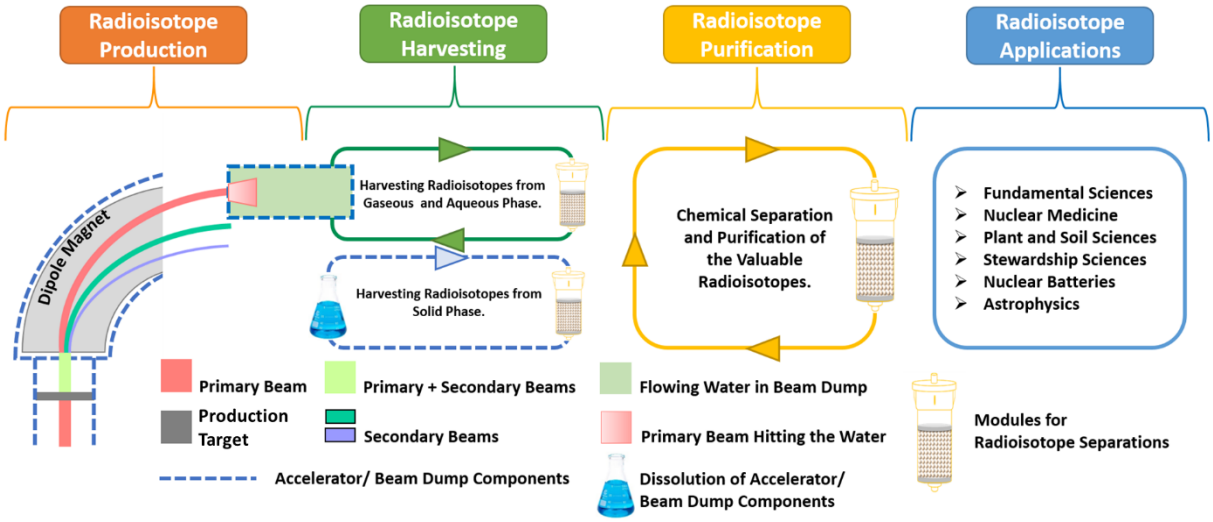

Figure 1.2: Schematic demonstrating the isotope production process at FRIB called "isotope harvesting". Radionuclides are produced via spallation and fusion evaporation reactions from the beam either depositing in the aqueous beam dump or activating an accelerator component. In the former case, aqueous or gaseous harvesting can be performed, while solid harvesting is performed for the latter. For ^{48}Cr, the ^{48}Cr will be produced in the aqueous beam dump and is extracted onto anion exchange resin prior to any chemical separation or purification steps. During the chemical separation and purification steps, ^{48}Cr will be chemically isolated and followed by the generation of ^{48}V. The generated ^{48}V can then be separated from the undecayed ^{48}Cr and manufactured into a target that can be used for neutron reaction studies.

During routine operation of the new Facility for Rare Isotope Beams (FRIB), many difficult-to-produce exotic radionuclides are created as spallation and fragmentation by-products in an aqueous beam dump. Because more than 90% of the primary beam does not react with the production target and ends up depositing into an aqueous beam dump after being separated from the reaction by-products of the desirable secondary beam for nuclear science experiments at FRIB, these exotic radionuclides can be produced in quantities that exceed the capabilities of the current best cyclotrons, accelerators, and nuclear reactors that are dedicated to isotope production [41–46]. The process of collecting these selected by-products, which include ^{48}Cr, from the beam dump is called, "isotope harvesting". Figure 1.2 shows an overview of this process from the initial radionuclide production step to the final separation and purification step for the radionuclide of interest. Over the past decade, research has been performed on various isotope harvesting techniques.

Most of these studies focused on demonstrating the proof-of-concept to selectively separate the radionuclides of interest from the aqueous beam dump. These separation processes have typically utilized either ion exchange adsorption or solvent extraction [41,43,44,47–52]. The early studies utilized processes that were selective for isolating desired radionuclides chemically, but not selective enough to yield high isotopic purity of a single radionuclide. However, the more recent studies have demonstrated the capability of obtaining a single radionuclide with high radionuclidic purity. For example, one study demonstrated the possibility of obtaining ^{47}Ca with 100% radionuclidic purity (within the limits of detection for gamma spectroscopy measurements performed with a high purity Germanium (HPGe) detector) [41]. These types of studies are proof that it is feasible to obtain unique radionuclides in high purity from aqueous isotope harvesting at FRIB. ^{48}Cr will be created in high quantities (up to 610 mCi/day with a ^{58}Ni beam) during irradiation of the aqueous beam dump with ^{58}Ni and ^{40}Ca beams [42,53]. Large quantities (mCi levels) of highly pure ^{48}V can be obtained by harvesting ^{48}Cr and setting up a ^{48}Cr/ ^{48}V generator. The generated ^{48}V would most likely contain some ^{51}V impurity, but the ^{51}V impurity would be of lesser concern because its neutron reaction cross-sections have been measured [18] and radioanalytical techniques can be utilized to discern the amount of ^{51}V in the final ^{48}V product by calculating the amount of ^{51}Cr that decayed in the generator. The important impurity in this case would be the ^{49}V, which could theoretically be minimized with the appropriate timing during the separation and purification steps. The effectiveness for this new isotope production technique to produce mCi levels of ^{48}V that is high in isotopic purity relative to ^{49}V was investigated in this dissertation.

1.3 Objective

The work in this project examines possible protocols for producing highly pure ^{48}V targets for neutron reaction studies. This includes both the production of mCi levels of highly pure ^{48}V and the production of a thin and uniform ^{48}V target. The final result is a recommended protocol covering all of the steps from the initial extraction of ^{48}Cr from the aqueous beam dump, to the separations and timing required to set up a $^{48}Cr/^{48}V$ generator and produce mCi quantities of ^{48}V in high isotopic purity relative to ^{49}V ($>10^4$ atoms of ^{48}V/atom of ^{49}V), and finally to the fabrication of a thin and uniform ^{48}V target for neutron reaction studies.

CHAPTER 2: EXTRACTION OF RADIONUCLIDES FROM AQUEOUS BEAM DUMP

2.1 Overview

The first step in any aqueous or gaseous isotope harvesting at FRIB is to extract radionuclides from the aqueous beam dump. Over the past decade, efforts have been undertaken at the predecessor facility, the National Superconducting Cyclotron Laboratory (NSCL), to demonstrate the possibility of extracting potentially useful radionuclides, which accumulate as by-products of either primary or secondary ion beams depositing in an aqueous beam dump. This work demonstrated the feasibility of this novel capability, while progressing through various iterations of a system designed for the collection of radionuclides. Early versions of this system consisted of a stationary 100 mL water target and utilized low power secondary beams at NSCL [44,50,52], while the more recent versions involved a flowing-water beam dump that allowed for unused primary ion beams at NSCL to be deposited within it [41,47,48,53]. The latter approximated a scaled-down model of the actual FRIB aqueous beam dump and demonstrated the online harvesting of radionuclides with packed ion exchange resin columns. However, the flow rate through these columns was restricted at times to 300 mL/min in part to prevent the resin beads from leaving the columns [47,48] and a better column design is needed to allow for higher flow rates and to prevent the resins from contaminating the FRIB beam dump. The work examining possible solutions to this issue is described within this chapter.

2.2 Background and Theory

FRIB will have the capability to accelerate uranium nuclei to 200 MeV/u and lighter nuclei to slightly higher energies at a beam power of 400 kW, which allows for the possibility of producing about 80% of all known isotopes of elements up to the early transuranics

[43,45,46,48,54,55]. Most of these nuclei will be produced as spallation, fusion-evaporation, and fragmentation by-products when unused primary ions are deposited in an aqueous beam dump. A major goal of the isotope harvesting project is to extract the potentially useful radionuclides from the water, which is being circulated through a rotating Grade 5 titanium alloy (Ti-6Al-4V (wt%)) beam dump) [42,54].

Early isotope harvesting experiments were performed by depositing low-energy secondary ion beams purified with the A1900 projectile fragment separator in small stationary water targets at NSCL [44,50,55]. One of these studies demonstrated the successful separation of ^{67}Cu from unpurified secondary ion beams deposited in a stationary 100 mL water target [52]. These experiments illustrate the feasibility of collecting the radionuclides of interest from an aqueous beam dump and successfully separating them from other fragmentation by-products. However, these experiments could only be done with low power beams and comparatively small volumes of water relative to the actual FRIB beam dump (100 mL vs. approximately 6930 L [56]). To better simulate FRIB conditions, more recent isotope harvesting experiments were performed by depositing high-power beams in a flowing water target containing multiple liters of water [41,47,48,53,57]. These experiments allowed to study the feasibility of harvesting radionuclides under conditions that are similar to those at FRIB.

2.2.1 Radiolysis of Water and Expected Conditions for Aqueous Isotope Harvesting

With the stopping of fast ions in water, radiolysis reactions lead to the formation of many molecular and radical species in addition to radioactive products. Some radical species reform back to water molecules, while others eventually form the following molecular species: H_2, H_2O_2, and O_2. The actual yields of these molecular species depend on numerous variables including the linear energy transfer (LET) of the ion beam and the pH of the aqueous solution. Many studies

examining the radiolysis of water with various types of ionizing radiation have found that H_2 and H_2O_2 are the most prominently produced molecular species, while O_2 is produced in low quantities [58–60]. The H_2 can lead to overpressurization and H_2O_2 can cause stress corrosion cracking in stainless steel if it builds up within the solution [61].

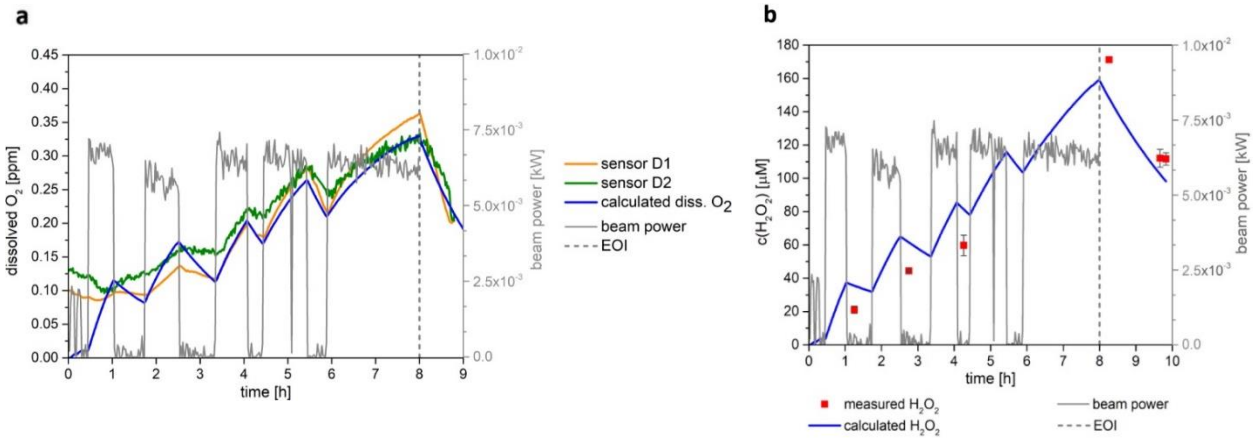

Figure 2.1: Graphs displaying the buildup of O_2 (a) and H_2O_2 (b) in the isotope harvesting system water when the flowing water target is irradiated with a $^{48}Ca^{20+}$ beam. Reprinted ref [48] with permission from Elsevier.

To minimize these potential issues, Domnanich et al. [48] constructed a system that would allow for the harvesting of radionuclides while simultaneously degrading H_2O_2 and removing gaseous species from the aqueous solution. The authors measured the concentrations of H_2O_2 and O_2 to determine how effective the system was at removing these radiolysis by-products. The other molecular species formed during radiolysis, H_2, was not expected to be very prominent in the aqueous solution due to the low Henry's law solubility constant it has in water [62] and most of the H_2 could be easily removed from the water by purging it with N_2. Figure 2.1 shows the results of their study from the irradiation of the flowing water target with a 140 MeV/u $^{48}Ca^{20+}$ beam. These results suggest that the concentration of H_2O_2 decreases in the water system due to the stainless-steel catalyst decomposing it. Meanwhile, the O_2 concentration decreases because the water was constantly purged with N_2. In both cases, the production rates of these species from the radiolysis reactions are greater than their removal rates when the flowing water target is being

irradiated [48]. It is difficult to predict the H_2O_2 and O_2 yields for future ^{40}Ca and ^{58}Ni irradiations at even higher beam energy and power; although, a recent study has proposed a possible model that may accurately predict the levels of radiolysis products that are expected to be produced in the FRIB beam dump [63]. Other studies have shown the maximum H_2O_2 and O_2 yields depend on the LET and the applied dose rates [64–66]. Regardless, the increase of dissolved oxygen and a strong oxidizing agent in H_2O_2 during the irradiation of the flowing water target suggests that the aqueous solution will be an oxidizing environment.

2.2.2 Ion Exchange Thermodynamics and Radionuclide Adsorption

Because any design of an isotope harvesting system would involve continuously passing large amounts of water over ion exchange resins for multiple hours at a time, the thermodynamics of the ion exchange process are far more important than the kinetics. This section will cover the thermodynamics of ion exchange reactions, while the kinetics will be discussed in Chapter 3 because the kinetics have a larger role in the elution and separation of adsorbed metal ions.

Ion exchangers are solid materials or resins that contain synthetic organic polymers with exchangeable sites. These sites contain replaceable cations or anions associated to the surface functional groups. In all ion exchange processes, ions from the fluid can engage in a reversible process of adsorbing onto the solid resin surface by displacing ions of the same charge on the resin matrix's functional groups [67–70]. Thus, ion exchange between an aqueous phase and a cationic resin (solid phase) within a closed system is an equilibrium process which can be represented by the following stoichiometric equation [67–69,71]

$$R_sSO_3H + M^+ + H_2O \rightleftharpoons R_sSO_3M + (H_3O)^+ \tag{2.1}$$

where M^+ is the hydrolyzed/complexed metal ion that is desired to be separated from the aqueous phase, R_s is the solid resin matrix, and SO_3H is hydrogen sulfite, which is an example of a strongly

acidic ionogenic group that can dissociate into SO_3^- and $(H_3O)^+$. The $(H_3O)^+$ can be exchanged with the metal ion or complex.

The equilibrium constant, K_{eq}, for the stoichiometric equation above (Equation 2.1) can be written as [67,68]

$$K_{eq} = \frac{k_f}{k_r} = \frac{[R_sSO_3M]\cdot[(H_3O)^+]}{[R_sSO_3H]\cdot[M^+]} \tag{2.2}$$

where $[X]$ is the concentration of component X, k_f is the forward rate constant, and k_r is the reverse rate constant.

The concentrations of chemical species at equilibrium depend on the equilibrium constant, which means the initial concentrations can be used to manipulate the direction of the reaction. Thus, for the case where the equilibrium constant in Equation 2.2 is 1,000 and the aqueous solution has 5 ppb of the targeted metal ion or complex and most of the H^+ ions are present on the surface of the resin, it is preferable for the metal species to adsorb to the resin surface while H^+ desorbs. As long as the solution is allowed to come into contact with enough resin, the metal species would continue to displace H^+ ions and adsorb to the surface until the equilibrium condition is reached. This would be the case when the concentration of the adsorbed metal ions the solution is 1,000 times larger than the concentration of the free metal ions in the solution. This process is illustrated on the next page in the "Sample Adsorption" step in Figure 2.2 from Cummins, Rochfort, and O'Connor [71].

In literature, ion exchange equilibrium is described using the distribution coefficient, K_d, which describes the partitioning of an ion (or solute) between the solid phase (or sorbent) and the aqueous phase. This can be defined as [67,69]

$$K_d = \frac{n_{ad}}{n_{soln}} \tag{2.3}$$

where n_{ad} is the moles of solute divided by the dry sorbent mass and n_{soln} is the molality of the solute in the aqueous phase at equilibrium.

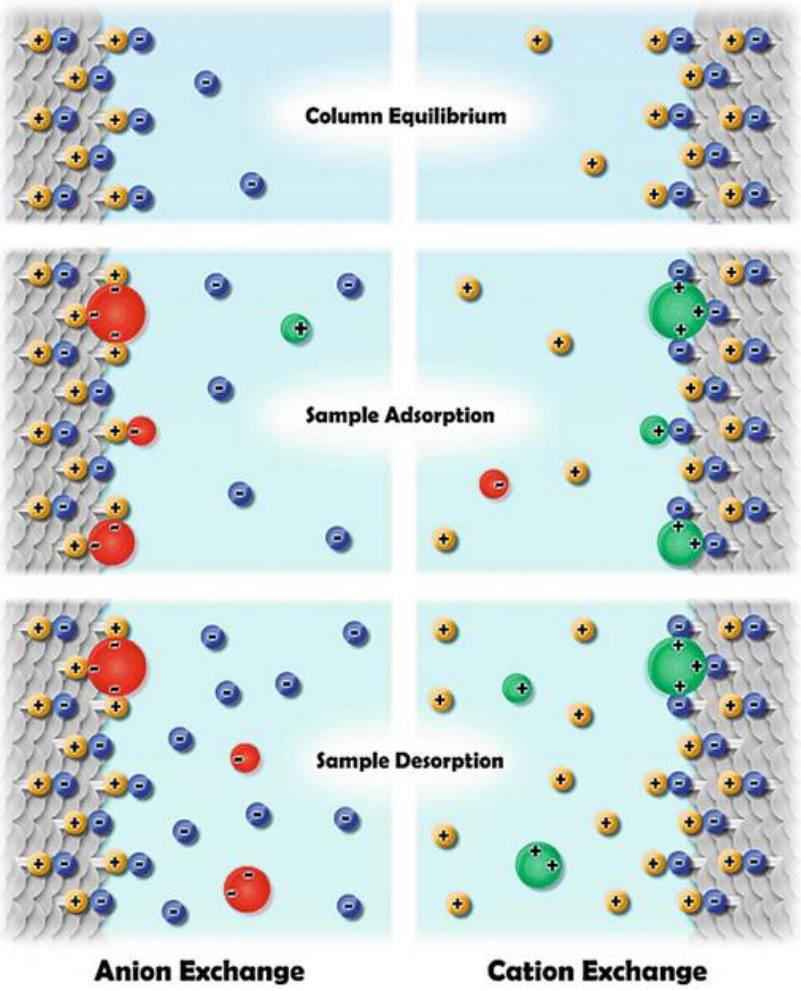

Figure 2.2: Ion exchange process steps for anion exchange and cation exchange resins. The resin is equilibrated or saturated with exchangeable ions in the "Column Equilibrium" step. Metal species adsorb to the resin surface by displacing the exchangeable ions on the surface functional groups in the "Sample Adsorption" step. If the metal species do not have high distribution coefficients, then they can be eluted with an eluent containing a high concentration of the original exchangeable ions (see "Sample Desorption" step). Reprinted from ref [71] with permission from Springer Link.

Equation 2.3 can be written in terms of the concentration of a metal ion (or solute), the weight of the resin (or sorbent), and the density of the aqueous phase as follows

$$K_d = \frac{\rho_w \cdot V \cdot (C_i - C_f)}{w_r \cdot C_f} \tag{2.4}$$

where V is the volume of the aqueous phase, C_i is the initial solute concentration in the aqueous phase, C_f is the final solute concentration in the aqueous phase, ρ_w is the density of water, and w_r is the dry sorbent weight. The distribution coefficient written in this manner has units of grams of solution/grams of resin. In literature, it is more common to encounter distribution coefficients in units of mL solution/g resin. As the difference between both is the inclusion of the density of the liquid phase, there is essentially no difference between the reported distribution coefficients as long as the density of the liquid phase does not deviate far from 1 g/mL. The distribution coefficient can vary depending on a variety of conditions, such as the pH of the aqueous phase, composition of the aqueous phase, ionogenic groups on the resin matrix, amount of crosslinking in the resin matrix, and the temperature of the system [69,70]. Thus, this will need to be considered when attempting to use ion exchange resins to extract ^{48}Cr from the FRIB beam dump.

Studies performed by Abel et al. [53] with a version of the harvesting system quantified the results of harvesting radionuclides produced with a 140 MeV/u $^{40}Ca^{20+}$ beam. To harvest the beam fragmentation and spallation products, the irradiated water was sequentially passed through a column filled with Bio-Rad AG 50W-X8 cation exchange resin (containing sulfonic acid functional groups [69]) and a Bio-Rad AG 1-X8 anion exchange resin (containing quaternary amine functional groups [69]) column. Table 2.1 on the next page shows some of the results from this experiment. Most radionuclides were adsorbed by the exchange resins according to their anticipated chemical speciation in oxidizing conditions over the measured pH range for this system (5.1 to 5.8) [53]. These results show that both ^{48}Cr and ^{48}V accumulated solely on the anion exchange resin, which is expected given that both tend to form anionic chromate and vanadate under the prevailing conditions [72]. As these ion exchange resins are expected to be used to collect unused primary ion beam by-products in future isotope harvesting experiments, these results are

pertinent to consider when developing protocols for the creation of a $^{48}Cr/^{48}V$ generator that would enable the possibility of producing an enriched ^{48}V target for neutron reaction cross section measurements.

Table 2.1: End of beam measurements of radionuclides present in the isotope harvesting system after irradiation of a flowing water target with a 140 MeV/u $^{40}Ca^{20+}$ beam. Modified from ref [53] with permission from Elsevier.

Radionuclide	Measured Activity (kBq)			
	Cation Exchange Resin	Anion Exchange Resin	H_2O_2 Degrader	H_2O
^{7}Be	13.9(4)	3.3(2)	-	-
^{18}F	39(9)	1,194(5)	-	80(4)
^{24}Na	125(7)	-	-	6(1)
^{28}Mg	1.7(1)	-	-	-
^{34m}Cl	-	4,500(9)	-	-
^{43}Sc	11(1)	23.5(9)	10.0(6)	11(1)
^{44g}Sc	4(1)	6(3)	3(1)	2.4(7)
^{44m}Sc	1.15(3)	1.59(4)	0.81(1)	0.83(9)
^{48}V	-	0.54(3)	-	-
^{48}Cr	-	0.79(6)	-	-
^{52}Mn	0.68(4)	-	-	-

2.3 Verification of Cold Cr and V Stock Solutions

A previous isotope harvesting experiment focusing on the extraction of ^{48}V from irradiated water experienced issues attempting to replicate the results of separations performed with ^{48}V produced with traditional isotope production techniques. When Loveless et al. [50] developed the separation procedures for the isotope harvesting experiment at NSCL, the authors used ^{48}V produced via proton-irradiation of a ^{nat}Ti foil, which was subsequently dissolved in 2 M H_2SO_4. This solution was diluted to 0.02 M H_2SO_4 prior to separating the ^{48}V from a variety of other metals using a column containing cation exchange resin and eluting it with a 0.01 M H_2SO_4 and 1% H_2O_2 solution. This resulted in a ^{48}V recovery of 92.4(41)%. Attempting to repeat this separation with ^{48}V captured in an aqueous solution during an irradiation with a low power ^{48}V secondary beam at the NSCL resulted in a significantly lower recovery (up to 47.0(25)%) [50].

The primary difference between both of these separation attempts is the initial state of the ^{48}V prior to the separation attempt. For the ^{48}V produced via proton-irradiation of a ^{nat}Ti foil, the ^{48}V most likely was present as some sort of cationic species during the dissolution process. For the ^{48}V produced by depositing a secondary ion beam into an aqueous solution, the highly oxidizing conditions of these solutions with a pH between 5 and 7 suggests that the prevalent vanadium species would have been vanadate, which Abel et al. observed during irradiation of water with a $^{40}Ca^{20+}$ beam [53]. Because the ligand exchange kinetics in hydrated vanadate species can be slow [73], the ^{48}V produced in these solutions appears to not fully reach equilibrium in the acidic solutions (i.e. 0.02 M H_2SO_4 or even 4 M H_2SO_4) Loveless et al. attempted to adjust it to, which caused the final recoveries to be much lower than expected [50]. To prevent similar unexpected results in future isotope harvesting tests with elements that have complex aqueous chemistries, attempts must be made to ensure those elements have undergone a similar chemistry history to that expected to be encountered during irradiation with a heavy ion beam.

Cr has a complex aqueous chemistry much like that of V [72]. Thus, any solutions prepared for the method development of post-extraction separation and purification of ^{48}Cr to set up a ^{48}Cr/^{48}V generator must contain Cr in the same species as those expected to be present in the FRIB beam dump, which in this case would be chromate. V must also be a part of this solution as vanadate because it will be present during any irradiation producing ^{48}Cr in the FRIB beam dump. To be able to perform experiments with cold, or non-radioactive, Cr and V, the stock solutions must be identified. The results from these experiments are stock cold Cr and V solutions that have Cr and V present as chromate and vanadate species respectively.

2.3.1 Methods

Stock 3250(50) ppm Cr and 7700(200) ppm V solutions were made by dissolving Cr and V salts (chromyl chloride (CrO_2Cl_2) and vanadium oxytrichloride ($VOCl_3$), both purchased from MilliporeSigma, USA) in deionized water (18.2 MΩ·cm, DI H_2O) (obtained from a Thermo Scientific MicroPure Ultrapure Water System from Fisher Scientific, USA). 20 ppm Cr and 20 ppm V solutions were made by diluting samples of these stock solutions with DI H_2O and the pH was adjusted with 0.01 M hydrochloric acid (ACS grade, 36.5%, HCl from Fisher Scientific, USA) and 0.01 M ammonium hydroxide (ACS grade, 28-30%, NH_4OH from VWR International, USA). These solutions were allowed to equilibrate for 72 hours to ensure all Cr and V species are mostly monomeric rather than polymeric (e.g. V is primarily present as polymeric species at concentrations of 102 ppm V and is mostly monomeric at concentrations of 10.2 ppm V in pH 5 to 7 solutions [74]). Additional 10 ppm and 1 ppm Cr and V solutions were made from these 20 ppm solutions and diluted with aqueous solutions of the appropriate pH. Batch tests were completed by continuously shaking 20 mL aliquots of these solutions with 250 mg of wet AG 1-X8 anion exchange resin in the OH^- form (20-50 mesh, procured from Bio-Rad Laboratories, USA) for 24 hours at 300 rpm. After completion of these tests, 10 mL of each solution was withdrawn to be analyzed via inductively coupled plasma-optical emission spectroscopy (ICP-OES) with an Agilent 5900 ICP-OES. The distribution coefficient (K_d) was then calculated using Equation 2.4. Since this equation requires the dry resin weight, a set of 250 mg of wet AG 1-X8 resin samples were dried for 24 hours at 60 °C. After those samples cooled to room temperature, they were reweighed and the average ratio of the dry resin weight to wet resin weight was determined to be 0.53(3). This ratio was used along with the wet resin weight for each sample to determine the correct w_r values and, thus, allow for the distribution coefficients to be calculated.

2.3.2 Results

The results of these studies are shown in Table 2.2. All distribution coefficients were very high, which suggests that the stable Cr and V present in these solutions are prevalently chromate and vanadate respectively. Of particular interest are the results for the 20 ppm Cr and V solutions that were produced by directing diluting the stock Cr and V solutions with DI H_2O and performing no additional pH adjustment (the right-most columns for both Cr and V). The distribution coefficients of Cr and V in these solutions are also very high, which suggests only a simple dilution with DI H_2O along with a 72-hour equilibration time is necessary to obtain a starting Cr and V solution that contains monomeric chromate and vanadate respectively. As such, all cold Cr and V solutions used to mimic the aqueous beam dump solution in this dissertation were made by diluting the stock Cr and V solutions containing dissolved CrO_2Cl_2 and $VOCl_3$ with DI H_2O.

Table 2.2: Calculated distribution coefficients in grams of solution/grams of resin of Cr and V in various aqueous solutions. Note that those determined for the columns with a range in pH are those made by diluting the Cr and V stock solutions with DI H_2O.

Metal Ion Concentration (ppm)	V			Cr		
	pH 5	pH 7	pH 3-4.5	pH 5	pH 7	pH 3-4.7
1	> 1,500	> 1,500	> 1,500	> 1,500	> 1,500	> 1,500
10	> 15,000	> 15,000	> 15,000	> 15,000	> 15,000	> 15,000
20	> 30,000	27,300	> 30,000	> 30,000	> 30,000	> 30,000

2.4 Single-Pass Extraction Efficiency

With the test harvesting system, irradiated water can be circulated continuously over packed ion exchange resin columns. But, a recent design of the section of the FRIB beam dump where isotope harvesting will be performed, called the clean-up loop, has the isotope harvesting equipment being installed in parallel with a line containing two 50-gallon ion exchange resin drums in series. The residence time, or the time a species spends in a solution, for cations and anions passing through these ion exchange resin drums is much shorter than the time it takes the solution to pass through the resin drums. Therefore, these ion exchange resin drums will remove

essentially all radiocations and radioanions in the solution that passes through them. As a result, any ion exchange resin columns or cages that are installed in parallel to these large resin drums must be effective at removing large quantities of radioions from the solution in one single pass.

For the purposes of isotope harvesting, it is important to measure the total uptake of the ion exchange resin in either a column or cage configuration rather than simply the extraction efficiency of the process. To do this, it is useful to measure the change in the mass flow rate of a metal ion entering and leaving the boundaries of the isotope harvesting equipment, which would contain some sort of arrangement of cation and anion exchange resins (possibly two in series or maybe more in parallel). The change in mass flow rate is equal to the mass accumulation rate, $\dot{m}_{accum}$, of a metal ion adsorbing on the ion exchange resins. The mass accumulation rate is also dependent on the entering mass flow rate for that metal ion, $\dot{m}_{in}$, and the extraction efficiency, ε, of the ion exchange resin to remove that metal ion. Equation 2.5 illustrates this:

$$\dot{m}_{accum} = \varepsilon \dot{m}_{in} = \dot{m}_{in} - \dot{m}_{out} \tag{2.5}$$

Note that the mass flow rate for a metal ion is equal to the concentration of that metal ion, C, times the volumetric flow rate, v, so Equation 2.5 can be expressed as

$$\dot{m}_{accum} = \varepsilon C v \tag{2.6}$$

Thus, measuring both the extraction efficiency and the volumetric flow rate provides insight into what configuration would be the best for harvesting radionuclides from the clean-up loop. Experiments were performed to measure these values and elucidate the configuration for the ion exchange resin that is the most effective for extracting metal ions (especially Cr) from rapidly flowing aqueous solutions.

2.4.1 Methods

These experiments were performed with the stock 20 ppm Cr and V solution prepared via direct dilution with DI H_2O as described in the previous section (Section 2.3.2).

2.4.1.1 Ion Exchange Resin Packed Column or Cage Setup

Both anion and cation exchange resin (AG 1-X8 anion and AG 50W-X8 cation, both 20-50 mesh and acquired from Bio-Rad Laboratories, USA) were prepared into columns via two methods: a traditional packed resin column and a novel resin cage. Prior to preparing any column or cage, the resins were washed with a series of DI H_2O and HCl rinses followed by conditioning with either 2 M NaOH (for anion exchange resin to be in the OH^- form) or 5 M HCl (for cation exchange resin to be in the H^+ form) and rinsed with more DI H_2O until the water leaving the resin was neutral in pH as described in Table 2.3.

Table 2.3: Rinsing and conditioning steps for preparing cation and anion exchange resins to be in the H^+ and OH^- forms respectively.

Cation Exchange Resin		Anion Exchange Resin	
Solution Purpose	Description	Solution Purpose	Description
Rinse	50 mL DI H_2O	Rinse	50 mL DI H_2O
Rinse	50 mL DI H_2O	Rinse	50 mL 2 M HCl
Condition	30 mL 5 M HCl	Rinse	50 mL 4 M HCl
Rinse	50 mL DI H_2O	Rinse	50 mL 6 M HCl
Rinse	50 mL DI H_2O rinses until solution leaving resin is neutral in pH	Rinse	50 mL DI H_2O
		Rinse	50 mL DI H_2O
		Condition	30 mL 2 M NaOH
		Rinse	50 mL DI H_2O rinses until solution leaving resin is neutral in pH

The traditional ion exchange resin columns contained 1.5 g of resin packed in rigid polycarbonate tubing (3/8″ OD, 1/4″ ID, McMaster-Carr, USA) that was plugged with glass wool as described in Abel et al. [41]. While these columns were proven to be effective in a few of the more recent isotope harvesting studies [41,47,48,53], the glass wool does not always prevent ion

exchange resin from entering the beam dump loop and it is difficult to safely handle spent ion exchange resin upon the conclusion of an experiment. Part of the work under study in this dissertation was to determine a safer and potentially more effective setup for the ion exchange resin.

Figure 2.3: Polypropylene resin cages for retaining ion exchange resins and allowing for radionuclides to be collected at faster flow rates than those obtainable with conventional packed columns. From left to right, each 3D-printed cage can retain 1.5 g, 1.0 g, and 0.5 g of 20-50 mesh ion exchange resin.

The results of this work came in the form of 3D-printed polypropylene (Centaur PP filament from FormFutura, Netherlands) resin cages, which are shown in Figure 2.3. Three cage sizes are shown in the figure, but other sizes could be made because these were produced through fused deposition modelling, which is an additive manufacturing process. Ion exchange resin would be loaded up to the end of the mesh part of the cages, which corresponds to 1.5 g, 1 g, and 0.5 g for each cage depicted from left to right in Figure 2.3.

2.4.1.2 Single-Pass Extraction Efficiency Tests

To accurately test the effectiveness of the ion exchange column designs under study, all columns were operated under the same conditions. Namely, this involves supplying water at the same pressure into the ion exchange resin columns or cages (70 psig) at standard room temperature (23 °C). Prior to conducting the experiments, a 10 gallon (37.85 L) solution of 100 ppb Cr and 100 ppb V was prepared adding the appropriate amount of the stock 20 ppm Cr and 20 ppm V solution to the appropriate amount of DI H_2O and the solution was mixed by continuously circulating the water in the tank for 15 minutes. A sample of the 10 gallon solution was then taken. Upon startup, a needle valve was briefly left slightly opened (~2 s) to reduce the stress on the piping and tubing that was caused by the sudden rapid flow (up to ~3 liters/min) of water passing through them. Immediately after this step, no flow was diverted to ensure the flow rate through the columns or cages would not be reduced. After the startup process, 1 gallon of solution was allowed to pass through a series of ion exchange columns or cages while the volumetric flow rate was monitored with either an analog flow meter (for trials performed with cages, 0.1 to 1 gpm 7205 series flow meter for water procured from King Instrument Co. via McMaster-Carr, USA) or a digital flow meter (Omega FTB323D Micro-Flo, acquired from Silicon Valley Techparts, USA). The basic setup of these experiments is shown in Figure 2.4 on the next page. Once a trial was completed, a sample of the outlet water was taken. All water samples were measured via ICP-OES.

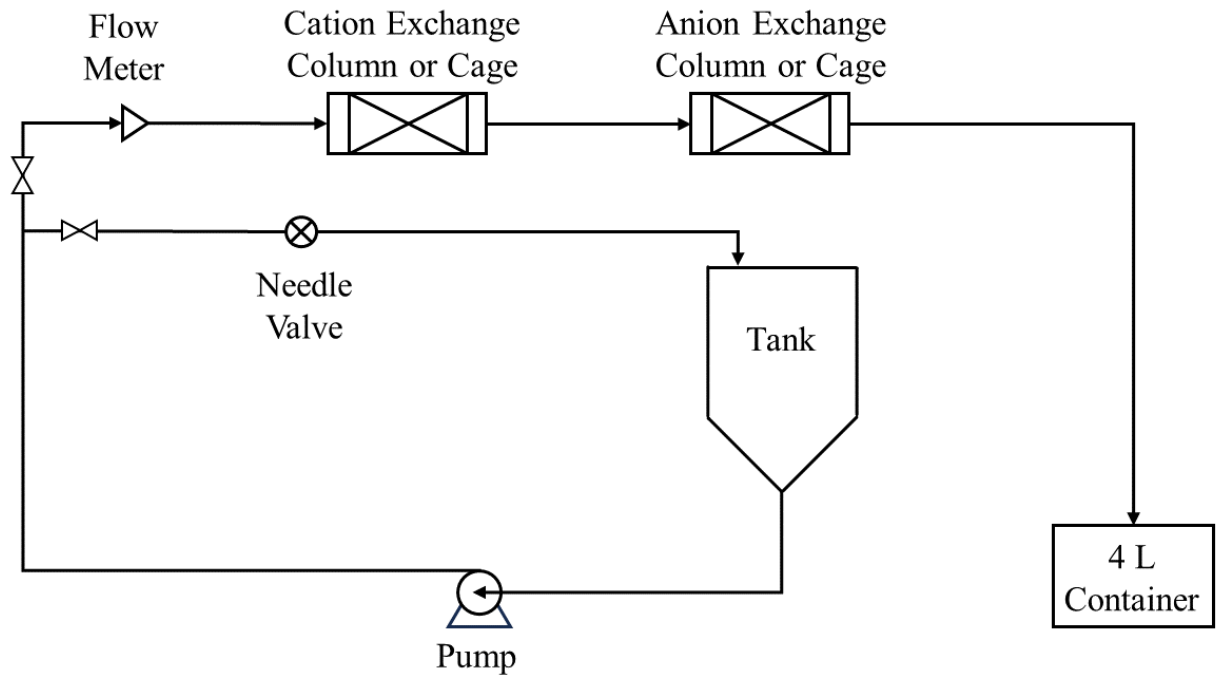

Figure 2.4: Diagram showing the locations of major pieces of equipment used in the single-pass efficiency tests. The pump (Grundfos CRNE 3-6) was set to output the solution at a constant pressure of 70 psig and was turned off to stop the flow of water at the completion of each trial.

2.4.2 Results

The measured volumetric flow rates, single-pass efficiencies, and the mass accumulation rates for the single-pass efficiency tests are shown in Table 2.4 on the next page. From these results the packed ion exchange columns had higher extraction efficiencies than the ion exchange resin cages, but with a significantly slower volumetric flow rate. This led to the accumulated Cr mass rates for the packed 1.5 g ion exchange resin columns and 1.5 g cages being same within error; albeit, the resin in the cages extracted V at a higher rate than the packed columns. On the surface, these results appear to contrast what Domnanich et al. [48] observed, which was the mass accumulation rate increases as the volumetric flow rate through an ion exchange column is increased. However, the pump used in the experiment Domnanich et al. kept outputing at a constant pressure of 25 psig even when the volumetric flow rate through the packed ion exchange columns

was varied [48]. Decreasing the volumetric flow rate through the columns allowed some of the solution to by-pass the columns rather than flow through them. This results in a decrease to the mass accumulation rate, which ultimately increases the total time to extract >99% of the desired radionuclides. With the single-pass efficiency tests, none of the solution was allowed to by-pass the columns or cages. Therefore, the observed accumulated mass rates are the maximum rates for each set up.

Table 2.4: Measured single-pass efficiencies, $\boldsymbol{\varepsilon}$, volumetric flow rates, $\boldsymbol{v}$, and the Cr and V mass accumulation rates on the anion exchange resin in various forms. Note that 3 trials were performed for each setup. Despite varying significantly in single-pass efficiency and volumetric flow rate, the rate that Cr that accumulates onto the anion exchange resin is the same within error for the 1.5 g packed column as the 1.5 g resin cage. The V accumulation rate on the resin suggests the extraction using the cages is enhanced; however, this could be due to small sample size.

Anion Column Type	ε	v (L/min)	$\dot{m}_{accum_{Cr}}$(µg/min)	$\dot{m}_{accum_{V}}$ (µg/min)
1.5 g Packed Column	0.563(26)	0.52(3)	26(2)	35(3)
1.5 g Resin Cage	0.106(7)	2.95(4)	27(3)	54(8)
0.5 g Resin Cage	0.094(29)	2.90(4)	20(4)	30(5)

The packed 1.5 g ion exchange resin columns had similar accumulated Cr mass rates to the 1.5 g ion exchange resin cages, but there is one noticable difference. Two of the packed 1.5 g ion exchange resin columns (one cation and one anion) began to migrate downstream during the tests. Figure 2.5 on the next page shows how far the cation exchange resin migrated during these single-pass efficiency tests. This is one of the reasons why the volumetric flow rate was typically restricted to either 300 or 450 mL/min through these packed 1.5 g ion exchange resins in previous isotope harvesting tests [47,48]. No resin left the cages and all cages remained in the 3D-printed polycarbonate (Polylite PC, procured from Polymaker, USA) tubes during tests with the ion exchange resin cages. Furthermore, at the conclusion of the experiment the resin cages were easier to handle and dispose of than the packed columns due to the resin being contained As a result, the ion exchange resin cages appear to be better than the packed ion exchange columns because of the

reduced risk of contaminating the FRIB beam dump with loose resin beads and the lower likelihood of spilling the resin beads in a radioactive fume hood or hot cell.

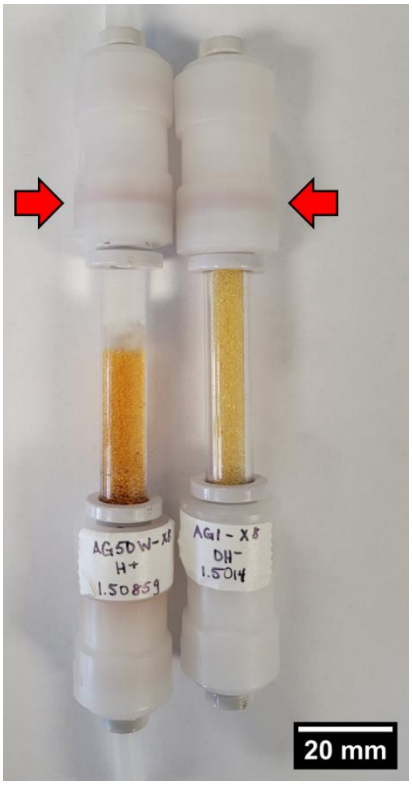

Figure 2.5: Two packed 1.5 g ion exchange resin columns after the single-pass efficiency tests. The red arrows indicate where each column was originally packed to. The 100 ppn Cr and 100 ppb V solution was passed through from the top to the bottom of each column with the cation exchange column located before the anion exchange column.

2.5 Proof-of-Concept Extraction of ^{48}V and ^{51}Cr

The resin cages were designed to be able to collect radionuclides by continuously passing irradiated water over them at high flow rates, and it would be ideal to test this setup with radiotracers to confirm this hypothesis. However, part of the water system failed during testing prior to an experiment with radiotracers could be performed. Although a redesign of the system sufficiently strengthened the system, testing on the updated system could not be completed before too much of the radiotracers ^{48}V and ^{51}Cr had decayed away. So, an alternative batch extraction test was conducted, which allowed for some important information to be gained on the effectiveness of the 3D-printed cages.

2.5.1 Methods

The initial solutions used in these studies contained ^{51}Cr (as sodium chromate in a saline solution with a pH of 8-10, purchased from PerkinElmer, USA) and ^{48}V produced at the University of Alabama-Birmingham (UAB).

2.5.1.1 Ion Exchange Resin Cage Setup

All column materials including tubing, adapters, and cages were rinsed with 3% v/v nitric acid (produced by using DI H_2O to dilute Suprapur 65% nitric acid (HNO_3) procured from MilliporeSigma, USA) followed by a final DI H_2O rinse prior to loading the cages. Both anion and cation exchange resin (AG 1-X8 anion and AG 50W-X8 cation, both 20-50 mesh and acquired from Bio-Rad Laboratories, USA) were loaded in 0.5 g resin cages, then the entire cage with resin was washed and conditioned following the procedure described in Table 2.3.

2.5.1.2 ^{48}V Production and Purification

^{48}V was produced via proton irradiation of an enriched Ti foil (~94.5 mg) at UAB. The irradiated foil was dissolved in 3 mL of a 1.2 M ammonium bifluoride and 12.1 M HCl solution as described in Loveless et al. [24]. Prior to being shipped to Michigan State University (MSU), about 80% of the ^{48}V was reconstituted in 1.5 mL of 12.1 M HCl. At MSU, the ^{48}V was separated from the irradiated Ti target material following the procedure in the subsequent paragraph.

First, the ^{48}V in HCl solution was vortexed, centrifuged at 1,500 rpm for 1 minute, and the supernatant was carefully transferred into a new 2.5 mL screw-cap vial. DI H_2O and 5 M HCl (TraceSELECT grade, 34-37%, procured from Honeywell Fluka via Fisher Scientific, USA) were used to dilute 493 µL of the supernatant (^{48}V activity of 22.4(4) µCi) to yield a 5 mL 5 M HCl solution. Three columns of 1.33 g hydroxamate resin (ZR resin, purchased from Eichrom Technologies, USA) were prepared, arranged in series, and washed and conditioned with DI H_2O

and 5 M HCl respectively via gravity flow. The prepared 5 M HCl solution with ^{48}V was passed through the columns first followed by 109 mL of a 5 M HCl wash solution. After the wash solution passed through, the orange Ti band was observed to be close to the bottom of the last ZR resin column. Once the separation was completed, the fractions containing ^{48}V were evaporated to approximately 1 or 2 mL and transferred to a 15 mL falcon tube (recovered ^{48}V activity = 18.8(2) µCi). All solutions were monitored via gamma spectroscopy performed using a High-Purity Germanium (HPGe) detector (Canberra BEGe gamma-ray detector, BE2020) and analyzed using Genie2000 software.

2.5.1.3 Batch Extraction

Aqueous solutions containing ^{51}Cr and ^{48}V were produced using 8.983 mL of DI H_2O, 17 µL of the ^{51}Cr solution from PerkinElmer, and 1 mL of the purified ^{48}V solution. The pH of each solution was then adjusted to approximately pH 4.5 using concentrated NH_4OH (ACS grade, 28-30%, acquired from VWR International, USA). Resin cages containing 500 mg of AG 1-X8 anion exchange resin (20-50 mesh) in the OH^- form were placed in the aqueous ^{51}Cr and ^{48}V solutions and shaken at 300 rpm and 25 ºC for 24 hours. Then, the cages were removed and centrifuged in a 15 mL falcon tube with a 3D-printed polypropylene bung or sleeve as shown in Figure 2.6 on the next page to extract the supernatant prior to performing studies on batch elutions, which will be covered in Chapter 3. For any additional batch extractions performed with the resulting depleted load solutions, 500 mg of the appropriate ion exchange resin (AG 1-X8 anion exchange resin (20-50 mesh) in the OH^- form, AG 50W-X8 cation exchange resin (20-50 mesh) in the H^+ form, or mixed cation and anion exchange resin (250 mg of AG 1-X8 and 250 mg of AG 50W-X8, both 20-50 mesh)) were added to the resin cages and the 24 hour extraction procedure was repeated. Batch extractions performed with higher amounts of ^{51}Cr followed the same

procedure as those used with the ^{51}Cr and ^{48}V solutions, except the pH of the initial solution did not need to be adjusted. Gamma spectroscopy was performed using a HPGe detector and analyzed using Genie2000 software. For elemental analysis of aqueous solutions, measurements were conducted via ICP-OES.

Figure 2.6: For separating the cages and the resins within them from the solution filling the pores and gaps within the resin, the cages can be placed on a bung or sleeve (3D-printed part in the middle), slid into a 15 mL falcon tube, and the falcon tube can be centrifuged. The bung or sleeve prevents the cage from falling to the bottom of the tube and allows liquid to escape the cage during centrifuging.

2.5.2 Results

The results from these batch extraction studies with ^{51}Cr and ^{48}V from the originally pH ~ 4.5 aqueous solutions using anion exchange resin are shown in Table 2.5 on the next page. The overall extraction efficiencies for ^{51}Cr and ^{48}V were modest as only 65.7(25)% and 69.0(9)% were extracted. These unexpected results stand in contrast with the high distribution coefficients for monomeric V and Cr species with AG 1-X8 anion exchange resin in these solutions (see Table 2.2). To elucidate the observed behavior, additional tests were performed.

Table 2.5: Average batch extraction of ^{48}V and ^{51}Cr from a pH 4.5 aqueous solution using anion exchange resin results for 9 trials. All activities were decay-corrected to the start of extraction for each sample. Modified from ref [75].

Radionuclide	Initial (μCi)	Recovered	
		(μCi)	(%)
^{48}V	1.86(12)	1.28(11)	69.0(9)
^{51}Cr	1.51(9)	0.99(9)	65.7(25)

The first test attempted to discern whether an equilibrium exists between the cationic Cr and V (Cr(III) and V(IV)) and anionic Cr and V (Cr(VI) and V(V)). For this test, three of the original load solutions underwent an additional 24-hour batch extraction within 5 to 31 days after the first 24-hour batch extraction. The additional batch extractions were performed with new ion exchange resin (mixed cation and anion, cation, and anion respectively) filled cages. Additionally, an empty resin cage was introduced to another original load solution to approximate the amount of ^{51}Cr and ^{48}V that could potentially be trapped by the polypropylene cage material during the extraction process. The results from these tests (see Table 2.6 on the next page) suggest that some of the ^{51}Cr and ^{48}V do become trapped within the resin material and both ^{51}Cr and ^{48}V are present as cationic and anionic species. Furthermore, the pH readings suggest a shift in pH occurs during the loading of the ion exchange resins. This observation was expected because the OH^- and H^+ counterions exchange with metal species in the solutions; however, the observed acidic pH after the introduction of cation exchange resin was not expected. About 50 to 5,000 more cations than the number of ^{51}Cr and ^{48}V ions would need to be present to cause a shift in the solution pH from 9 to 1.5 and 3.5.

Table 2.6: Results for additional batch extractions conducted with an empty resin cage (none) and resin cages with 500 mg of either solely one type of ion exchange resin or half cation and half anion exchange resin (mixed). All activities were decay-corrected to the start of extraction for each sample. The initial pH of all solutions was 9. Modified from ref [75].

Resin Type	Initial ^{48}V (µCi)	^{48}V Recovered (µCi)	^{48}V Recovered (%)	Initial ^{51}Cr (µCi)	^{51}Cr Recovered (µCi)	^{51}Cr Recovered (%)	Final pH
Mixed	0.181(3)	0.112(3)	61.8(21)	0.249(8)	0.118(10)	48(4)	3.5
Cation	0.616(10)	0.408(11)	66.2(21)	0.593(21)	0.256(25)	43(4)	1.5
Anion	0.581(9)	0.335(10)	57.7(20)	0.527(19)	0.257(22)	49(5)	9.75
None	0.178(4)	0.009(5)	5.0(29)	0.258(10)	0.007(13)	3(5)	9

Table 2.7: Elemental analysis of a mixed ^{48}V and ^{51}Cr solution and a pure ^{51}Cr solution used in batch extraction experiments. Samples were measured via ICP-OES. Reprinted from ref [75].

Element	Mixed ^{48}V and ^{51}Cr Solution (ppm)	^{51}Cr Solution (ppm)
Al	1.191	< 0.005
B	2.717	0.149
Ca	0.113	< 0.005
Cr	< 0.005	< 0.005
Fe	0.194	< 0.005
Na	285	< 0.005
Si	0.054	0.190
V	< 0.005	< 0.005
W	0.300	< 0.005

Table 2.8: Average results for 2 batch extraction trials with samples containing only ^{51}Cr. All activities were decay-corrected to the start of extraction for each sample. Modified from ref [75].

Initial ^{51}Cr (µCi)	^{51}Cr Recovered (µCi)	^{51}Cr Recovered (%)
25.5(4)	22.5(4)	88.3(19)

Performing elemental analysis on one of the ^{51}Cr and ^{48}V solutions reveals the presence of increased quantities of sodium, boron, aluminum, tungsten, and iron (see Table 2.7). Elemental analysis of solutions containing only ^{51}Cr suggest these solutions contain significantly fewer metal ions than the solutions containing both ^{51}Cr and ^{48}V, which means these impurities originate from the prior processing steps for the ^{48}V. Without as many of these impurities, ^{51}Cr was extracted with much higher recoveries (see Table 2.8) than those observed with the mixed ^{51}Cr and ^{48}V solutions. This suggests that the impurities from the ^{48}V solution limited the amount of ^{51}Cr and ^{48}V that were present as anionic chromate and vanadate species. Thereby, fewer ^{51}Cr and ^{48}V were present

as anionic species in these solutions than would be expected in the aqueous beam dump at FRIB [53]. Therefore, while the extraction efficiencies observed in all these tests are not expected to be representative for the behavior of Cr and V in the FRIB beam dump, they do highlight the potential of resin cages being used to allow for the collection of radionuclides from the beam dump and for safe disposal upon the conclusion of an experiment.

2.6 Concluding Remarks

Within this chapter, cold Cr and V stock solutions were identified and allowed for preliminary tests with stable Cr and V to occur before proof-of-concept tests with radioactive Cr and V. A key component of this process was to ensure that the Cr and V in these aqueous solutions were chromate and vanadate respectively, which are the species ^{48}Cr and ^{48}V are expected to be in the FRIB beam dump. One of the preliminary tests performed suggested housing the ion exchange resin in cages during the collection process does not significantly affect the mass accumulation rate on the ion exchange resin, and may lead to an increase in the mass accumulation rate (at least with respect to V), while at the same time allowing for higher volumetric flow rates to be obtained without the possibility of contaminating the FRIB beam dump line. However, the cages did allow for easier handling of the resin after the conclusion of the experiment.

For tests performed with radiotracers ^{51}Cr and ^{48}V, attempting to use the ion exchange resin cages in a batch mode resulted in moderate extraction efficiencies from the aqueous solution (65.7(25)% and 69.0(9)% respectively). Such recoveries were not expected because of the high distribution coefficients that were observed in experiments with stable Cr and V. However, performing elemental analysis on the aqueous solutions themselves suggest that the presence of large quantities of impurities from the processing steps for the ^{48}V appear to hinder the adsorption of ^{51}Cr and ^{48}V to the anion exchange resin. Batch extractions conducted with aqueous solutions

containing only ^{51}Cr resulted in recoveries of 88.3(19)%. Thus, the extraction efficiencies observed for the ^{51}Cr and ^{48}V in this proof-of-concept study are not good indicators of what to expect from harvesting at FRIB, but the study does provide more evidence in favor of utilizing ion exchange resin cages in place of packed ion exchange resin columns. Particularly as there is potential for the ion exchange resin cages to provide similar quantities of radionuclides while having the capability of performing extractions in a batch mode with a small amount of solution and being safer to handle and use overall.

CHAPTER 3: PRODUCTION OF HIGH PURITY ^{48}V

3.1 Overview

After radionuclides are extracted from the aqueous beam dump at FRIB, they undergo a separation and purification process to ultimately obtain the desirable radionuclide in the appropriate purity. Thus, the effectiveness of isotope harvesting as an isotope production technique relies not only on production rates, but the isotopic and chemical purity of the produced radionuclides. The crucial requirement for the activation method to be used to measure the ^{48}V(n, γ)^{49}V cross-section with a ^{48}V target is the high isotopic purity with respect to ^{49}V (>10^4 atoms of ^{48}V/atom of ^{49}V). This purity cannot be obtained via the conventional method for producing ^{48}V, which involves irradiating ^{nat}Ti foil with protons, but could theoretically be achieved with isotope harvesting by setting up a ^{48}Cr/^{48}V generator. Additionally, production via α-irradiation of a ^{nat}Sc foil might be another possible production route to attain a ^{48}V purity that is close to the required purity and is a more conventional isotope production method. The work examining and comparing both production methods is presented within this chapter.

3.2 Background and Theory

3.2.1 Conventional Isotope Production

Conventional isotope production techniques utilize cyclotrons, nuclear reactors, or accelerators. Worldwide, most techniques utilize accelerators, such as the commercially available low energy (<30 MeV) and even 30 MeV cyclotrons, to accelerate protons or deuterons, which can produce abundant amounts of many important radionuclides for medical purposes (e.g. ^{11}C, ^{15}N, ^{18}F, ^{111}In, ^{201}Tl, ^{67}Ga, and ^{123}I) [76,77]. For higher energies or wider variety of particle beams, such as the capability to accelerate α particles, larger cyclotrons are needed and can only be found

at a few sites. Regardless of the utilized particle beam, each produced radionuclide still needs to be extracted from the irradiated target material, which typically is a solid target [76].

If a conventional method is under consideration for producing a particular radionuclide, then decisions must be made regarding:

1. Feasible nuclear reactions.
2. The required target material composition and thickness.
3. The selection of the particle beam type and energy.
4. Radiochemical separation processes (see Section 3.2.2)

The start of this process involves identifying the underlying nuclear reaction(s). With ^{48}V production using ^{nat}Sc foil, the primary reaction of interest is the ^{45}Sc(α, n)^{48}V because the natural abundance of ^{45}Sc is 100%. There are a number of side reactions that can occur too, but the most important one of these side reactions is ^{45}Sc(α, γ)^{49}V because ^{49}V will be an undesirable impurity in the final ^{48}V product. At this point in the process, the target material composition and particle beam type have been identified as ^{nat}Sc and α respectively. However, the α beam energy and the ^{nat}Sc target thickness still needs further consideration.

To determine the beam energy and target thickness, excitation functions and the stopping characteristics of the particle beam in the target material need to be considered. The first step in this process would be to examine the excitation functions of all possible reactions that could occur in the target material at the range of beam energies the target material is planned to be exposed to. In the case of α-irradiation of ^{nat}Sc, all excitation functions on ^{nat}Sc that produce radionuclides over the range of incident α energies of 0 to 25 MeV are shown in Figure 3.1 on the next page. The data in the plot includes both measured data from a variety of experiments [31–36] and predicted data using TALYS reaction code [29] for the ^{45}Sc(α, γ)^{49}V cross-section. One noticeable characteristic of the plot is the cross-sections of the ^{45}Sc(α, n)^{48}V and ^{45}Sc(α, γ)^{49}V reactions both decrease as new reaction channels that result in the production of other radionuclides open up. When

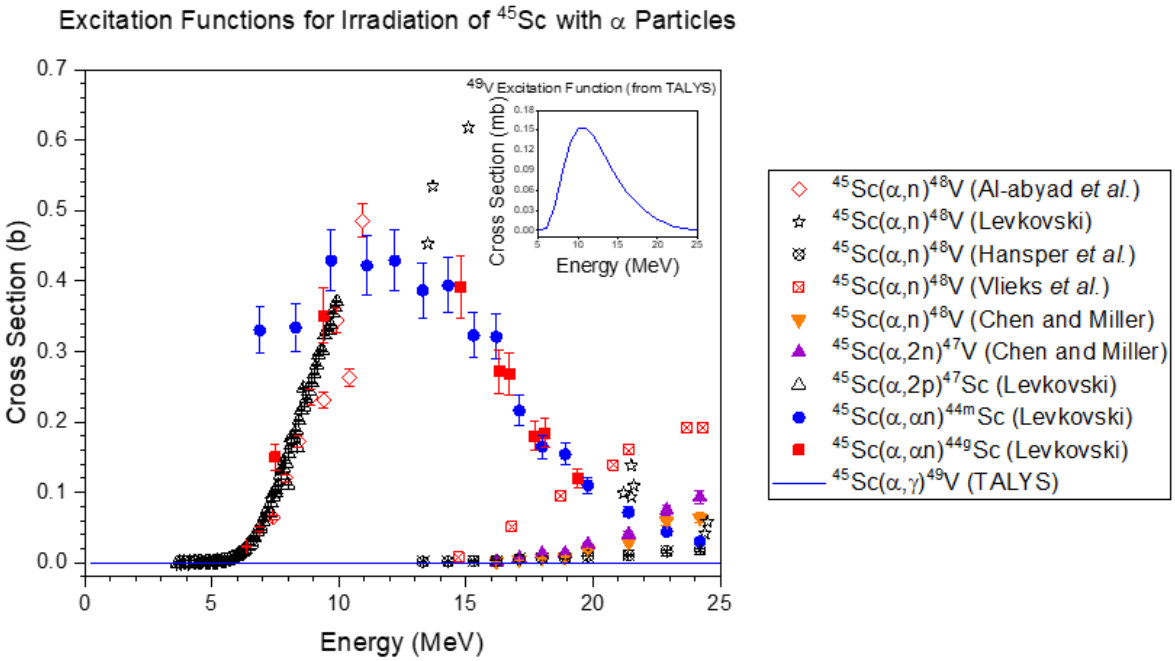

Figure 3.1: Measured cross-section data for the $^{45}Sc(\alpha, n)^{48}V$ reaction and other competing reactions for incident α energies of <25 MeV along with the theoretical excitation function for the $^{45}Sc(\alpha, \gamma)^{49}V$ reaction calculated using TALYS reaction code. Note that the measured cross-sections for the $^{45}Sc(\alpha, n)^{48}V$ reaction are on the order of hundreds of millibarn while the cross-sections for the $^{45}Sc(\alpha, \gamma)^{49}V$ reaction are predicted to be three orders of magnitude smaller.

determining the beam energy for production of a particular isotope, this characteristic of excitation functions needs to be considered, as it can affect the final purity of the radionuclide of interest. In the case of the production of ^{48}V by irradiating a ^{nat}Sc foil with α particles, the new reaction channels (shown in Figure 3.1) are not particularly concerning. The other radionuclides produced at higher incident α particle energies are either short-lived V radioisotopes that can decay away during a "cool down" period post-irradiation or radioscandium, which will be separated from the radiovanadium in the subsequent chemical separation. However, the decrease in the cross-section of the $^{45}Sc(\alpha, n)^{48}V$ reaction with the increasing α particle energy results in a lower ^{48}V production rate with the highest energy incident α particles. Thus, while the thickness of the ^{nat}Sc target material can be increased to allow for more ^{48}V to be produced with higher energy beams, the gain becomes marginal at some point. As such, the supplied α particle beam energy should be somewhere in the 20 to 25 MeV range, which is when other reactions become more prominent

than the ^{45}Sc(α, n)^{48}V reaction. To further refine the incident α beam energy, the induction of the ^{45}Sc(α, γ)^{49}V reaction, which has not been measured experimentally yet, must be considered as it affects the purity of the produced ^{48}V with respect to ^{49}V.

Using predicted excitation functions from TALYS reaction code for the production of radionuclides can give sufficiently accurate estimates, but it would be better to verify those predictions with measured data. To understand what measurements would be desirable in this case, consider Equation 3.1, which describes the production rate for a radioactive residual nucleus of an α-induced reaction on a thick ^{45}Sc target:

$$\frac{dN_i(t,E)}{dt} = \frac{\rho_{Sc} N_{AV}}{M_{Sc}} \phi(t,E)\sigma(E) + \lambda_i N_i(t,E) \tag{3.1}$$

where N_i is the number of atoms of residual nuclide i, ρ_{Sc} is the density of ^{45}Sc in g/cm^3, N_{AV} is Avogadro's number, M_{Sc} is the molecular weight of ^{45}Sc in g/mol, ϕ is the flux of the α particles in particles/s (i.e. $\phi(t,E) = \frac{i_\alpha(t,E)}{q_\alpha}$, where $i_\alpha(t,E)$ is the measured current and q_α is the charge of an α particle), σ is the cross-section for the α-induced reaction, E is the incident α particle energy, and t is the irradiation time.

If a tandem Van de Graaff accelerator is utilized to produce the incident particle beam, then the beam is monoenergetic and the flux and cross-section do not depend on energy. However, the cross-section depends on the distance the beam travels within the target material (due to energy loss) and the flux may fluctuate over the course of the irradiation. Furthermore, if the irradiation is much shorter than the half-live of the residual nucleus, say an irradiation over the course of a few hours for a radionuclide with an approximately 2 week half-live, then the second term in Equation 3.1 becomes negligible. If ratio of two residual nuclei of two types of nuclear reactions of an incident particle beam and the target were to be expressed with these assumptions, then the following would be obtained when attempting to integrate the production rate equations for the

residual nucleus in each reaction (assuming ^{45}Sc(α, n)^{48}V and ^{45}Sc(α, γ)^{49}V are the reactions of interest):

$$\frac{N_{48_V}}{N_{49_V}} = \frac{\iint \frac{\rho_{Sc} N_{AV}}{M_{Sc}} \phi(t) \sigma_{48_V}(x) \mathrm{dxdt}}{\iint \frac{\rho_{Sc} N_{AV}}{M_{Sc}} \phi(t) \sigma_{49_V}(x) \mathrm{dxdt}} \tag{3.2}$$

where x is the distance into the target material in line with the particle beam. The only difference between the numerator and the denominator in Equation 3.2 is the cross-sections, which are independent of time. This simplifies Equation 3.2 to the following:

$$\frac{N_{48_V}}{N_{49_V}} = \frac{\int \sigma_{48_V}(x) \mathrm{dx}}{\int \sigma_{49_V}(x) \mathrm{dx}} \tag{3.3}$$

Computing these integrals results in the average cross-section for those production reactions over the thickness of the target material. To approximate this from measured data in the literature or calculated data from reaction codes, these cross-sections need to be rewritten in terms of energy. When positively charged ion beams enter materials, they do not always undergo nuclear reactions with the nuclides in the target material to become new nuclides. In most cases, they lose their energy through elastic or inelastic scattering via Coulomb interactions with the electrons surrounding the target nuclei as they travel through the material before they eventually are stopped [19,21]. The rate at which these charged particles lose their energy to the surrounding material is called the stopping power of the material, S, which is expressed as $S(E) = \frac{dE}{dx}$. By multiplying each of the integrals in Equation 3.3 by the stopping power, the ^{48}V/^{49}V production ratio becomes dependent upon energy as follows:

$$\frac{N_{48_V}}{N_{49_V}} = \frac{\int \sigma_{48_V}(x) \mathrm{dx}}{\int \sigma_{49_V}(x) \mathrm{dx}} \cdot \frac{\frac{dE}{dx}}{S(E)} \cdot \frac{S(E)}{\frac{dE}{dx}} = \int \frac{\sigma_{48_V}(E)}{S(E)} dE \cdot \int \frac{S(E)}{\sigma_{49_V}(E)} dE \tag{3.4}$$

If an irradiation is performed and measurements were conducted for the beam current and the activity of the residual nuclei in this equation, then the cross-sections of each reaction shown in

Equation 3.4 could be determined as a function of energy if the stopping power is included in the calculation as well. With the stopping power function being the same in the numerator and the dominator, the only difference really is the excitation function for each reaction over the range of expected beam energies within a ^{nat}Sc target. Taking this into consideration, it can be seen in Figure 3.1 that the $^{45}Sc(\alpha, \gamma)^{49}V$ excitation function follows a similar shape to the $^{45}Sc(\alpha, n)^{48}V$ excitation function; albeit, being much lower in magnitude. Being able to compare the $^{45}Sc(\alpha, n)^{48}V$ and $^{45}Sc(\alpha, \gamma)^{49}V$ cross-sections somewhere where both reactions are the most prominent would be the most useful for determining the accuracy of the predictions from the TALYS reaction code.

To determine the thickness of the ^{nat}Sc target, the stopping power of an α particle beam in ^{nat}Sc and the average range the α particles impinging upon the target will travel must be predicted. The stopping power is a function of some properties of the projectile ion (mass, charge, and velocity) and the atomic number and density of the target material. Bethe and Bloch derived an expression for the stopping power of an ion [21]. If the stopping power was plotted against the penetration depth of an ion in a material, then the Bragg curve would be obtained. The Stopping and Range of Ions in Matter (SRIM) code is based on the Bethe-Bloch expression along with several other stopping theories, such as Brandt-Kitagawa and LSS theory [78]. From these calculations, ion range distributions can be obtained within 5% of their actual values. Using SRIM to determine the ion range distribution for the majority of 24.3 MeV α particles in ^{nat}Sc results in the calculated range of 268.98 μm of ^{45}Sc. The computed distance is actually not an exact value because straggling inevitably occurs as the energy loss of the particles is a statistical or stochastic process. Straggling causes the energies of an ion beam passing through material to broaden [19]. Recall that the range of the α particle beam and the stopping power of the ^{nat}Sc material need to be

considered when determining the thickness of the ^{nat}Sc target material to determine the cross-section of the ^{45}Sc(α, γ)^{49}V reaction, and ultimately the achievable atomic ^{48}V/^{49}V ratio. In this case, by fitting stopping power data obtained using SRIM, 24.3 MeV α particles are expected to leave a 254 μm thick ^{45}Sc target with an average energy of about 4 MeV, which is near the threshold the ^{45}Sc(α, n)^{48}V reaction. This suggests a foil stack of two 127 μm ^{nat}Sc foils and an α beam energy of 24.3 MeV would allow for the atomic ^{48}V/^{49}V ratio to be measured over two energy ranges where the ^{45}Sc(α, n)^{48}V and ^{45}Sc(α, γ)^{49}V reactions are the most prominent.

3.2.2 Post-Irradiation Processing

Post-irradiation, the produced radionuclide of interest needs to be separated from the bulk target material and other radionuclides. This process typically involves comparing the distribution coefficients of the radionuclide of interest, the bulk material, and any undesired impurities. Recall from Section 2.2.2 that the distribution coefficient describes the partitioning of a metal ion between the solid resin and the solution. This value depends on a variety of factors including the amount of resin, the metal ion concentration in the solution, and even the presence of competing metal ions. As such, the actual distribution coefficients may vary from experiment to experiment. However, in general, a good first step when deciding which resins could be used for the anticipated separation task is to consult tabular data that depicts measured distribution coefficients for various elements and resins or organic extractants as a function of acid concentration. Suitable sources include Ichikawa et al. and Kraus and Nelson for anion exchange resin [79,80], Ishimori and Nakamura for various organic extractants, which can be partially extended towards extraction chromatographic resins [81,82], and Pourmand and Dauphas for *N*,*N*,*N*′*N*′ tetraoctyl-1,5-diglycolamide (TODGA) resin [83]. Once identifying the distribution coefficients for two elements that need to be separated, the separation factor, f_S, can be determined using the following

equation only if the distribution ratios for those elements do not depend on the composition of the solvent and extractant phases (i.e. the distribution ratios are equal to the distribution coefficients):

$$f_s = \frac{\mathrm{K}_{d_l}}{\mathrm{K}_{d_s}} \tag{3.5}$$

where K_{d_l} is the larger K_d value and K_{d_s} is the smaller K_d value. The larger the separation factor, the better the separation will be assuming the resin capacity is large enough to allow for complete adsorption of the element with the high K_d value. With isotope harvesting, the resin capacity should not be a limiting factor because there is no bulk material [75]. Once the resins for the separations have been chosen, studies need to be performed to ensure there are no kinetic limitations to the ion exchange or extraction chromatography process.

For ion exchange reactions, the actual exchange of ions at exchange sites in the resin matrix is typically very fast, which means the reaction is controlled by the rate of diffusion of the ions to the exchange sites [67,69,70]. In extraction chromatography, the reaction is also usually controlled by the rate of diffusion of the ions in the mobile phase but can be controlled by the kinetics of the reaction between the metal ion and the extractant. Typically, these limitations in a separation on an extraction chromatographic resin can be minimized by utilizing a slow flow rate [81]. In addition to temperature, the physical characteristics of the resin matrix, such as the degree of crosslinking, particle size, and dimensions of the resin bed, affect the rate of reactions in both ion exchange and extraction chromatographic resins. In general, the rate of reaction decreases as the degree of crosslinking increases and the particle size increases, while it increases as temperature increases [69,81]. Meanwhile, the column length is important for the breakthrough capacity of the bed and the sharpness of the eluted ion concentration when measuring the elution profiles for ions of interest.

3.3 Production via α-Irradiated ^{nat}Sc Foil

Of the two ^{48}V production methods presented within this chapter, the ^{48}V production by α-irradiation of a ^{nat}Sc foil is more conventional. Many studies have measured the ^{45}Sc(α, n)^{48}V excitation function over a range of incident α particle energies; however, none of these studies have measured the ^{45}Sc(α, γ)^{49}V excitation function [31–33,35,36]. As mentioned in a previous section (Section 3.2.1), it would be desirable to measure cross-sections for the ^{45}Sc(α, γ)^{49}V reaction for incident α energies where both the ^{45}Sc(α, n)^{48}V and ^{45}Sc(α, γ)^{49}V reactions are prominent. This would help discern the accuracy of the TALYS reaction code to predict the production rate of ^{49}V at different incident α particle energies. Such measurements would also determine whether this production method would be a viable method for producing ^{48}V in high enough purity with respect to ^{49}V (>10^4 atoms of ^{48}V/atom of ^{49}V), to finally enable a ^{48}V(n, γ)^{49}V total cross-section measurement with high enough precision (10 barns). The work present in this section will cover both the separation methodology and the determination of the ^{48}V/^{49}V atomic ratio. However, the ^{45}Sc(α, n)^{48}V and ^{45}Sc(α, γ)^{49}V cross-section measurements were not performed due to imprecise beam current data. Fortunately, the results from these studies still allow for a comparison to be made with the ^{48}V production via aqueous isotope harvesting.

3.3.1 Methods

There were three experimental parts to evaluate the effectiveness of this ^{48}V production method: the production of ^{48}V by bombarding ^{nat}Sc foil stacks with 24.3 MeV α particles, the separation of ^{48}V from bulk Sc, and the determination of the ^{48}V purity with respect to the amount of ^{49}V present as an impurity.

3.3.1.1 Irradiation of ^{nat}Sc Foil Stacks with α-Particles

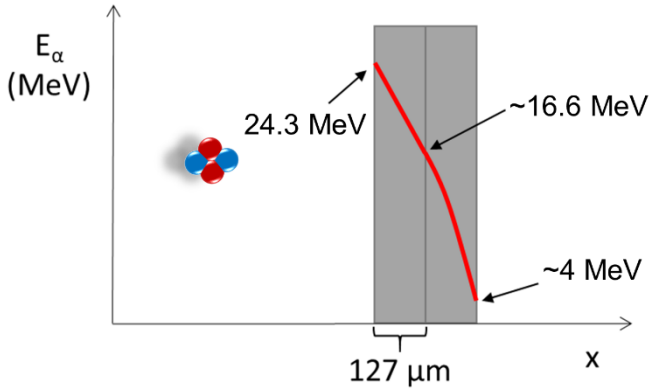

Figure 3.2: Drawing depicting the energy of a 24.3 MeV α beam as it penetrates a ^{nat}Sc foil stack. Each labelled point along the red line are average α particle energies in MeV.

Two ^{nat}Sc foil stacks, each containing two 25 mm x 25 mm x 0.127 mm thick ^{nat}Sc foils (99.999% purity, purchased from Alfa Aesar, USA), were bombarded with 24.3(2) MeV α particles produced using the FN 10 MV Tandem Accelerator at the Institute for Structure and Nuclear Astrophysics at the University of Notre Dame. The foil stacks were mounted onto a target ladder and placed directly after the pelletron chain to maximize the beam current. Figure 3.2 depicts the expected average α particle beam energy as the beam travels through a foil stack. Note that energy windows through each foil are 24.3 MeV to ~16.6 MeV and ~16.6 MeV to ~4 MeV. The target stack used to determine the atomic ^{48}V/^{49}V production ratio was irradiated for a total of approximately 7.4 hours, while the other foil stack was irradiated for about 5.75 hours. Analysis of the beam post-irradiation suggested that only $^{4}\alpha^{2+}$ particles were interacting with the ^{nat}Sc target stacks. After an approximately 1-week cooldown time, the foils were then shipped to MSU, where the chemical processing was performed. During the irradiation, a part of the target ladder, which was wrapped in Kapton tape, touched the beam pipe. The generated electrical current partially discharged to the pipe and resulted in a suppressed beam current. With no alternative method to accurately measure the beam current, the focus was shifted from assessing the cross-sections for the ^{45}Sc(α, n)^{48}V and ^{45}Sc(α, γ)^{49}V reactions to measuring the ^{48}V/^{49}V atomic ratio.

3.3.1.2 Separation of ^{48}V from Bulk Sc with Anion Exchange and a DGA Column

After the foils arrived at MSU, the corners of each foil were detached using scissors and discarded prior to dissolution. All foils (44.3 mg to 55 mg) were dissolved using 10 mL of 5 M Suprapur HCl (32%, procured from MilliporeSigma, USA). Then, 2.5 mL aliquots of these solutions were diluted using an oxalic acid (trace metals grade, 99.999%, $C_2H_2O_4$, acquired from MilliporeSigma, USA) aqueous solution of the appropriate concentration to obtain 62.5 mL 0.2 M HCl and 0.1 M $C_2H_2O_4$ solutions. These solutions were used as the load solutions to be passed over an anion exchange column containing 2 g of AG 1-X8 resin (100-200 mesh) in the Cl^- form at 0.5 mL/min. After the load solution was passed through, the anion exchange column was washed with a 125 mL 0.2 M HCl and 0.1 M $C_2H_2O_4$ solution. The ^{48}V and ^{49}V were eluted from the column using 5 M HCl. After elution, the 5 M HCl solution fractions containing ^{48}V and, presumably, ^{49}V were passed through an 80 mg *N,N,N',N'*-tetra-n-octyldiglycolamide (normal DGA resin, 50-100 µm particle size, procured from Eichrom Technologies, USA) column. Upon completion of the loading steps, the column was rinsed with 5 mL 5 M HCl solutions until no ^{48}V counts could be detected in the last 5 M HCl sample via gamma spectroscopy using a HPGe detector and analyzed using Genie2000 software to determine the amount of activity in each. All measured activities were decay-corrected to the acquisition time of the measurement of the load solution.

3.3.1.3 Separation of ^{48}V from Bulk Sc with a Single DGA Column

The 5 M HCl solutions containing ^{48}V, ^{49}V, radioscandium, and bulk Sc described in the previous section had 2.5 mL aliquots withdrawn to be used as the load solutions without further processing. These solutions were directly passed over ~1.4 g normal DGA resin columns at 0.5 mL/min. The columns were then washed with 5 mL fractions of 5 M HCl solutions until no

^{48}V counts could be detected in the last 5 M HCl sample via gamma spectroscopy using a HPGe detector and analyzed using Genie2000 software to determine the amount of activity in each. All measured activities were decay-corrected to the acquisition time of the measurement of the load solution. This method was exclusively used to separate ^{48}V and ^{49}V from the second ^{nat}Sc foil stack.

3.3.1.4 Liquid Scintillation Counting of Purified Radiovanadium Fractions

The fractions containing ^{48}V in the separation for each foil in the second ^{nat}Sc foil stack were evaporated to approximately 500 µL, weighed, and diluted to 3 mL using a HCl solution of the appropriate molarity to yield a 1.77 M HCl solution. Each of these solutions were added to 17 mL of Ultima Gold^{TM} AB scintillation cocktail (obtained from PerkinElmer, USA) in a plastic 20 mL liquid scintillation counter (LSC) vial. A blank of these solutions was also made using 3 mL of 1.77 M HCl and 17 mL of Ultima Gold^{TM} AB scintillation cocktail. All samples were vortexed for 1 minute and placed in a dark area for 24 hours prior to counting on an LSC to determine the ^{49}V activity. The samples were counted for 2 hours in 2 cycles on an almost weekly basis with a PerkinElmer Tri-Carb 4910TR LSC and the counts observed over the windows spanning 0 to 10 keV were analyzed. The samples were also vortexed for 1 minute 24 hours before counting every other week to ensure they did not settle. The samples were also measured using a HPGe detector and analyzed with Genie2000 software to quantify the ^{48}V activity.

A quench curve was obtained using ^{51}Cr and used without any further adjustment to calculate the LSC detection efficiency for ^{49}V at various levels of quenching. This was done because ^{51}Cr and ^{49}V have similar electron and x-ray emissions in terms of energy and intensity [17,38]. For the quench curve preparation and measurements, the “Method 2” procedure as described by Thomson [84] was followed with the exception of using 200,000 dpm ^{51}Cr in a

1 M HCl solution dispensed in each vial rather than ^{3}H or ^{14}C. However, ionization quenching was observed, which led to an apparent increase in detection efficiency with the samples quenched with nitromethane rather than observing an expected decrease. This effect was noticed even after remeasuring the samples 48 hours later. Because the detection efficiency for the actual ^{49}V samples was decreasing over time, the quench curve was remeasured by attempting to determine the quench caused by dilution with 1 M HCl rather than a chemical quench from the addition of nitromethane. The resulting quench curve was fitted with a logarithmic function to allow for the efficiency to be determined using the measured tSIE value of the solution. The calculated detection efficiencies for the ^{49}V samples (31-21%) was comparable to the higher end of the range of efficiencies determined by Rodríguez Barquero et al. using HiSafe II™, HiSafe III™, Ultima-Gold™, and Insta-Gel® Plus scintillation cocktails (25-8%) [85].

3.3.2 Results

3.3.2.1 Separation of Radiovanadium from Bulk Sc

Two separation methods were investigated prior to attempting to separate ^{48}V and ^{49}V from the bulk ^{nat}Sc in the most active foil stack to ensure the most effective method would be used. The anion exchange resin separates V from Sc by utilizing the presence of oxycationic V(IV) species in 0.2 M HCl solutions, which form anionic complexes with $C_2H_2O_4$, and the inability of trivalent Sc ions in these solutions to interact with the $C_2H_2O_4$ [86,87]. For the DGA resin, the distribution coefficient for trivalent Sc is much greater than that for tetravalent V in 5 M HCl solutions ($>10^4$ vs. ~5) [83]. Inserting those values into Equation 3.5 suggests that the separation factor is $>10^3$, which is excellent. This combined with the high capacity DGA resin has for trivalent metal ions makes it a suitable candidate to examine as a standalone column to remove bulk Sc and to remove any small quantity of Sc that may have eluted with the ^{48}V and ^{49}V from the anion exchange resin.

Table 3.1: Results for attempts to separate ^{48}V and ^{49}V from bulk Sc. Only samples from the front foil contained ^{47}Sc, ^{44m}Sc, and ^{44g}Sc. Those initial solutions contained 0.0176(10) µCi ^{47}Sc, 0.0298(11) µCi ^{44m}Sc, and 0.0368(26) µCi ^{44g}Sc. None of the radioscandium was observed in the final ^{48}V fractions for separations conducted with those solutions.

Separation Method	Initial ^{48}V (µCi)	^{48}V Recovered (µCi)	(%)	Volume Containing Recovered ^{48}V (mL)
2 g Anion Exchange + 80 mg DGA	0.468(7)	0.432(5)	92.4(17)	18.56(14)
1.38 g DGA	0.634(6)	0.604(4)	96.1(12)	21.60(5)

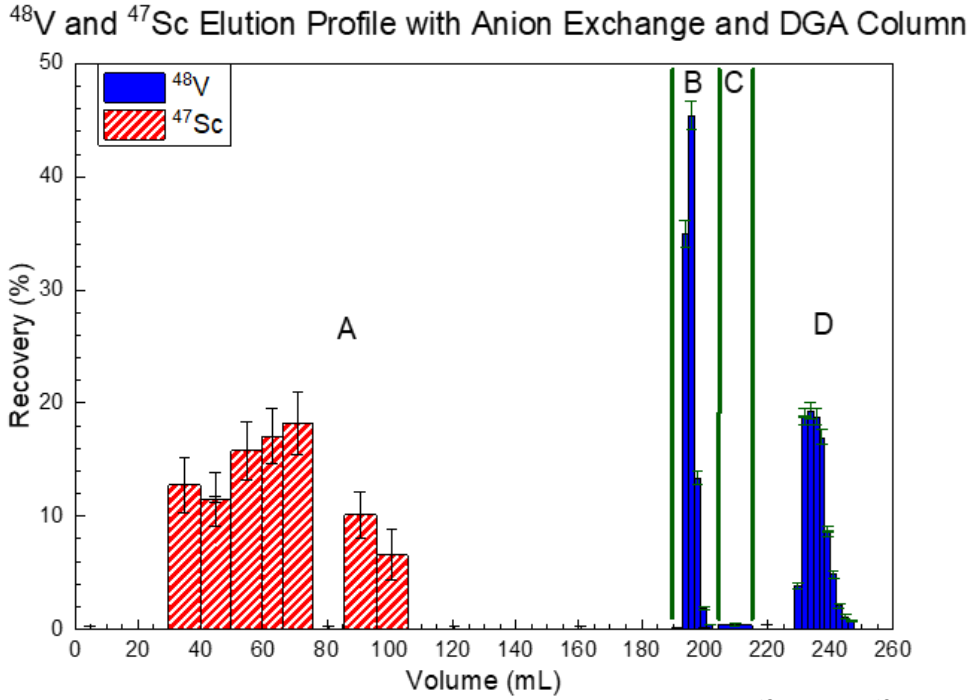

Figure 3.3: Typical elution profile obtained during separations of ^{48}V and ^{49}V from bulk Sc utilizing a 2 g AG 1-X8 anion exchange column in the Cl^- form and an 80 mg normal DGA column. All of the radioscandium passed through the anion exchange column during loading and washing with a 0.2 M HCl and 0.1 M $C_2H_2O_4$ solution (A). Most of the radiovanadium eluted from the anion exchange column with 5 M HCl (B), but a very small amount sometimes eluted with a DI H_2O rinse after the 5 M HCl rinse (C). The 5 M HCl fractions were passed through an 80 mg normal DGA column to ensure all bulk Sc was successfully separated from the radiovanadium (D). The average initial ^{48}V activity was 0.468(7) µCi. For the separations performed with the dissolved front Sc foil, the average ^{47}Sc activity was 0.0176(10) µCi. The other radioscandium present in separations performed with the dissolved front Sc foil were ^{44m}Sc and ^{44g}Sc, both of which are difficult to determine the recovery for.

The results of both separation methods are shown in Table 3.1. Typical elution profiles for separations performed with an anion exchange column in series with an 80 mg normal DGA column (Anion + DGA) and those conducted with a single large ~1.4 normal DGA column are shown in Figure 3.3 and Figure 3.4 respectively. For the Anion + DGA separations, all

radioscandium passed through the anion exchange column during loading and washing with a 0.2 M HCl and 0.1 M $C_2H_2O_4$ solution. During elution, most of the radiovanadium could be eluted from the anion exchange column with 5 M HCl, but a very small amount occasionally eluted with a DI H_2O rinse after the 5 M HCl rinse. The ^{48}V recovery after the 5 M HCl fractions were passed through an 80 mg normal DGA column was 92.4(17)%. For the separations with the single DGA column, no radioscandium was observed in the 5 M HCl loading and wash solution as it adsorbed to the resin, which resulted in a ^{48}V recovery of 96.1(12)%. Overall, the results suggest that both methods are effective at separating radiovanadium from bulk Sc with high recoveries in approximately the same volume. However, the method utilizing a single normal DGA column could be completed in a shorter amount of time and was chosen to perform the separation. Results for the separation of radiovanadium from the bulk Sc and the evaporation of the ^{48}V-containing fractions in the most active foil stack are shown in Table 3.2. High recoveries of 91.8(12)% and 91.8(10)% for the Front foil and Back foil respectively improved the chances of being able to observe counts from the decay of ^{49}V when using an LSC.

Table 3.2: Results of separations performed to recover ^{48}V and ^{49}V from the longest irradiated ^{nat}Sc foil stack. The only radioscandium the dissolved front foil contained was ^{47}Sc with an average of 0.0026(6) µCi. None of the eluted fractions from the DGA column contained ^{47}Sc.

Foil Position	Total Initial ^{48}V (µCi)	Total Recovered ^{48}V	
		(µCi)	(%)
Front (~16.6 to 24.3 MeV)	3.62(3)	3.33(3)	91.8(12)
Back (~4 to ~16.6 MeV)	8.04(6)	7.38(6)	91.8(10)

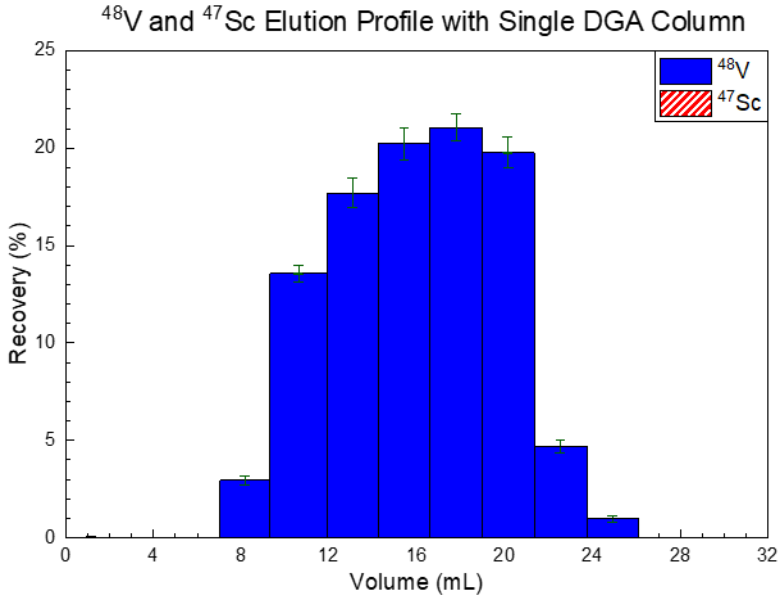

Figure 3.4: Typical elution profile for separations performed using a single ~1.4 g normal DGA column to separate ^{48}V and ^{49}V from bulk Sc. No radioscandium was observed in the 5 M HCl loading and wash solution as it adsorbed to the resin. The average initial ^{48}V activity was 0.634(6) µCi. For the separations performed with the dissolved front Sc foil, the average ^{47}Sc activity was 0.0176(10) µCi. The other radioscandium present in separations performed with the dissolved front Sc foil were ^{44m}Sc and ^{44g}Sc, both of which are difficult to determine the recovery for.

3.3.2.2 ^{48}V Radioisotopic Purity

When plotting the raw data of the counts observed in the low-energy windows of the LSC, it is apparent that both samples contain two radionuclides with very different half-lives (see Figure 3.5 on the next page). This was expected because the half-life of ^{49}V is much longer than the half-life of ^{48}V (330 days vs. 15.974 days). Thus, the initial events are the result of a combination of the decays of ^{48}V and ^{49}V. After the ^{48}V has decayed significantly enough that its contribution to the measured spectrum is negligible, then all observed events are due to the decay of ^{49}V. From this point, all of the observed counts can be assumed to be due to the decay of ^{49}V. Calculating the ^{49}V at each of these points (beyond 219 days for the Front foil sample and 225 days for the Back foil sample), decay-correcting them to the end-of-beam (EOB) time for the original irradiation, and accounting for separation efficiencies results in average ^{49}V activities of

731(27) pCi (or 27.0(10) Bq) and 1,616(23) pCi (or 59.8(9) Bq) for the Front and Back foil respectively. These results and the atomic $^{48}V/^{49}V$ ratio, which combines the calculated ^{48}V activity from the HPGe data and ^{49}V activity from the LSC data, are shown in Table 3.3. Most of the activity being in the last foil was expected considering the peaks of the excitation functions for both the $^{45}Sc(\alpha, n)^{48}V$ and $^{45}Sc(\alpha, \gamma)^{49}V$ reactions were expected to be between 10 and 13 MeV (see Figure 3.1), which falls in the range of average energies the α beam was expected to have while traveling through the second foil (see Figure 3.2). The observed atomic $^{48}V/^{49}V$ ratio in both foils suggests that this method would not be able to produce ^{48}V in high enough radioisotopic purity with respect to ^{49}V for neutron reaction measurements to be performed via the activation method.

Table 3.3: Measured end-of-beam (EOB) activities for ^{48}V and ^{49}V in a ^{nat}Sc foil stack bombarded with 24.3(2) MeV α particles. The $^{48}V/^{49}V$ atomic ratios in both foils suggests that this method would not be viable for producing ^{48}V in high purity with respect to ^{49}V (>10^4 atoms of ^{48}V/atom of ^{49}V).

Foil Position	EOB ^{48}V (μCi)	EOB ^{49}V (μCi)	atoms ^{48}V/atom ^{49}V
Front (~16.6 to 24.3 MeV)	17.5(9)	7.31(27)E-4	1160(70)
Back (~4 to ~16.6 MeV)	70.1(23)	1.617(23)E-3	2100(80)

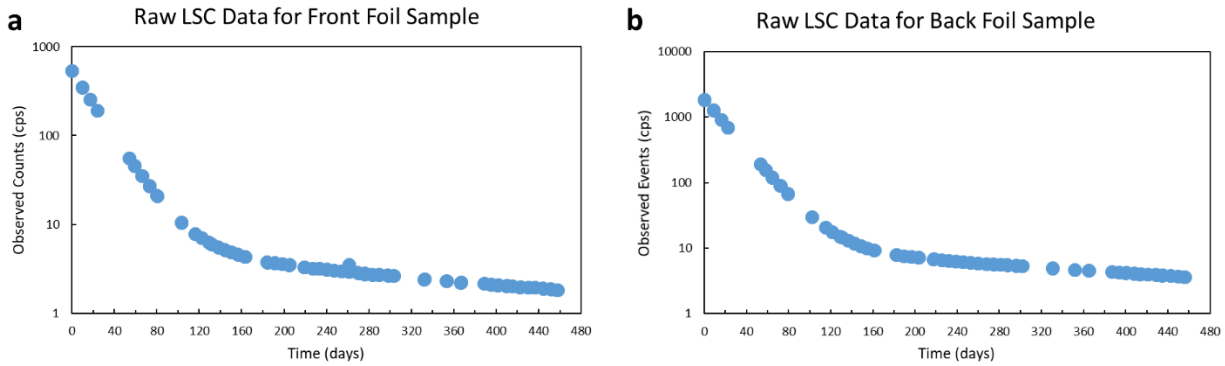

Figure 3.5: Raw observed counts per second in the low energy windows of the Tri-Carb 4910TR LSC for ^{48}V and ^{49}V extracted from an α-irradiated ^{nat}Sc foil stack. The LSC observed counts from both ^{48}V and ^{49}V in both samples over the course of about 200 days. Afterwards, the amount of ^{48}V was too small to contribute much and the overwhelming majority of the observed counts was due to ^{49}V.

While the result of this study suggests that irradiating ^{nat}Sc with α particles will not allow for the production of ^{48}V at a high enough isotopic purity with respect to ^{49}V (>10^4 atoms of ^{48}V/atom of ^{49}V), additional work still needs to be completed to verify this result. This is because the LSC sample for the ^{48}V and ^{49}V in the Back foil was observed to undergo significant color quenching in addition to the expected chemical quenching and different types of quenching can have different effects on the detection efficiency. For example, color quenching has been observed to cause a larger decrease in the detection efficiency for low-energy beta emitters, especially when significant quenching occurs [88,89]. Preliminary measurements on these samples using a Hidex 300 SL LSC have resulted in EOB ^{49}V activities of 820(230) pCi (or 30(8) Bq) and 1,250(150) pCi (or 46(6) Bq) for the Front and Back foils respectively. The Hidex 300 SL has a 3-photomultiplier tube setup rather than a 2-photomultiplier tube setup, which is what the Tri-Carb 4910TR has. This setup allows for the quenching to be measured in terms of the triple-to-double-coincidence ratio (TDCR) of the events observed by the photomultiplier tubes rather than measuring the change in the cocktail response when irradiated with gammas from an external source [90]. The result of this is different types of quenching do not have different effects on the detection efficiency when using the TDCR method [91]. The measurement of the Front foil sample obtained with the Hidex 300 SL is within error of the value measured with the 2 Tri-Carb 4910TR, while the Hidex measurement for the Back foil (the sample with higher quenching) was less than the value obtained with the Tri-Carb LSC. Although there are high errors in the Hidex 300 SL measurements, the uncertainty can be decreased by measuring a quench curve and ultimately improve the accuracy of the atomic ^{48}V/^{49}V ratio. However, even with the preliminary Hidex 300 SL measurement for the ^{49}V activity in the Back foil, the ^{48}V/^{49}V atomic ratio only increases to 2700(300), which is still lower than the desired >10^4 ratio. For >10^4 atoms of ^{48}V/atom of ^{49}V, the

amount of ^{49}V present in the Back foil at EOB would need to be <338 pCi (or <12.5 Bq), which does not appear to be obtainable with this production method.

3.4 Production via Isotope Harvesting

Isotope harvesting is a new isotope production technique that has the potential to overcome some of the issues conventional isotope production has in terms of quantity and purity of rare radionuclides. As previously described in Sections 1.2 and 3.1, mCi quantities of ^{48}V could theoretically be produced in high isotopic purity with respect to ^{49}V (>10^4 atoms of ^{48}V/atom of ^{49}V) by harvesting ^{48}Cr and setting up a ^{48}Cr/^{48}V generator. Chapter 2 covered the examination of procedures for the first step in this process, which is to extract the desired radionuclide, ^{48}Cr, from the FRIB beam dump. In this section, the studies on the necessary separations to set up a ^{48}Cr/^{48}V generator that could produce highly isotopically pure ^{48}V will be discussed.

3.4.1 Methods

For aqueous isotope harvesting, the first step in the separation and purification process for a desired radionuclide is to elute the desired radionuclide from the ion exchange resin that it accumulated on during the loading process (i.e. the continuous passing of the beam dump solution over ion exchange resin columns or cages). With the resin cages, this can be performed with a batch elution. After this step, the desired radionuclide can be chemically separated from other potential metal ion impurities and, in the case where the daughter nuclide is desired as a pure final product, allowed to generate its daughter nuclide, which can be purified to be of high purity.

For the production of highly pure ^{48}V, the desired radionuclide to harvest from the FRIB beam dump would be ^{48}Cr. After the ^{48}Cr has been harvested and separated from any V, it can generate ^{48}V that would be of high isotopic purity after it has been separated from the undecayed ^{48}Cr. When the FRIB beam dump solution is passed over cation and anion exchange resin, ^{48}Cr is

expected to accumulate on the anion exchange resin. The first step in the production process for highly pure ^{48}V is to elute ^{48}Cr from the anion exchange resin. All proceeding steps would revolve around the setup of a ^{48}Cr/^{48}V generator. It would be ideal to actually perform an experiment at FRIB or its precursor, NSCL, to demonstrate the protocols for producing highly pure ^{48}V, but due to a number of unforeseen circumstances, this was not possible. As a result, the protocols were tested using ^{48}V and ^{51}Cr radiotracers that were carrier free. Figure 3.6 shows the outline of the steps that were under study, which were also presented in a published paper [75].

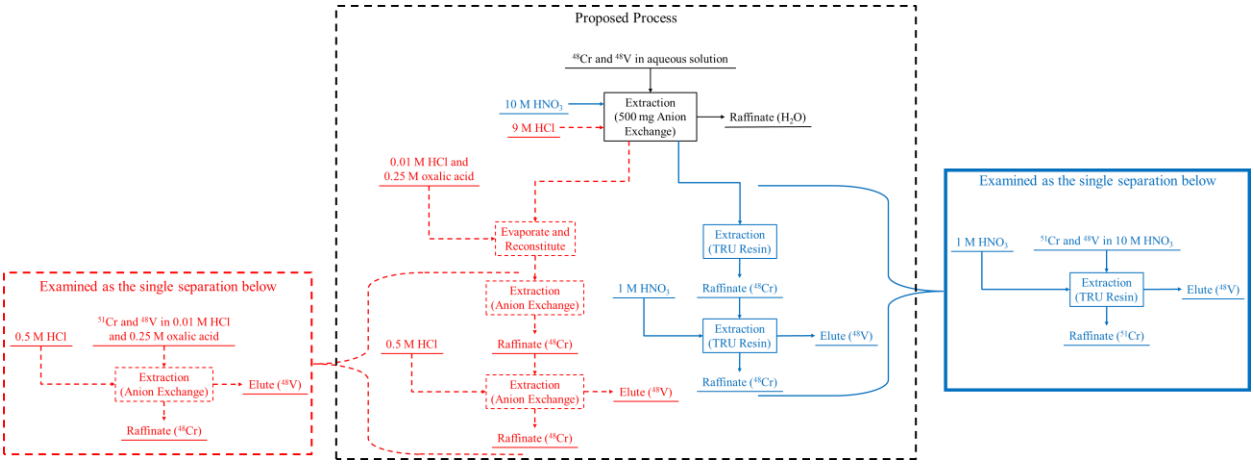

Figure 3.6: Process flow-sheet depicting possible extraction and purification processes for producing ^{48}V in high isotopic purity relative to ^{49}V via aqueous isotope harvesting at FRIB. The individual separations on the left and right of the above diagram depict how those branches were studied using ^{51}Cr and ^{48}V radiotracers as chemical analogs in place of the ^{48}Cr and ^{48}V that would be produced in the aqueous beam dump at FRIB. Reprinted from ref [75].

3.4.1.1 Batch Elution Kinetics with Stable Cr and V

The stock solution was a 20 ppm Cr and 20 ppm V aqueous solution that was prepared by diluting the Cr and V stock solutions listed in Section 2.3.1 with DI H_2O and allowing the resulting solution to equilibrate for at least 3 days. Resin cages containing 500 mg of AG 1-X8 anion exchange resin (20-50 mesh) in the OH^- form were loaded with > 99% Cr and V by continuously passing 2 gallons of an aqueous solution containing 100 ppb Cr and V through the cage at approximately 1 gpm for the equivalent time of 45 total solution passes (e.g. 1.5 hours for a 2 gallon solution with a loading speed of 1 gpm). Post-loading, the cages were placed in one of

two eluent solutions (3 mL of 10 M HNO_3 (ACS grade, 70%) or 10 mL of 9 M HCl (ACS grade, 36.5%), both procured from Fisher Scientific, USA) and shaken at 300 rpm for various lengths of time. These HCl and HNO_3 eluent solutions were chosen because the distribution coefficients for Cr in these solutions were expected to be very low [79,80]. Different eluent volumes were chosen because preliminary tests with 6-hour batch elutions found that the elution speed was too slow (i.e. the recoveries were around 50% for both Cr and V) at lower volumes for 9 M HCl. Elemental analysis by ICP-OES was performed on samples of the loading solution and the eluent to determine the total amount of extracted and eluted Cr and V. Additionally, tests were performed to determine if centrifuging the cages after loading following the procedure described in Section 2.5.1.3 (to reduce the total volume of eluent) had any effect on the maximum recoveries that could be obtained. As with the other tests, samples of the loading solution and eluent were analyzed via ICP-OES.

3.4.1.2 Batch Elution with Radiotracers

Batch elutions of ^{51}Cr and ^{48}V from resin cages containing 500 mg of AG 1-X8 anion exchange resin (20-50 mesh) in the OH^- form were performed following a procedure developed using the results from elution kinetic tests described in the preceding section (Section 3.4.1.1). The centrifuged cages from the batch extraction experiments (Sections 2.5.1.3 and 2.5.2) were placed in 2 mL of the appropriate acid (three were placed in 10 M HNO_3 (Suprapur, 65%, acquired from MilliporeSigma, USA) and the rest were placed in 9 M HCl (TraceSELECT, 34-37%, procured from Honeywell Fluka via Fisher Scientific, USA)). Each solution was shaken at 300 rpm and 25 ºC for 1 hour. Post-elution, each cage was centrifuged to remove the retained eluent and the supernatant was transferred back to the rest of the eluent solution. Gamma spectroscopy was performed on all solutions with a HPGe detector and Genie2000 software was used to analyze the

resulting spectra. All measured activities were decay-corrected to the measurement start time for the original aqueous solution that underwent batch extraction with the anion exchange resin being eluted.

3.4.1.3 Separations with Radiotracers in HCl Media

The separation process for ^{51}Cr and ^{48}V that were eluted with 9 M HCl is depicted with red, dashed lines proceeding from the batch extraction step shown in Figure 3.6. The 9 M HCl eluents obtained from the batch elution step were evaporated to dryness by using a hotplate to heat the solutions at 270 °C for approximately 2 to 4 hours. The residue was reconstituted in 1 mL of 0.1 M HCl. The resulting solution was diluted to 10 mL with a 0.278 M trace metals grade $C_2H_2O_4$ solution to produce a 0.01 M HCl and 0.25 M $C_2H_2O_4$ solution. These solutions were loaded onto 1.5 g AG 1-X8 anion exchange columns conditioned to be in the Cl^- form (note: to condition anion exchange resin to be in the Cl^- form, the 2 M NaOH step in the procedure described in Table 2.3 was replaced with 30 mL of 6 M HCl) with 100-200 mesh and 20-50 mesh resin size at 0.5 mL/min and 4 mL/min respectively. The columns were washed with 7.5 to 15 mL of a 0.01 M HCl and 0.25 M $C_2H_2O_4$ solution. The ^{48}V, loaded onto the 100-200 mesh anion exchange resin, was eluted with 21.75 to 23.25 mL of 0.5 M HCl at 0.5 mL/min. To trace the ^{51}Cr and ^{48}V, gamma spectroscopy was performed on all solutions with a HPGe detector and Genie2000 software was used to analyze the acquired spectra. All measured activities were decay-corrected to the start time of the measurement of the load solution for the columns.

3.4.1.4 Separations with Radiotracers in HNO_3 Media

The separation process for ^{51}Cr and ^{48}V that were eluted with 10 M HNO_3 is depicted with blue, solid lines proceeding from the batch extraction step shown in Figure 3.6. The obtained 10 M HNO_3 eluents from the preceding batch elution with ^{51}Cr and ^{48}V were used as the load

solutions for separations performed with TRU resin columns (50 mg cartridges obtained from Eichrom Technologies, USA) at 0.5 mL/min. After these columns were loaded, they were washed with 10 mL 10 M HNO_3 followed by the application of 2.5 mL DI H_2O to reduce the acidity of the solution surrounding the resin and to initiate the elution of ^{48}V. The remaining ^{48}V was eluted with 7.5 to 10 mL of 1 M HNO_3. Gamma spectroscopy was performed on all solutions with a HPGe detector and Genie2000 software was used to analyze the acquired spectra. All measured activities were decay-corrected to the start time of the measurement of the batch extraction eluent solution.

3.4.1.5 Radionuclidic Purity Determination

To quantify the purity of the ^{51}Cr and ^{48}V fractions recovered from all separations with TRU and anion exchange resin, the radionuclidic purity, RNP, of the recovered fractions was calculated using Equation 3.6:

$$RNP = \frac{A_i}{A_T} x\ 100\% \tag{3.6}$$

where i is either ^{48}V or ^{51}Cr, A_i is total activity of solely radiotracer i in the set of fractions containing radiotracer i, and A_T is the total activity present from both ^{48}V and ^{51}Cr in the same set of fractions.

3.4.1.6 Production Rate Estimates

The production rates of ^{48}Cr, ^{49}Cr, ^{48}V and ^{49}V in the aqueous beam dump during a 12-hour irradiation with a 160 MeV/u ^{58}Ni beam at FRIB were predicted using the nuclear reaction simulation code LISE++ [92]. Extraction and separation efficiencies observed in this study were used to determine the activities of ^{48}V and ^{49}V in the final solution containing highly pure ^{48}V. The atoms of ^{48}V/atom of ^{49}V ratio was calculated by converting the activities of each isotope in the final high purity ^{48}V solution to number of atoms by using the following well-known equation:

$$N_i = \frac{A_i}{\lambda_i} \tag{3.7}$$

where N_i is the number of atoms of radionuclide i, A_i is the activity of radionuclide i, and λ_i is the decay constant of radionuclide i.

3.4.2 Results

3.4.2.1 Batch Elution Kinetics with Stable Cr and V

The results of these batch elution experiments are shown in Figure 3.7. From this data, the optimal batch elution time appears to be 1 hour for both the 10 mL 9 M HCl and 3 mL 10 M HNO_3 solutions as that was the fastest time >90% of the Cr could be recovered within. Additional tests were performed to determine if centrifuging the cages after loading (to reduce the total volume of eluent) had any effect on the maximum recoveries that could be obtained. These results are shown in Table 3.4 on the next page and were within the error for batch elutions with the non-centrifuged cages, which suggests removing residual load solution inside of the cages had no measurable effect on the total amount of Cr and V that can be recovered via a 1 hour batch elution.

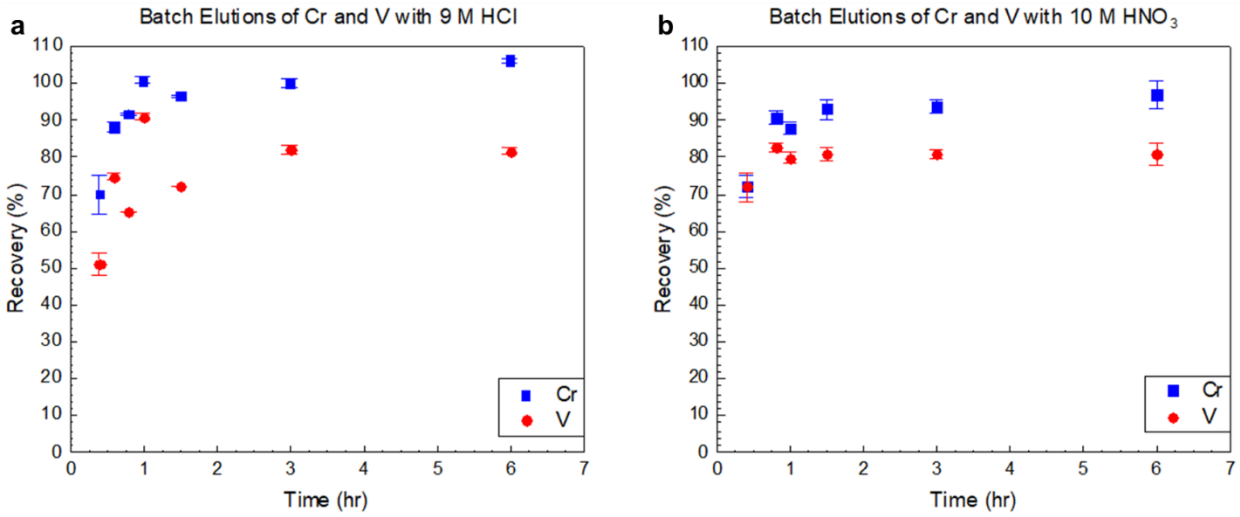

Figure 3.7: Results of batch elutions performed with 0.5 g AG 1-X8 anion exchange resin in the OH^- form in resin cages and either 10 mL of 9 M HCl or 3 mL of 10 M HNO_3 for various elution times.

Table 3.4: Results of 1-hour batch elutions performed with 3 mL of 10 M HNO_3 and 0.5 g AG 1-X8 anion exchange resin in the OH^- form in resin cages that had been either centrifuged or not post-loading of a 2 gallon aqueous solution containing 100 ppb Cr and 100 ppb V. Reprinted from ref [75].

Centrifuged? Yes/No	Cr Recovery (%)	V Recovery (%)
Yes	97.3(26)	96.7(23)
No	92.7(22)	94.9(23)

3.4.2.2 Batch Elution with Radiotracers

The ^{51}Cr and ^{48}V that were extracted from aqueous solutions using anion exchange resins were eluted with respective average recoveries of 64(3)% and 67.2(11)% for 9 M HCl and 64(4)% and 73.8(16)% in 10 M HNO_3, which can be seen in Table 3.5. Additional elution tests with 10 mL of 9 M HCl resulted in only slightly increased recovery rates for V and a significant increase for Cr (67.9(24)% for ^{48}V and 96(10)% for ^{51}Cr). However, the distribution coefficient data strongly favors the elution of these metal ions [79,80], which was also verified in experiments with stable Cr and V as recoveries were observed to be greater than 80% for both in the previous section (Section 3.4.1.1). So, these recovery rates seem lower than what could be achievable.

Table 3.5: Average 1-hour batch elution results for using 2 mL of either 10 M HNO_3 (3 trials) or 9 M HCl (5 trials) to elute ^{48}V and ^{51}Cr from 0.5 g of AG 1-X8 anion exchange resin in resin cages. All activities were decay-corrected to the start of the elution for each sample. Modified from ref [75].

Acid	Initial ^{48}V (μCi)	Recovered ^{48}V (μCi)	Recovered ^{48}V (%)	Initial ^{51}Cr (μCi)	Recovered ^{51}Cr (μCi)	Recovered ^{51}Cr (%)
9 M HCl	1.274(18)	0.859(7)	67.2(11)	0.96(4)	0.610(11)	64(3)
10 M HNO_3	1.307(24)	0.962(11)	73.8(16)	1.02(6)	0.655(16)	64(4)

These results can be explained in two ways. One is diffusion could be limiting the recoveries. With the metal ion concentration in the solution increasing, there is a point when it becomes nearly equal to the metal ion concentration in the bulk of the resin beads. When this point is reached, the concentration gradient is almost zero and mass transfer of the metal ions into the solution is slow and becomes the limiting factor in the transfer of the metal ion to the solution [69]. The other possible reason for these results is irreversible adsorption of the metal ions to the

backbone of the polymer in the resin beads and other surfaces, such as the polypropylene in the 3D-printed cages. Such irreversible adsorption to extraction chromatographic resins containing a styrene and divinylbenzene co-polymer backbone has been reported to occur due to possible defects in a very small amount of resin (<< 0.01 w/w %) [93,94]. AG 1-X8 anion exchange resin has a comparable backbone [95] and contains similar defects that could strongly interact with ^{51}Cr and ^{48}V and cause irreversible adsorption to the resin.

By repeating the batch elution experiment with resin loaded with an average of 22.5(4) µCi of ^{51}Cr and eluting with either 2 mL or 10 mL of 9 M HCl, nearly 15% more ^{51}Cr could be recovered with 10 mL of 9 M HCl than with 2 mL of 9 M HCl (see Table 3.6). This suggests that diffusion limitations are at least partially responsible for the observed decrease in the radionuclide recoveries versus the greater than 90% recoveries obtained during batch elution kinetic tests with stable metal ions. Irreversible adsorption could be responsible for at least a 5% loss of ^{51}Cr and ^{48}V, as that is about how much absorbs to the polypropylene cages during attempts to extract ^{51}Cr and ^{48}V from an aqueous solution (see Table 2.6). Thus, the reduced elution recoveries appear to be a result of diffusion limitations and irreversible adsorption to inert materials. By increasing the eluent volume, the recoveries can be improved.

Table 3.6: Results for 1-hour batch elutions conducted with 9 M HCl and 0.5 g AG 1-X8 anion exchange resin in resin cages that were loaded with ^{51}Cr from aqueous solutions containing only ^{51}Cr. Increasing the eluent volume increased the amount of ^{51}Cr that could be eluted from the resin in 1 hour. Modified from ref [75].

Eluent Volume	Initial ^{51}Cr (µCi)	Recovered ^{51}Cr	
		(µCi)	(%)
2 mL	27.4(6)	19.8(4)	72.3(22)
10 mL	17.7(4)	14.73(3)	83.1(19)

3.4.2.3 Separations with Radiotracers in HCl Media

Typical elution profiles for separations performed with anion exchange columns of two resin bead sizes and elution speeds are shown in Figure 3.8 and Figure 3.9, while the results of these separations are shown in Table 3.7. In both cases, the presence of oxycationic V(IV) species in 0.01 M HCl solutions and their formation of anionic complexes with $C_2H_2O_4$ [86] allowed for ^{51}Cr and ^{48}V to be separated. The Cr^{3+} behaves similarly to other trivalent cations in HCl solutions and does not interact with the $C_2H_2O_4$ [87]. Therefore, the Cr^{3+} passes through the column while the anionic vanadium oxalate complexes adsorb, resulting in complete separation of ^{51}Cr from ^{48}V in all but one trial. In that trial, 4.8(8)% of the ^{51}Cr eluted from the column with the first eluent fraction containing ^{48}V.

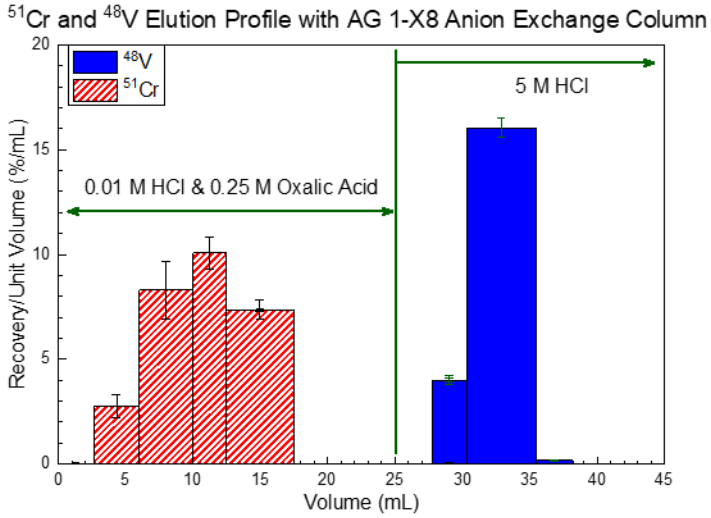

Figure 3.8: Typical elution profile of ^{48}V and ^{51}Cr separations performed at a flow rate of 0.5 mL/min with 1.5 g of AG 1-X8 anion exchange resin. The average initial ^{48}V and ^{51}Cr activities were 0.957(9) µCi and 0.634(15) µCi respectively. Reprinted from ref [75].

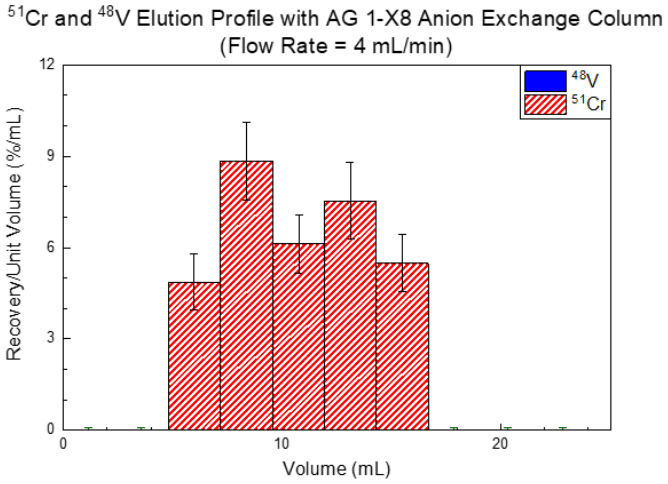

Figure 3.9: Typical elution profile of ^{48}V and ^{51}Cr separations conducted at a flow rate of 4 mL/min with 1.5 g of AG 1-X8 anion exchange resin. Nearly all of the ^{48}V adsorbed to the resin in every trial. Average initial ^{48}V and ^{51}Cr activities were 0.583(6) µCi and 0.434 µCi respectively. Reprinted from ref [75].

Table 3.7: Results for separations of ^{48}V and ^{51}Cr performed using 1.5 g AG 1-X8 anion exchange columns. No elution was conducted to recover the ^{48}V loaded onto an anion exchange column at 4 mL/min. All activities were decay-corrected to the start of loading the columns with the 0.01 M HCl and 0.25 M $C_2H_2O_4$ solution containing ^{48}V and ^{51}Cr. Modified from ref [75].

Flow Rate (mL/min)	Initial ^{48}V (µCi)	Recovered ^{48}V (%)	*RNP* (%)	Volume Containing ^{48}V (mL)	Initial ^{51}Cr (µCi)	Recovered ^{51}Cr (%)	*RNP* (%)	Volume Containing ^{51}Cr (mL)
0.5	0.957(9)	96.2(12)	99(1)	11.1(5)	0.634(15)	95.6(26)	92(2)	20.6(4)
4	0.583(6)	0.29(6)	N/A	3.61(4)	0.434(10)	79(3)	99.5(3.9)	12.86(5)

Further examination of the results in Table 3.7 reveals that attempting to quickly set up a ^{48}Cr/^{48}V pseudo-generator by rapidly passing through the 0.01 M HCl and 0.25 M $C_2H_2O_4$ load solution at 4 mL/min would allow for the ^{48}Cr to be recovered faster and in less solution volume than it would be recovered when performing the separation at 0.5 mL/min (~10 minutes and 12.86(5) mL vs. ~90 minutes and 20.6(4) mL). However, the yield of ^{51}Cr would be lower as only 79(3)% of the initial ^{51}Cr was observed to be recovered for separations performed at 4 mL/min. Higher ^{51}Cr yields were obtained with the separation being performed at the slower speed of 0.5 mL/min as 95.6(26)% of the initial ^{51}Cr could be recovered.

3.4.2.4 Separations with Radiotracers in HNO_3 Media

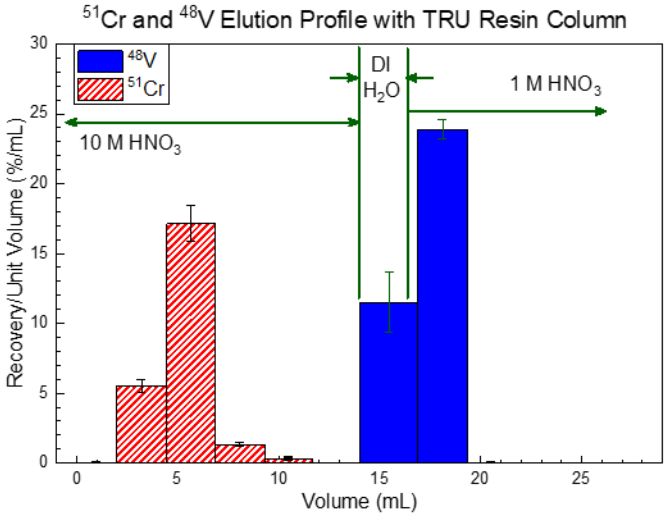

Figure 3.10: Typical elution profile of ^{48}V and ^{51}Cr separations performed at a flow rate of 0.5 mL/min with 50 mg TRU resin. Initial ^{48}V and ^{51}Cr activities were 0.962(11) µCi and 0.655(16) µCi respectively. Reprinted from ref [75].

Table 3.8: Results for separations of ^{48}V and ^{51}Cr conducted at a flow rate of 0.5 mL/min with 50 mg TRU resin columns. All activities were decay-corrected to the start of loading the columns with a 10 M HNO_3 solution containing ^{48}V and ^{51}Cr. Modified from ref [75].

Initial ^{48}V (µCi)	Recovered ^{48}V (%)	RNP (%)	Volume Containing ^{48}V (mL)	Initial ^{51}Cr (µCi)	Recovered ^{51}Cr (%)	RNP (%)	Volume Containing ^{51}Cr (mL)
0.962(11)	96.2(13)	100(1)	5.39(16)	0.655(16)	94.1(28)	100(2)	8.81(8)

The results for separations performed with ^{51}Cr and ^{48}V eluted with HNO_3 and utilizing TRU resin are shown in Table 3.8 and a typical elution profile is shown in Figure 3.10. The extractant group on TRU resin, octyl(phenyl)-N,N-diisobutylcarbamoylmethylphosphine oxide dissolved in tributyl phosphate (CMPO-TBP), has large distribution coefficients with tetravalent and hexavalent metal ions and relatively low distribution coefficients with trivalent metals ions in highly concentrated nitric acid solutions [96]. Since the ^{48}V in the 10 M HNO_3 is most likely in its tetravalent state (as evidenced by the bluish tint observed in elutions performed with stable V) and ^{51}Cr is in its trivalent state, ^{48}V had a large distribution coefficient and readily adsorbed to the TRU resin, while ^{51}Cr had a low distribution coefficient and passed through during the loading step. The acid dependency, which is roughly proportional to the distribution coefficient, of all ions in

CMPO-TBP tends to decrease as the acid concentration in the aqueous phase decreases [96]. Thus, any retained ions should elute more readily with solutions of lower acidity. This was observed with the ^{48}V promptly eluting when DI H_2O and 1 M HNO_3 are passed through the TRU resin column. In all trials, ^{51}Cr and ^{48}V were successfully separated from each other with the radionuclidic purities of the fractions containing them being 100(2)% and 100(1)% respectively. Also, ^{51}Cr and ^{48}V had high recoveries in small solution volumes (94.1(28)% in 8.81(8) mL and 96.2(13)% in 5.39(16) mL respectively).

3.4.2.5 High Purity ^{48}V Production Rate Estimates

For production of ^{48}V in high isotopic purity relative to ^{49}V via aqueous isotope harvesting, the first step in the process would be to extract ^{48}Cr from the FRIB beam dump aqueous solution using anion exchange resin in the OH^- form possibly contained in a resin cage. The subsequent step would involve eluting the ^{48}Cr along with other absorbed metal ions, which would include low-purity ^{48}V, from the anion exchange resin using the novel batch elution process described in Sections 3.4.1.2 and 3.4.2.2. After the ^{48}Cr has been eluted, it can be separated from the low purity ^{48}V. The isolated ^{48}Cr would then be a pseudo-generator that would generate highly pure ^{48}V. The final separation step would isolate the pure ^{48}V from the undecayed ^{48}Cr, ^{51}Cr, and stable Cr isotopes.

From the proposed separation schemes depicted as two branches (one with solid blue lines and the other with dashed red lines) in Figure 3.6, the branch that would result in the highest yield of ^{48}V with the least contaminants would be the one that utilizes TRU resin and 10 M HNO_3. This is because the separations performed with TRU resin had high recoveries of the ^{51}Cr and ^{48}V radiotracers with both being collected in smaller fractions with better radionuclidic purities than could be obtained with separations conducted with anion exchange resin (see Table 3.7 and

Table 3.8). Accounting for the recoveries observed in the experiments described in the preceding sections and delays to allow any collected ^{49}Cr to decay to ^{49}V prior to performing any Cr and V separations, Table 3.9 on the next page lists the amount of ^{48}V along with the isotopic purity with respect to ^{49}V that can be produced via aqueous isotope harvesting of ^{48}Cr and following the separation steps outlined for the TRU resin separation that utilizes 10 M HNO_3. These results suggest that an appreciable amount of ^{48}V can be produced in high isotopic purity with respect to ^{49}V. Because any additional columns or cages place in parallel will result in an increase in the daily production rate, there is potential to produce mCi levels of highly pure ^{48}V (up to 8.9 mCi/day and 8.3 mCi/day for a purity of $>10^4$ atoms of ^{48}V/atom of ^{49}V with twenty-five 1.5 g anion exchange cages and twenty-five 1.5 g packed anion exchange columns respectively). These levels could also be attained for ^{48}V with a ^{48}V/^{49}V atomic ratio of $>10^8$ as twenty-five 1.5 g anion exchange cages and twenty-five 1.5 packed anion exchange columns in parallel would yield up to 6.3 mCi/day and 5.9 mCi/day respectively. Alternatively, the line to the two 50-gallon ion exchange resin drums could be closed during collection attempts for isotope harvesting. In this configuration, the beam dump solution can be continuously passed over the 1.5 g of anion exchange resin in either a cage or a column until the harvesting is stopped, which depends on the desired purity (i.e. for ^{48}V of higher isotopic purity, the solution can be passed over the anion exchange resin for longer periods of time than for lower isotopic purity, which reduces the losses of ^{48}Cr due to radioactive decay post-irradiation). With this configuration, the production rate for ^{48}V with an isotopic purity of $>10^4$ atoms of ^{48}V/atom of ^{49}V would be up to 2.1 mCi/day and 1.9 mCi/day for a 1.5 g anion exchange cage and column respectively. Meanwhile, for ^{48}V with a ^{48}V/^{49}V atomic ratio of $>10^8$, this value would respectively be up to 2.0 mCi/day and 1.9 mCi/day for a 1.5 g anion exchange cage and column. As a result, isotope harvesting can potentially produce more than enough ^{48}V in

high isotopic purity that meets or exceeds the required $^{48}V/^{49}V$ atomic ratio ($>10^4$ atoms of ^{48}V/atom of ^{49}V) for total cross-section measurements performed using the activation method.

Table 3.9: Estimated daily production rates for pure ^{48}V obtained from ^{48}Cr extracted from the FRIB beam dump on a single anion exchange column or cage in series with a cation exchange column or cage. The extraction efficiencies reported in Table 2.4 and all recoveries with batch elutions and Cr and V separations performed in 10 M HNO_s media (see Table 3.5 and Table 3.8) were used to calculate these values.

	$>10^4$ (atoms ^{48}V/atom ^{49}V)	$>10^5$ (atoms ^{48}V/atom ^{49}V)	$>10^8$ (atoms ^{48}V/atom ^{49}V)
1.5 g Packed Column	330 µCi/day	290 µCi/day	240 µCi/day
1.5 g Resin Cage	350 µCi/day	310 µCi/day	250 µCi/day
0.5 g Resin Cage	310 µCi/day	270 µCi/day	220 µCi/day

3.5 Isotope Production Method Comparison

Considering the results obtained from the work described in Sections 3.3 and 3.4, producing ^{48}V via aqueous isotope harvesting is the best method for producing mCi quantities of ^{48}V that is pure enough to conduct total cross-section measurements with the activation method. Irradiating ^{nat}Sc foil with α particles could produce ^{48}V in a higher isotopic purity with respect to ^{49}V than the traditional proton irradiation of an enriched ^{48}Ti foil ($>10^3$ atoms of ^{48}V/atom of ^{49}V vs. $\sim10^2$), but this would only allow for a total cross-section measurement of the $^{48}V(n, \gamma)^{49}V$ reaction to be made with a precision of about 100 barns instead of the desired 10. With isotope harvesting, this purity requirement can be met or even exceeded. The results in Table 3.9 suggest that an appreciable amount of ^{48}V can be produced with a $>10^8$ $^{48}V/^{49}V$ atomic ratio. It must be stressed that this estimate is a worst-case scenario estimate that assumes only about 3% (with resin cages, 0.6% with packed columns) of the beam dump loop water will actually pass through a 1.5 g cation exchange resin cage or packed column and anion exchange resin in either a cage (1.5 g or 0.5 g) or packed column (1.5 g) in series in the isotope harvesting portion of the beam dump clean up loop while the rest of the solution passes through two 50 gallon ion exchange resin drums. With improvements in both the isotope extraction and elution process, these daily production rates can be improved to yield mCi levels of ^{48}V.

3.6 Concluding Remarks

Two ^{48}V production methods were compared to determine the most effective method for producing mCi quantities of ^{48}V in high enough purity with respect to ^{49}V. One method was a conventional method that involved bombarding a metal foil with a beam of charged particles. In this case, ^{48}V was produced by irradiating ^{nat}Sc foil with α particles. This resulted in ^{48}V being produced in a higher purity than what could be obtained with the conventional proton irradiation of an enriched ^{48}Ti foil (>10^3 atoms of ^{48}V/atom of ^{49}V vs. ~10^2), but the purity will still not allow total cross-section measurements to be made with a precision of 10 barns using the activation method. The other method examined in this chapter involved producing ^{48}V through the novel isotope harvesting method. Although a proof-of-concept study could not be performed at FRIB, experiments were conducted using carrier free ^{51}Cr and ^{48}V radiotracers. The results from these studies suggest that ^{48}V can be produced in appreciable quantities and high enough isotopic purity (up to >10^8 atoms of ^{48}V/atom of ^{49}V) that meets or exceeds the requirements for performing cross-section measurements with the activation method for a precision of 10 barns to be possible (>10^4 ^{48}V/^{49}V atomic ratio). From the work completed in this dissertation, the best isotope production method for producing mCi quantities of ^{48}V in high isotopic purity relative to ^{49}V is isotope harvesting at FRIB.

CHAPTER 4: ^{48}V TARGET PRODUCTION METHODS FOR NEUTRON REACTION STUDIES

4.1 Overview

After producing ^{48}V, the last step before nuclear reaction measurements can be made is to fabricate a target for such studies. For measurements performed with the activation method, which would allow for the possibility for measuring the total cross-section for the ^{48}V(n, γ)^{49}V reaction, the target nuclide isotopic purity is the most important quantity. However, a sufficient amount of outgoing charged particles need to be measured as part of a direct reaction measurement if any cross-section measurements are to be made for the ^{48}V(n, p)^{48}Ti reaction. In this case, the thickness and uniformity of the target are important characteristics to consider. Two target production methods were examined in this dissertation: a conventional electrodeposition method and a new controlled drop deposition method. This work aimed to identify the best method for manufacturing a ^{48}V target for these direct measurement studies of neutron-induced charge particle reactions, which, by extension, could be used to fabricate a target for neutron reaction studies via the significantly less resource-intensive activation method.

4.2 Background and Theory

The requirements of a target for nuclear reaction studies strongly depend on the measurement technique the target will be used in. The activation method requires the target to be high in isotopic purity and able to be irradiated in a nuclear reactor. As such, the target preparation method can be as straightforward as the method utilized by Shusterman et al. when producing a target for measurements of the total neutron capture cross-section for ^{88}Zr [10]. In this case, the purified ^{88}Zr was present in a concentrated HCl solution and evaporated to dryness. The resulting ^{88}Zr solid residue, which was most likely [^{88}Zr]$ZrCl_4$, was placed in a quartz ampule and flame-

sealed shut. This sample could be safely inserted into the University of Missouri Research Reactor together with other flame-sealed ampules containing monitor foils to assess the total neutron capture cross-section via the activation method [10]. A similar sample could be made with pure ^{48}V; however, this would only allow for measurements to be made on the total neutron capture cross-section. Other reactions of interest, such as the ^{48}V(n, p)^{48}Ti reaction, which produces a stable nuclide, cannot be measured with high enough precision at any point pre- or post-irradiation. For that reaction, the best measurement technique would be a direct reaction measurement that allows for the real time detection of the outgoing charged particles and the incident neutrons can be measured via a time-of-flight technique. The low-energy neutron-induced charged particle detection system (LENZ) allows for direct measurements to be made of these reactions. This system can be installed on a flight path in the Weapons Neutron Research (WNR) facility at the Los Alamos Neutron Science Center (LANSCE), where a linear accelerator that is capable of accelerating protons up to 800 MeV is housed. By bombarding a tungsten spallation target with this proton beam, a white neutron source is generated [97]. Samples can be exposed to the pulsed neutron beam in various instrumental setups located on any of the flight paths, including the LENZ system, which allows for neutron-induced charged particle reactions to be studied.

The LENZ instrument has been used to study neutron-induced charged particle reactions on both stable [98–100] and radioactive [101] targets at LANSCE. It allows for the possibility of reconstructing the Q value for neutron-induced charged particle reactions by using the measured incident neutron time-of-flight (note that this is proportional to the inverse of the neutron energy) and measured charged particle energy and angle from the beam axis. The charged particles are detected using annular S1-type double-sided silicon strip detectors (DSSD) in an arrangement that provides coverage over a range of angles relative to the beam axis and target (both downstream

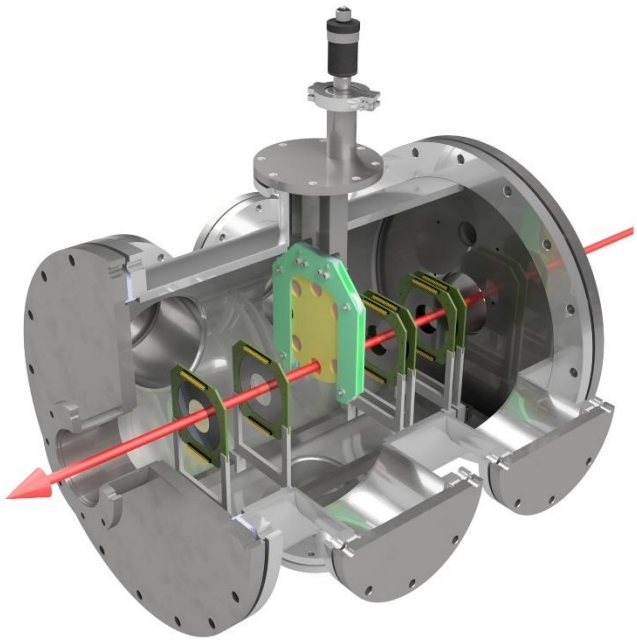

Figure 4.1: Diagram of one possible configuration of the LENZ instrument. The red arrow depicts the incident neutron beam, which would undergo neutron reactions with the target it is intersecting on the target wheel in the center of the image. DSSDs shown upstream and downstream from the target allow for the detection of outgoing charged particles at backward and forward angles respectively. Reprinted from ref [103] with permission from Elsevier.

and upstream) (see Figure 4.1). The annular shape of the DSSDs facilitates that most of the detected charged particles evolve as products of compound and pre-compound nuclear reactions rather than products of direct nuclear reactions. This is due to the tendency of the products of direct reactions to emit in the incident projectile direction, while the products of compound and pre-compound reactions are emitted primarily isotropically [18]. Direct nuclear reactions occur over a very short timescale (~10^{-22} s) and one possible channel is a direct two-body transfer of the projectile with a nucleon in the target nucleus. Compound nuclear reactions occur over a much larger timescale (10^{-15}-10^{-18} s) and involve the formation of an intermediate reaction product, called a "compound nucleus", which decays by various means into the residual nucleus once it reaches a state of statistical equilibrium. Pre-compound nuclear reactions occur on a timescale between those for direct and compound reactions and involve the emission of reaction products before the compound nucleus can reach a state of statistical equilibrium. Because a particle can

populate different energy levels within the intermediate reaction product for compound and pre-compound reactions, two neutron-induced charged particle reactions with the same target nuclide and same emitted charged particle can have different reaction Q values [102]. Thus, the LENZ instrument can measure partial cross-sections for reactions that result in the emission of a charged particle from different levels within the compound nucleus (e.g. for an emission from the ground state and first state, the reaction would be written as (n, x_0) and (n, x_1) respectively, where x is a charged particle, such as p, α, or d) [103]. Much like how the general production rate for a residual nucleus is the sum of all partial reactions that produce it, as shown in Equation 4.1, the overall cross section, σ_{total}, for a particular neutron-induced charged particle reaction, (n, x), is equal to the sum of the partial reaction cross-sections as follows:

$$\sigma_{total} = \sum_i \sigma_i + \sigma_{cont} \tag{4.1}$$

where $\sum_i \sigma_i$ is the summation of the cross-sections for each partial reaction that results in an emission of charged particle x from the ith discrete state and σ_{cont} is the cross-sections for reactions that result in the population of the continuum during the formation of the compound nucleus. To be able to measure these reactions with the LENZ instrument, the target needs to be thin with relatively good uniformity. A target that is too thick will attenuate the outgoing charged particles and lead to the band broadening for each partial reaction in the obtained spectrum, impeding the accumulation of adequately resolved events over the course of a run. This results in too large uncertainty in the measurement.

For radioactive targets, the thickness of the deposited film is less of a concern as the amount of material will probably not be enough to significantly attenuate outgoing charged particles. This becomes apparent when attempting to determine the amount of ^{48}V required in a target for measurements of neutron-induced charged particle reactions with the LENZ instrument. To make

this estimate, the typical values for the neutron flux experienced in the 15R flight path in the WNR facility [97] along with the position and detection efficiency for the LENZ instrument [99] can be leveraged. With these values, theoretical $^{48}V(n, p)^{48}Ti$ cross-section data from the JEFF 3.3 nuclear data library [22], and assuming the beam spot equals the target cross-sectional area of 1 cm^2, the initial amount of ^{48}V required to observe 1,000 events over the course of a 4 week irradiation at LANSCE can be calculated and found to be at least approximately 250 mCi (note that this does not necessarily need to be sourced from FRIB because the isotopic purity of ^{48}V is not a major requirement for this target). For a uniform target covering an area of 1 cm^2, the maximum thickness would be about 8 nm assuming the deposited ^{48}V was present as only $[^{48}V]V_2O_5$. This is much lower than the maximum thickness that low energy α particles (< 3 MeV) are stopped completely in, which is about 8.35 μm (from SRIM calculations). However, the material should be dispersed evenly over the entire incident beam area to minimize the measurement time and error due to a complex target geometry. Thus, uniformity should be of higher importance for radioactive targets. Target thickness is still tied into this characteristic though because with two targets containing the same amount of material, the target with thicker deposits would in theory have a lower surface coverage and is more likely to be less uniform than the target with thinner deposits.

Ever since the 1950's and 1960's, two inexpensive state-of-the-art techniques for producing thin and uniform radioactive nuclear reaction targets with high yields are electrodeposition and molecular plating [104–107]. Recent examples of these techniques being utilized to fabricate thin targets for nuclear reaction studies include ^{171}Tm and ^{147}Pm targets manufactured via molecular plating for neutron capture reaction studies [108] and $^{58,59}Ni$ electrodeposited targets for neutron-induced charged particle reaction studies [99]. These targets successfully allowed for measurements on either neutron capture [109,110] or neutron-induced

charged particle reactions [99]. However, not all metals can be electrodeposited or molecular plated, and impurities from the solutions, such as from the electrolyte or some other component of the solutions, can contaminate the final deposited film [105,111–113]. Alternative radioactive target manufacturing techniques tend to either be expensive, such as melting by levitation, or can have other limitations in terms of thickness (e.g. sedimentation produces thick targets), yield (e.g. vacuum evaporation has low yields), or solution formulation (e.g. electrospray deposition requires complex solutions to enable deposition) [104,114]. Maugeri et al. investigated an automated micropipette setup to produce ^{7}Be targets for nuclear reaction studies, but the µL droplet volumes were too large to allow for a uniform layer to be produced [115]. Thus, a new alternative method is required if electrodeposition or molecular plating cannot be used to fabricate a ^{48}V target for neutron-induced charged particle reaction studies.

4.2.1 Microjet Printing and Radioactive Targets

Haas et al. recently demonstrated that using a Drop-on-Demand (DoD) printer may allow for controlled deposition of droplets that are small enough in volume to produce uniform targets for nuclear reaction studies [116]. The authors reported printing droplets that were on the order of nanoliters in volume with good control in both volume and x-y application. The system was used to produce a ^{171}Tm target for nuclear reaction studies via the activation method [117]. This technique will be referred to as "microjet printing" because the droplets printed by these systems tend to form micrometer-sized sessile drops on surfaces that are not too hydrophilic or too hydrophobic. With the production of sessile droplets in the micrometer range rather than in the millimeter range, like those obtained with the automated pipetting system, microjet printing has a greater potential to manufacture targets with adequate uniformity. The deposition substrate requires sufficient heating to minimize the occurrence of the so-called "coffee ring effect," which

would result in the metal salt or oxide of interest depositing around the edges of an evaporating sessile droplet rather than uniformly or in the center of the droplet [118].

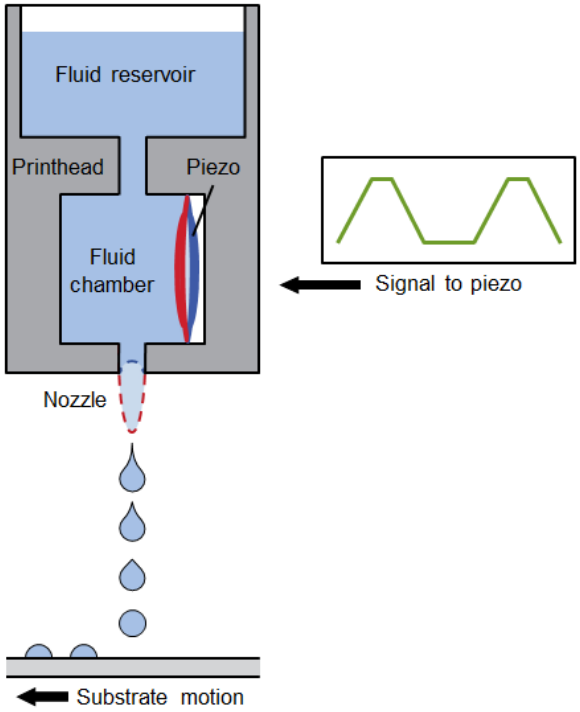

Figure 4.2: Diagram depicting the working principle behind a microjet printer. If the fluid is flush with the orifice of the nozzle and the appropriate waveform is delivered to the piezoelectric actuator (labelled as piezo), then a stream of droplets can be dispensed. Moving the substrate controls the location droplets are deposited.

The working principle behind a DoD or microjet printer is exemplified in the schematic shown in Figure 4.2. First, the fluid to be printed must be delivered to the orifice in the nozzle. In Figure 4.2, gravity pulls the fluid to the orifice in the nozzle, while other printers require another delivery system, such as a pneumatic system that applies pressure to the back of the fluid. Whichever is the case, the fluid needs to be flush with the nozzle opening and held in place by its surface tension. To produce a stream of droplets, pressure waves need to be produced within the fluid to displace the fluid at the orifice of the nozzle and for droplets to be pinched off during the displacement. This can be executed by using either a heating element that introduces a small vapor bubble or a piezoelectric actuator [119]. Allowing a heating element to come into direct contact

with a radioactive solution would increase the risk of the printer becoming contaminated and some of the radionuclide of interest being lost to the printer [116]. Therefore, using a piezoelectric actuator, like the one shown in Figure 4.2, would be preferred. Upon receiving an electrical signal, the piezoelectric actuator will expand and contract to produce the pressure waves within the fluid. The components of this signal are depicted in Figure 4.3. The optimal values for these parameters depend on many variables including properties of the fluid itself (e.g. surface tension and viscosity) and the geometry of the nozzle and the channel containing the fluid between the piezoelectric actuator and the orifice of the nozzle [120]. After the optimal signal is delivered to the piezoelectric actuator, pressure waves are generated in the fluid, and a stream of droplets is ejected out the end of the nozzle at a certain frequency (note that this would ideally be the same as the frequency of the optimal signal). To control the deposition of the droplet on the substrate surface, either the substrate or the entire printhead can be moved at the appropriate velocity [119]. This process could result in a controlled deposition of a uniform layer of nano- or picoliter-sized droplets across the surface of a substrate. Heating the substrate and printing more layers of a dilute radioactive metal salt of oxide solution might facilitate the fabrication of a thin, uniform radioactive target for neutron-induced charged particle reaction studies.

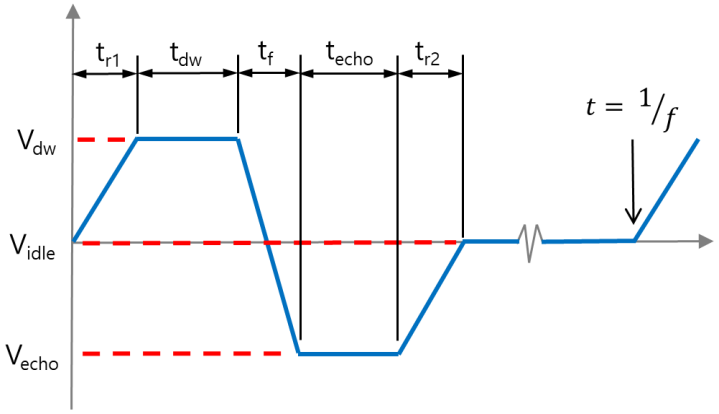

Figure 4.3: Schematic depicting the components of the electric signal that is sent to the pzieoelectric actuator where ***f*** is the frequency of the signal, t_{r1} and t_{r2} are rise times 1 and 2 respectively, t_{dw} is the dwell time, V_{dw} is the dwell voltage, t_f is the fall time, t_{echo} is the echo time, V_{echo} is the echo voltage, and V_{idle} is the idle voltage.

4.3 Electrodeposition

In literature, V has been shown to electrodeposit in low molarity sulfuric acid solutions [121–123]. However, this cannot be utilized with ^{48}V produced via aqueous isotope harvesting unless the ^{48}V is reconstituted in a low molarity sulfuric acid solution because the pure ^{48}V would be obtained in 1 M HNO_3 when following the optimal separation and purification method. Therefore, any possibility of electrodepositing ^{48}V onto a foil backing to produce a ^{48}V target for nuclear reaction studies would need to involve electrochemical reactions without the presence of sulfuric acid to prevent having to reconstitute the ^{48}V. Pretty et al. observed that vanadium in its vanadate form can be electrodeposited onto a reticulated vitreous carbon electrode in a pH 8 solution [124]. If this can be replicated with high yields and using a gold electrode, then it would be possible to produce a ^{48}V target via electrodeposition. Being able to directly deposit the V onto Au would be preferable because Au is an ideal target backing for studying neutron-induced charged particle reactions with the LENZ instrument (due to its contributions to the background in the obtained spectra is low) and it is commonly used as a neutron flux monitor during studies of nuclear reactions via the activation method [125]. However, electrochemical reactions can be sensitive to a variety of factors including the solution composition, the electrode material, and the finish of the electrode [126]. Thus, electrodeposition of V onto Au must be demonstrated prior to being able to conduct the electrodeposition via the simplified schematic shown in Figure 4.4. In this case, the vanadate in the solution can migrate close enough to the cathode to be reduced to a solid oxide or hydroxide species as long as the electrolyte concentration is high enough to cause the electrostatic potential forces to be negligible [126]. The vanadium oxide or hydroxide species would precipitate onto the surface of the Au electrode and post-treatment processes can be utilized to ensure the solid vanadium oxide or hydroxide adheres to the Au foil backing if necessary.

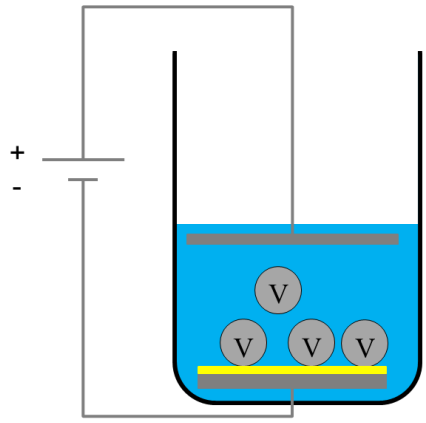

Figure 4.4: Schematic showing a simplified setup for electrodepositing V oxide or hydroxide complexes onto a gold foil. The anionic vanadate species reduces at the cathode when the applied potential is more negative than the reduction potential for the reaction, which results in V precipitating onto the cathode surface. By including enough of the electrolyte, NH_4NO_3, in the solution, the electricstatic potential gradient acting on the vanadate is negligible and allows for the V to react at the cathode surface.

4.3.1 Methods

To determine the possibility of using electrodeposition to fabricate a ^{48}V target for neutron-induced reaction studies, the studies conducted by Pretty et al. [124] should be replicated with a glassy carbon electrode. If the electrodeposition can be replicated, then attempts need to be made using Au foil. Ultimately, if vanadium can be electrodeposited onto a Au foil with high yields, then this could be a viable method for manufacturing a ^{48}V target for neutron-induced charged particle reaction studies.

4.3.1.1 Electrodeposition with Glassy Carbon Electrode

To perform these tests, a series of 1 ppm V solutions were prepared by evaporating the appropriate amounts of the concentrated 7700(200) ppm V stock solution, described in Section 2.3.1, to dryness in 20 mL vials. This was followed by reconstituting the V in a 0.1 M ammonium nitrate (NH_4NO_3, ACS grade, procured from MilliporeSigma, USA) aqueous solution that was adjusted to be a pH 8 solution with 2 M NH_4OH and 3 % v/v HNO_3 while

undergoing constant purging with N_2 gas. The total volume of the resulting solutions was 10 mL and the solutions were allowed to equilibrate for at least 72 hours to minimize the amount of polymeric species. After equilibration, a CH Instruments, Inc. 600 series potentiostat was used to perform anodic stripping voltammetry (ASV) with a 3 mm diameter disc glassy carbon electrode as the working electrode, a platinum counter electrode, and a Ag/AgCl reference electrode following the settings shown in Table 4.1. After performing ASV, the applied potential was left at +1.3 V for an additional 30 seconds to ensure the deposited V was completely stripped from the electrode surface. A blank solution was run before the sample set using the same settings in Table 4.1. Before each run, 250 µL of the sample was withdrawn. An additional 500 µL was withdrawn at the end of the deposition time. All aliquots were diluted to 5 mL and analyzed via ICP-OES to determine the V concentration in the aqueous phase.

Table 4.1: Settings used to collect anodic stripping voltammograms. The total deposition time was increased if longer depositions were being attempted. If an anodic stripping voltammogram was desired for a solution with high concentrations of V, such as 100 or 500 ppm, then the total deposition time was decreased to 60 seconds. With ~12 ppm V solutions, the total deposition time was set to 300 seconds. Also, any anodic stripping voltammograms obtained for depositions with Au foil had scan rates of 0.1 V/s.

Anodic Stripping Voltammetry Settings	
Initial Potential	-1.3 V
Final Potential	+1.3 V
Scan Rate	0.05 V/s
Sample Interval	0.001 V
Total Deposition Time	900 s
Quiet Time (no stirring)	30 s

4.3.1.2 Electrodeposition with Gold Foil

The same procedure described in the previous section was performed for attempts to electrodeposit V onto a Au foil with the following exceptions: the NH_4NO_3 was trace metals grade obtained from MilliporeSigma, USA, solutions contained ~12 ppm V produced using a 1000 ppm vanadium ICP standard solution also obtained from MilliporeSigma, USA, and the Au foil (a 6 µm

thick 99.9% pure light tight foil purchased from Goodfellow Corporation, USA) had a 1.13 cm^2 deposition area. Additionally, attempts were made to vary the deposition potential (to -0.9 V and -1.0 V), adjust the V concentration, measure the pH, and add a phosphate buffer solution (sodium phosphate dibasic and monobasic (Na_2HPO_4 and NaH_2PO_4 respectively, both trace metals basis and procured from MilliporeSigma, USA)) in place of the NH_4NO_3 electrolyte.

4.3.2 Results

4.3.2.1 Electrodeposition with Glassy Carbon Electrode

V was deposited from a 1 ppm V solution that originally contained 8.2(5) µg of V resulted in only 0.29(23) µg of V depositing onto a glassy carbon electrode with a deposition efficiency of 4(3)%. This appears to be lower than what Pretty et al. observed. However, the solutions made by Pretty et al. contained nanogram levels of metal ions and a reticulated vitreous carbon electrode is a porous material that probably has a larger surface than the glassy carbon disc electrode utilized in these experiments with microgram amounts of metal ions. Another possible reason for the poor deposition results could be the presence of considerable amounts of tetravalent V species, which were formed during the long equilibration time. Pretty et al. observed poor deposition when tetravalent V was the dominant species of vanadium [124]. However, this does not seem to be very probable, as 1 ppm Cr pH 8 solutions made under identical conditions as the 1 ppm V pH 8 solutions suggested the hexavalent Cr is not reduced to trivalent Cr (see Figure A.1 in APPENDIX). This result would also suggest the reduction of pentavalent V to tetravalent V, as Cr and V have similar aqueous chemistries in pH 8 solutions [72]. Although poor V deposition yields were obtained with a glassy carbon electrode, it is possible the deposition yield could be improved if the deposition area was increased.

4.3.2.2 Electrodeposition with Gold Foil

Electrodepositing V from an approximately 12 ppm V pH 8 solution onto a Au foil for a total deposition time of 5 minutes resulted in deposition at applied potentials of -1 and -0.9 V (see Table 4.2 on the next page). During the deposition at an applied potential of -1.0 V, intense H_2 evolution was observed. This H_2 generation decreased when the deposition potential was -0.9 V. Because of these observations and the deposition efficiencies at both applied potentials were within error of each other, -0.9 V was chosen to be the deposition potential. A typical anodic stripping voltammogram from these deposition attempts is shown in Figure 4.5 on the next page. From these tests, the peak potential, E_p, for the vanadium oxidation (and reduction) reaction was found to be -127 mV. Electrodepositing V at a deposition potential of -0.9 V from a more concentrated V solution (500 ppm) for longer periods of time, such as about 1 hour, resulted in the V concentration decreasing slightly within the initial 15 minutes (by about 1%), but afterwards, the concentration rises to approximately 100.7% of the initial solution concentration. The pH of this solution was found to have shifted from pH 8 to pH 6. Performing anodic stripping voltammetry with the 500 ppm V pH 6 solution revealed the absence of the -127 mV peak corresponding to the V oxidation reaction during the stripping of the Au foil. These results suggest that the inability to maintain the pH throughout the electrodeposition experiment led to the re-dissolving of the originally deposited V into the solution, along with any additional V being reduced by the Au foil not forming a solid oxide or hydroxide precipitate. This is not surprising because V has a very complex aqueous solution chemistry [72]. To prevent the pH from shifting, an attempt was made to utilize a buffer solution in place of the electrolyte.

Table 4.2: Results after attempts to electrodeposit V onto Au foil from an approximately 12 ppm V pH 8 solution with 0.1 NH_4NO_3 as the electrolyte. The total deposition time was 5 minutes.

Deposition Potential (V)	Initial V (µg)	Deposited V (µg)	Deposition Efficiency (%)
-0.9	59.7(6)	1.1(7)	1.9(11)
-1.0	59.5(6)	1.0(6)	1.7(11)

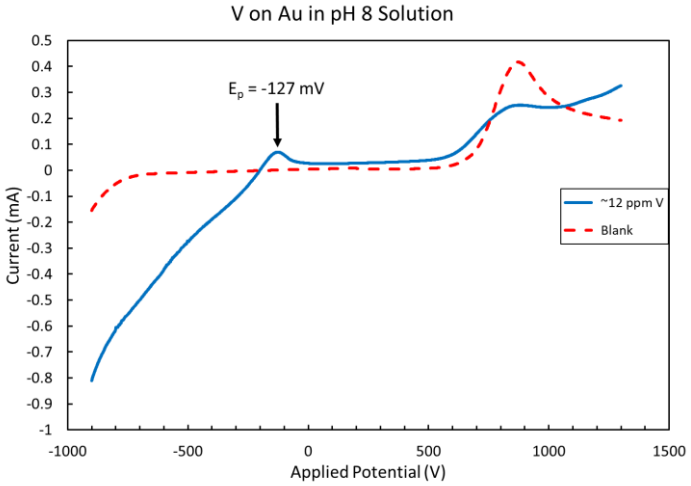

Figure 4.5: Anodic stripping voltammograms of an approximately 12 ppm V pH 8 solution and a blank with a Au foil as the cathode. Both solutions contained 0.1 M NH_4NO_3 as the electrolyte. The peak potential, E_p, for the V oxidation reaction is -127 mV.

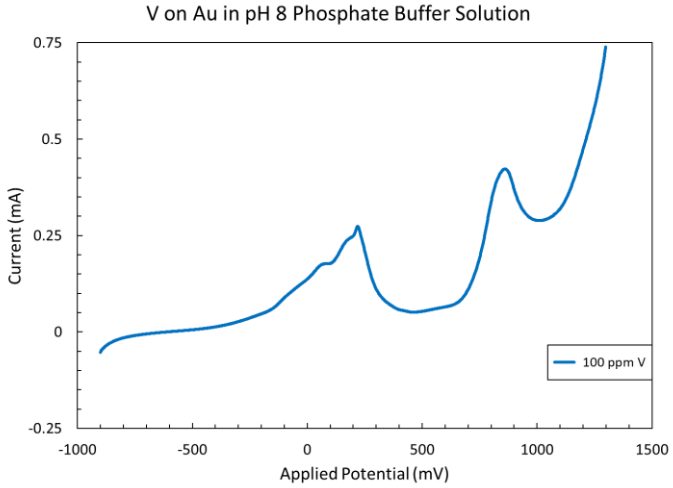

Figure 4.6: Anodic stripping voltammogram for a pH 8 solution containing 100 ppm V and stabilized with a 0.2 M phosphate buffer. Note that the peak potential for the V oxidation reaction observed in Figure 4.5 at -127 mV is absent.

Figure 4.6 shows the anodic stripping voltammogram that was obtained when a 0.2 M phosphate buffer replaced the NH_4NO_3 electrolyte in a 100 ppm V pH 8 solution. The V oxidation reaction at -127 mV appears to be absent in this plot. This suggests the V reacted with

the phosphate buffer and, just like in the previous experiments when the pH became more acidic, formed complexes that do not partake in electrochemical deposition reactions on the surface of the Au foil. This is additionally collaborated by the slow color change of the solution from yellow and clear (with the fresh solution) to slightly white and opaque (final state obtained between 0.5 and 3 days). Because V is also likely to interact with many of the other possible pH 8 buffer solution candidates and slowly adding a basic solution continuously during attempts to deposit V onto a Au foil is impractical (particularly due to the increasing solution size and the fact that this would need to occur within a hot cell with a radioactive sample to produce a ^{48}V target), no further investigations were conducted into attempting to electrodeposit V from a variation of these solutions and alternative methods were given more focus.

4.3.3 Alternative Electrodeposition Analog Target

One alternative method that is similar to electrodeposition is applying a V chemical conversion coating to an aluminum foil. A conversion coating is a coating deposited onto a solid metal due to chemical reactions that occur between the solid metal surface and other ions in the solution [127]. Aluminum has been used as a target backing or containment structure for some experiments examining nuclear reactions [11] and could be an adequate target backing for neutron-induced charged particle reaction studies with the LENZ instrument. There are numerous chemical reactions that can facilitate the formation of a conversion coating and a combination of these reactions is usually involved in the process. Some of these reactions include acid dissociation, pH-driven precipitation, oxidation, and reduction [127]. The formation of a V oxide layer on the Al surface of may initiate in part due to a redox reaction between the aqueous V species and the solid Al because the standard reduction potential for pentavalent V is more noble than the standard reduction potential for metallic Al [128]. For multilayer deposition after enough V has been

initially reduced, Guan and Buchheit suggested a proposed mechanism that involves a sol-gel process where hydrolyzed V undergoes an olation reaction and forms inorganic polymers interconnected by covalent or intermolecular bonding. These authors also observed V conversion coatings on Al being similar in morphology to conventional chromium conversion coatings on Al, which have been shown to exhibit uniform thickness during growth on Al surfaces [129,130]. This method was utilized in a related project conducted by another researcher within the Isotope Harvesting group, therefore the work undertaken to determine an optimized procedure for this method is outside the scope of this dissertation. However, applying the optimized procedure, which is based on a modified procedure of that developed by Sudagar et al., allowed samples of stable V targets to be manufactured. The results suggest the formation of a vanadium oxide layer that is most likely similar to the vanadium oxide or hydroxide precipitate formed during electrodeposition because the conversion coating solution was a pH 8 solution [131]. This means a sample stable V target manufactured via this method can be compared to microjet printed targets as an analog to an electrodeposited V target.

4.4 Microjet Printing

Microjet printing is a potential target production method that can theoretically fabricate any solid target for neutron reaction studies as long as the target nuclide of interest is soluble in a liquid, however this still needs to be examined. To manufacture radioactive targets, a microjet printer must fit inside of a hot cell. Commercial DoD devices typically need to be adapted for use a hot cell (i.e. parts need to be easily exchangeable and able to handle radioactive solutions), so a prototype compact microjet printer needs to be constructed to obtain a more accurate evaluation of this technique to fabricate radioactive targets for neutron reaction studies. After a prototype printer is constructed, the microjet printing technique can be evaluated by producing prototype

targets and comparing them to a sample analog electrodeposition target along with optimized microjet printed targets fabricated with a commercially available materials deposition platform.

4.4.1 Methods

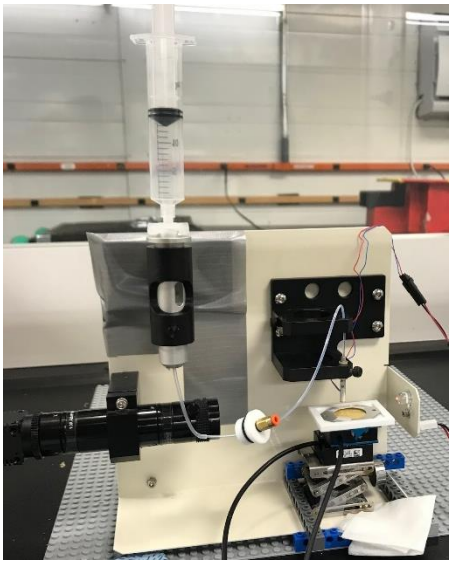

Figure 4.7: Prototype microjet printer.

The prototype printer assembled for producing prototype microjet printed targets is shown in Figure 4.7 and consists of a PH-47 printhead purchased from Microfab, USA and motorized stages acquired from Physik Instrumente, USA (U-521 PILine® Linear Stages). To produce a continuous stream of picoliter-sized droplets, the pressure of the air in the headspace of the fluid reservoir needs to be controlled and the optimal voltage signal needs to be sent to the annular piezoelectric element in the nozzle of the printhead. The fluid reservoir in the PH-47 printhead was replaced with a cartridge style fluid reservoir from a PH-41 printhead (Microfab) to allow for small solution volumes to be utilized and better control of the air pressure in the headspace of the fluid reservoir when using a disposable BD 10 mL. Nozzles with an 80 µm orifice (MJ-AT-01-80, procured from Microfab, USA) were installed in the printhead. This prototype printer did not have the capability to fabricate optimal stable targets. Optimized microjet printed targets were fabricated

with a commercially available materials deposition platform (CeraPrinter F-Serie materials deposition platform, acquired from CeraDrop, France).

4.4.1.1 Microjet Printing

The solutions that were printed are listed in Table 4.3 on the next page and comprised of a sodium chloride (NaCl, 99.999% trace metals basis, procured from MilliporeSigma, USA) solution to produce NaCl control targets and a V solution, which was made by dissolving ammonium metavanadate (NH_4VO_3, 99.999% trace metals basis, obtained from MilliporeSigma, USA) in a pH 9.5 solution (adjusted using NH_4OH (Optima grade, procured from Fisher Scientific, USA). The Au foils (all acquired from Goodfellow Corporation, USA as 99.9% pure light tight foils) that the solutions were printed on were 3 µm thick (for all V target samples), 4 µm thick (for NaCl control that underwent neutron-induced charged particle analysis), and 10 µm thick (for duplicate NaCl target). For controlled droplet deposition, both the drop generation process and substrate movement needed to be optimized. Table 4.4 on the next page shows the parameters for the optimized waveforms that were sent to the piezoelectric actuator for each solution. A CM-VSU-01 optics system procured from Microfab, USA was used to image the droplets and ImageJ was used to measure the droplet size. The motion stages were set to move at the optimal stage movement speed of 25 mm/s and droplets were deposited in a circular 2D cubic pattern. Each printed layer required the printhead to pass over the entire deposition area 4 times with a 30 second delay between each pass to ensure complete evaporation of the deposited droplets. With this setup, droplets were deposited 100 µm apart in each pass and the subsequent passes were offset 50 µm from the preceding ones so that each layer consisted of dried deposits spaced 50 µm apart from each other. After the sample targets were printed, they were coated with a 20 nm Au layer via physical vapor deposition to improve the adhesion of the metal salt or oxide film to the Au backing.

Table 4.3: Metal salt solutions used to produce microjet printed targets on Au foils with the prototype printer. The NH_4VO_3 solution was adjusted to pH 9 with 5 drops of 14.3 M NH_4OH.

Solution	Drop Volume (pL)	Sessile Drop Diameter (μm)	Notes
100 mg NaCl/g DI H_2O	26.5(4)	58.0(3)	
5 mg NH_4VO_3/g DI H_2O	28.9(4)	53.1(2)	pH 9.5 solution

Table 4.4: Parameter values for the electric signal sent to the piezoelectric actuator in the printhead for each solution printed. When using the CeraPrinter, the same parameter set was required to produce a continuous stream of droplets for both solutions.

Salt/Printer	f (Hz)	t_{r1} (μs)	t_{dw} (μs)	t_f (μs)	t_{echo} (μs)	t_{r2} (μs)	V_{dw} (V)	V_{echo} (V)	V_{idle} (V)
NaCl/Prototype	500	4	18	4	3	3	20	0	1
NH_4VO_3/Prototype	500	4	6	4	3	3	57	0	0
Both/CeraPrinter	500	4	6	4	3	3	57	0	0

4.4.1.2 Optimized Microjet Printing

To fabricate optimized microjet printed sample targets, a CeraPrinter F-Serie materials deposition platform was used to print the same NaCl and V solutions listed in Table 4.3. The same nozzles utilized to print the prototype target were inserted into the CeraPrinter and prior to printing the metal salt solutions. The diameters of the deposited metal salt solution droplets (a.k.a. sessile drop diameters) were measured using an internal camera in the printhead of the CeraPrinter and are also listed in Table 4.3. These diameters were used to ensure deposited droplets would not overlap during the printing process. To be able to more thoroughly compare these optimized targets with the prototype microjet printed targets, a 1-layer and a 10-layer NaCl sample target were also made with a deposited droplet spacing of 50 μm (i.e. the spacing used with the prototype microjet printer). During the printing process, the Au foils were always heated to 60 °C.

4.4.1.3 Target Film Imaging and Composition

A Keyence VK-X3100 laser microscope was used to examine the surfaces and the morphology of all sample targets. Optical imaging was performed to capture the 2D images with either a 2.5x or 10x magnification lens, while 3D images were obtained via the focus variation method and confocal laser scanning. The 3D images obtained via the focus variation method for the prototype and optimized microjet printed targets were analyzed with the Keyence Analysis

software to determine the surface coverage and thickness of the metal salt or oxide layers. The thickness measurements were performed by analyzing the obtained 3D images. For the sample targets prepared via the application of a V conversion coating on Al, slices of the 3D images obtained via confocal laser scanning were analyzed to determine the thickness of the V layer only because the V layer did not have many breaks or gaps that allowed for using the focus variation method. Compilations of 2D optical images of these sample targets were obtained with the 2.5x magnification lens and analyzed with ImageJ to determine the surface coverage of the V layer. Meanwhile, the atomic composition of the V films on the prototype microjet printed and V conversion coating targets were measured via X-ray photoelectron spectroscopy (XPS). The initial XPS measurements performed on the V conversion coating targets utilized a Perkin-Elmer Phi 5600 ESCA system with a magnesium K_α x-ray source at MSU. All other XPS measurements were performed at the Los Alamos National Laboratory (LANL).

4.4.1.4 Neutron-Induced Charged Particle Spectroscopy

Neutron-induced charged particle spectroscopy was performed to detect impurities in a V conversion coating target, a prototype microjet printed NaCl target, and a prototype microjet printed V target. The sample targets were mounted on a target ladder and placed in the LENZ instrument on the 15R neutron flight path in the WNR facility at LANSCE. The outgoing charged particles were detected with two annular S1-type DSSDs arranged to cover the particles ejected at angles spanning 40 to 60° relative to the beam axis. This detector setup was optimized to study $^{16}O(n,\alpha)$ reactions at the forward angles with a 65 μm DSSD and additional background reactions with a 1000 μm thick DSSD mounted at backward angles.

4.4.2 Results

4.4.2.1 Purity and Composition

The vanadium layers in the prototype microjet printed and chemical conversion coating targets were measured via XPS and their V-to-O atomic compositions were found to be 30:70 and 15:85 respectively. The V layer in the prototype microjet printed sample target appears to primarily consist of V_2O_5 because the V $2p_{3/2}$ peak was at 517 eV, which corresponds to the expected peak for V-O bonds in V_2O_5 [132]. V_2O_5 was expected to be the primary chemical form of the vanadium in this sample target because the ammonium ion has a low acid dissociation constant [128], which means most of those ions end up forming ammonia. Ammonia is a very volatile compound with a low Henry's law solubility constant in aqueous solutions [62]. Meanwhile, the conversion coating target was observed to have a combination of V_2O_5 and V_2O_4 because of the V $2p_{3/2}$ peak was broad and encompassed 516 eV and 517 eV (see Figure 4.8 on the next page), the V $2p_{3/2}$ peaks for V_2O_4 and V_2O_5 respectively [132]. After the conversion coating target was exposed to ambient air for one week, the XPS results suggest the V layer became primarily V_2O_5 because the V $2p_{3/2}$ peak was observed to be at 517 eV. The V was expected to be V_2O_4 because it had to reduce as part of a redox reaction with the Al near the surface of the Al foil. However, the V_2O_4 is expected to oxidize to V_2O_5 in the presence of ambient air because this has been observed before [133]. A Ca $2p_{3/2}$ peak also appears at 347 eV and a C 1s peak appears at 284.8 eV for the V layer on the conversion coating target, which suggests CaO (note that the C 1s peak would be at about 289 eV if the Ca was $CaCO_3$) is present as an impurity (see Figure A.2 in APPENDIX) [134]. This calcium impurity in the conversion coating target was unexpected, but numerous chemicals were used during the preparation and execution of applying the V conversion coating and it is possible that

one contained some calcium impurity. Furthermore, multiple O 1s peaks were observed in both sample targets. This suggests that water or some other impurity was probably present in the layers.

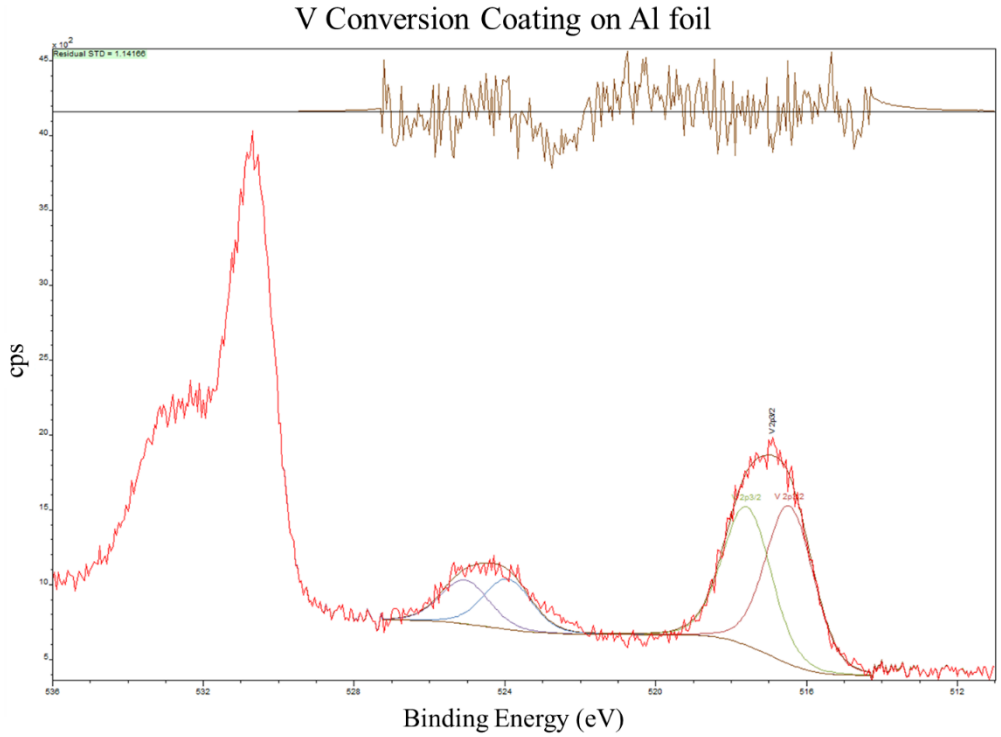

Figure 4.8: X-ray photoelectron spectroscopy results for a V conversion coating on Al target fabricated at MSU. This part of the spectrum has been enlarged and fitted to show the contributions of the V-O bonds in V_2O_4 and in V_2O_5 to the V $2p_{3/2}$ peak. The V $2p_{3/2}$ peak positions for V_2O_4 and V_2O_5 from the fit were 516.45 eV and 517.58 eV respectively.

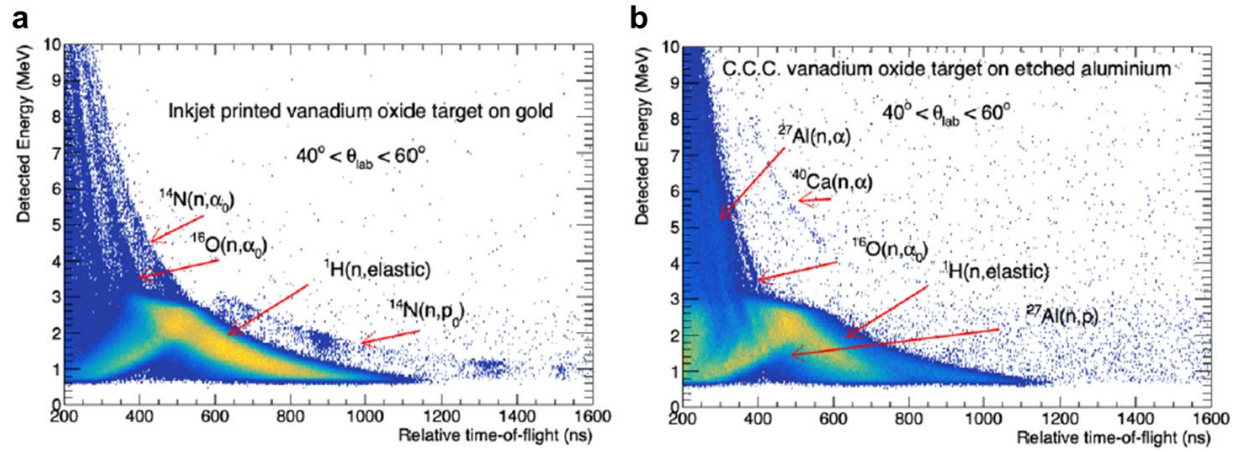

Figure 4.9: Neutron-induced charged particle spectroscopy results for (a) a microjet printed V target (see Figure 4.10b) and (b) a V conversion coating target (see Figure 4.10c). The correlation between the energy of the detected charged particle and the neutron time-of-flight provides a signature of the reaction Q value and is used to identify the reactions of interest.

Additional investigations were performed using the LENZ instrument at LANSCE to, in part, identify the impurities. Figure 4.9 on the previous page shows the results of the neutron-induced charged particle spectroscopy for one of the conversion coating targets and one of the prototype microjet printed V targets. Impurities were present in both targets, as indicated by the observation of the $^{14}\mathrm{N}(n,\alpha_0)$ and $^{40}\mathrm{Ca}(n,\alpha)$ reactions. The nitrogen impurity in the prototype microjet printed V target was expected, as the original V salt contained ammonium ions, while the Ca impurity in the conversion coating target validates the XPS results. Also, the $^{1}\mathrm{H}(n,el)$ reaction was observed in both targets, which is more evidence that water was likely present. The $^{1}\mathrm{H}(n,el)$ and $^{16}\mathrm{O}(n,\alpha_0)$ reactions do not always interfere with the reaction of interest when performing measurements on neutron-induced charged particle reactions; however, it would be beneficial to minimize the presence of water in these targets. Not all observed counts for the $^{1}\mathrm{H}(n,el)$ reaction in the plot for the prototype microjet printed V target are from water because some are from the suspected ammonium ion impurity. Another notable feature of the plots shown in Figure 4.9 is the size of the bands for the $^{16}\mathrm{O}(n,\alpha_0)$ reaction. The band appears to be broader for the prototype microjet printed V target than the band for the V conversion coating target. This result was expected because the prototype microjet printed V targets were found to be thicker than the conversion coating targets (11.7(27) μm vs. 5.3(18) μm). Overall, these findings highlight an advantage microjet printing can have over more traditional techniques such as electrodeposition or molecular plating in the case of impurities because additional chemicals, such as electrolytes, that could contain unknown impurities do not need to be added.

4.4.2.2 Surface Morphology and Uniformity

The prototype microjet printed and conversion coating sample targets are shown in 2D optical images in Figure 4.10, while 3D images of the microjet printed targets are shown in

Figure 4.11. Data on the surface coverage and average thicknesses of all sample targets are shown in Table 4.5 on the next page. The prototype microjet printed targets appear to be relatively uniform with somewhat poor surface coverage, as indicated by the data shown in Table 4.5 and the low variance in the metal salt or oxide film thicknesses in the 3D images in Figure 4.11. Meanwhile, the data on the V conversion coating targets in Table 4.5 and the uniform layer thickness implied from its smooth topography suggest these targets have excellent uniformity and good surface coverage.

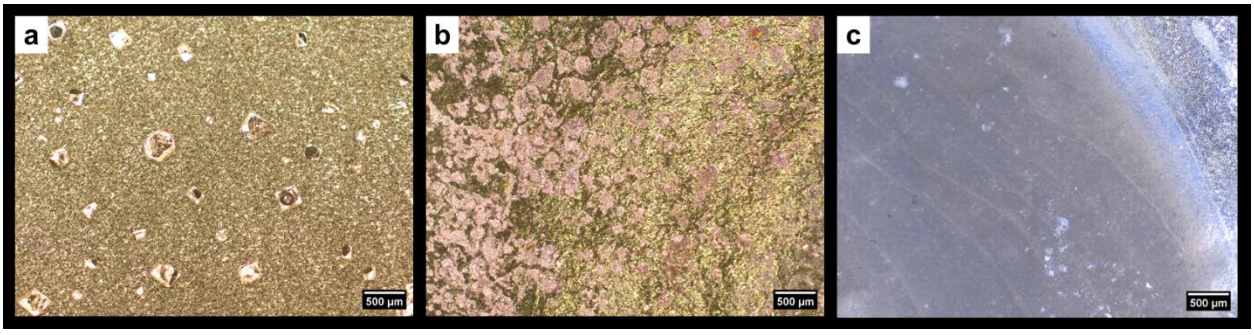

Figure 4.10: Optical 2D images of (a) NaCl and (b) V targets produced with the prototype microjet printer. Also shown in (c) is the edge of a V conversion coating target. The top righthand part of (c) is the Al backing, while the V layer is the brownish layer that covers most of the image. This brownish layer extends over most of the deposition area for the V conversion coating target.

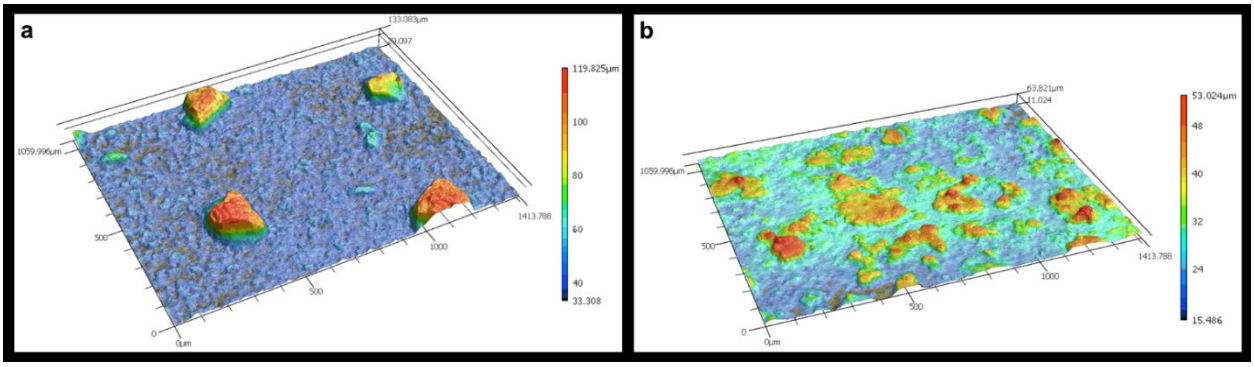

Figure 4.11: The focus variation method was used to obtain 3D images of (a) a region on the lefthand side of the NaCl target in Figure 4.10a and (b) a region near the top righthand corner of the V target in Figure 4.10b. The topgraphy of the V layer in the V conversion coating target was essentially smooth with no significant variation in height, so none of those 3D images are shown here.

Table 4.5: Average deposited metal salt or oxide layer surface coverage and thicknesses for all targets fabricated with the prototype microjet printer and by V conversion coating.

Target	Average Surface Coverage (%)	Average Thickness (µm)
Prototype Microjet Printed NaCl	13.3(3)	14(5)
Prototype Microjet Printed V	30.9(3)	11.7(27)
V Conversion Coating	79.8(4)	5.3(18)

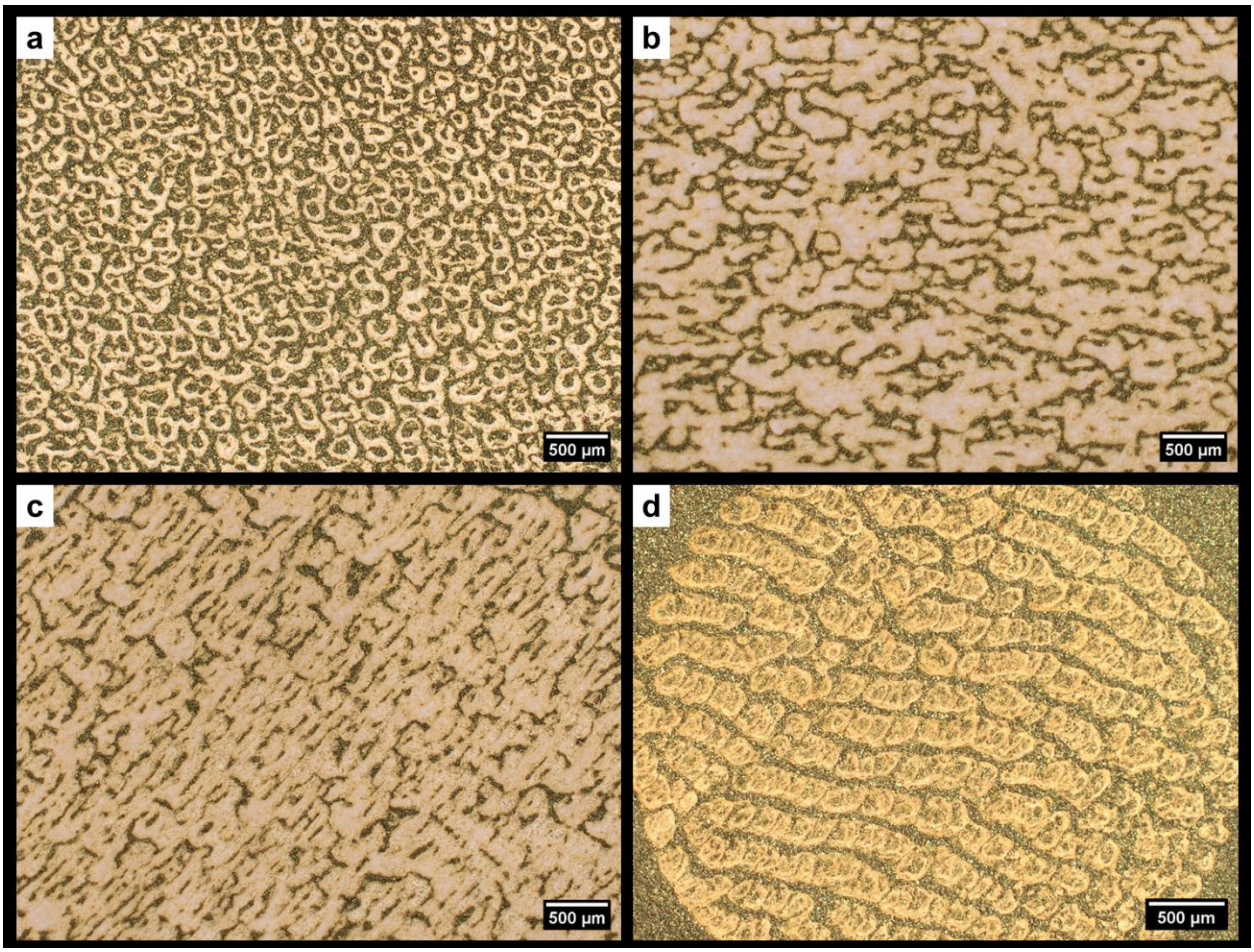

Figure 4.12: Optical 2D images of NaCl and V targets prepared with the CeraPrinter. Three were NaCl targets that were printed with various layers and droplet spacings: (a) one layer of droplets spaced 50 µm from each other (i.e. a direct comparison to the prototype microjet printed NaCl target in Figure 4.10a), (b) ten layers of droplets spaced 50 µm from each other, and (c) ten layers of droplets spaced 58.0 µm apart. The V target (d) had 167 layers of droplets spaced 53.1 µm apart.

Optical images of microjet printed targets prepared with the CeraPrinter are shown in Figure 4.12, 3D images are shown in Figure 4.13, and the surface coverages and metal salt or oxide layer thicknesses are listed in Table 4.6 on the next page. The CeraPrinter F-Serie materials deposition platform did not always produce more uniform targets than the prototype microjet

printer as the 1-layer NaCl microjet printed target shown in Figure 4.12a and Figure 4.13a is qualitatively less uniform than the prototype microjet printed sample target displayed in Figure 4.10a and Figure 4.11a. This observation appears to be true despite the NaCl target fabricated with the CeraPrinter being thinner and having a higher surface coverage than the NaCl target produced with the prototype microjet printer. The surface coverage and average thickness respectively increase and decrease when multiple layers were printed with the CeraPrinter. However, the uniformity was improved only if the droplets are deposited at an optimal distance from each other, as the 10-layer NaCl target created with deposited droplets spaced by their sessile drop diameter on Au (58.0 μm) was the only NaCl target that was qualitatively better than any of the other NaCl sample targets. This adjustment to the printing of the NaCl layer results in a lower areal density (or a thinner layer) and a qualitatively better uniformity. Overall, these observations suggest that the combination of optimal droplet deposition and heating of the target backing during the printing process improve the thickness, coverage, and uniformity of the deposited layer.

Table 4.6: Average metal salt or oxide layer surface coverage and thicknesses for samples printed with the CeraPrinter (CP) shown in Figure 4.12 and Figure 4.13 along with the results for the NaCl and V targets prepared with the prototype micojet printer originally displayed in Table 4.5.

Target	Average Surface Coverage (%)	Average Thickness (μm)
Prototype Microjet Printed NaCl	13.3(3)	14(5)
CP 1-Layer NaCl	41.1(14)	9(5)
CP 10-Layer NaCl with 50 μm drop spacing	96.8(23)	10(5)
CP 10-Layer NaCl with 58 μm drop spacing	76(8)	8.3(12)
Prototype Microjet Printed V	30.9(3)	11.7(27)
CP 167-Layer V	68.0(22)	8.1(19)

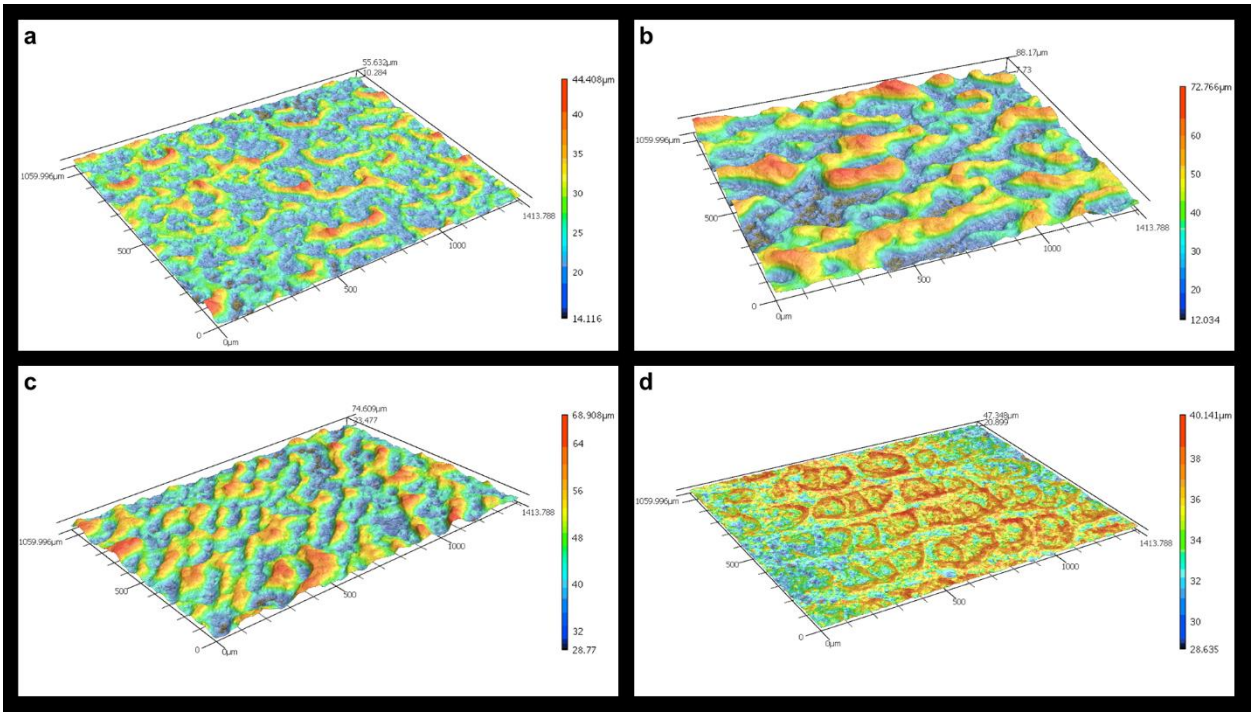

Figure 4.13: The focus variation method was used to assemble 3D images of 1.499 mm^2 areas of each target shown in Figure 4.12. The area imaged for the 1-layer NaCl target (a) is in the center of Figure 4.12a. For the 10-layer NaCl with a droplet spacing of 50 µm (b), the area is the bottom right corner next to the scale bar of Figure 4.12b. The imaged areas for both the 10-layer NaCl with a droplet spacing of 58.0 µm (c) and the V target (d) are in the centers of Figure 4.12c and Figure 4.12d respectively.

In light of these observations, a multilayer V microjet printed target was produced with the CeraPrinter and an optimal droplet spacing of 53.1 µm. This resulted in a V layer that was larger in surface coverage and thinner in thickness than the layer obtained with the prototype microjet printer, but with seemingly no improvement in the uniformity. The reason why no improvement was observed in the uniformity of the V layer is difficult to discern, as the morphology of this layer depends on the mechanism behind the evaporation of the deposited salt solution droplets. The evaporation process is typically affected by a combination of variables, which include physical and chemical properties of the liquid and gas phases [135], the salt concentration [136], and the type of metal salt [137]. An exhaustive investigation of these parameters is outside the scope of this dissertation. Regardless of the mechanism behind the evaporation of the deposited droplets,

the results from this study suggest improvements could be made to the prototype microjet printer that result in thinner and more uniform metal salt or oxide layers for neutron-induced charged particle reaction studies.

4.5 ^{48}V Target Production Method Comparison

Between the two main target production techniques studied, microjet printing appears to be the most promising method for fabricating a ^{48}V target for neutron-induced charged particle reaction studies in the future. The more conventional electrodeposition technique was not very effective at electrodepositing V from a pH 8 solution. The solution would become too acidic during the deposition and cause the deposited solid V precipitate to redissolve into the solution. This could potentially be addressed by continuously dripping a basic solution into the electrochemical cell throughout the duration of an attempt to electrodeposit V; however, this increases the complexity of a task that would eventually be performed in a hot cell and could result in the premature termination of the deposition attempt if the electrochemical cell can only contain small volumes of solutions. Furthermore, the analysis of the electrodeposition analog target demonstrates how reactions with an unexpected impurity from a chemical additive can be observed during measurements on direct neutron-induced reactions. If an electrodeposited V target could be made, it is certainly possible that an unexpected impurity could be observed in that target too due to the electrolyte that is required to enable the electrochemical reaction between the Au surface and V to occur in these solutions. It is preferable to avoid any unexpected impurities in the final target and the electrodeposition technique may not be able to meet this requirement, but microjet printing appears to do so because additional additives are not required.

The V targets manufactured via microjet printing with a small, rudimentary microjet printer (see Figure 4.7) had relatively good uniformity and no unexpected impurities, but with somewhat

poor surface coverage (30.9(3)%) and thickness (11.7(27) μm). However, the surface coverage and thickness can be improved with optimal droplet placement and heating of the Au backing during printing. This was demonstrated using a CeraPrinter F-Serie materials deposition platform as improvements were observed in the surface coverage (68.0(22)%) and thickness (8.1(19) μm) of the V layer, even with the deposition of more material than could be printed with the prototype printer. The adjustments that need to be made to the prototype printer will not considerably increase its size because small silicone heating elements could be added to the stage to enable heating of the Au backing during printing and adjustments to the droplet deposition pattern can be made in the software. Also, the prototype printer could be further improved by including a pneumatic controller to allow for automated control of the air pressure in the fluid reservoir headspace. This would enable more layers to be printed as the microjet printer could operate unattended, which is especially important for printing radioactive solutions. These adjustments are all feasible and together with the results from these preliminary experiments suggests that microjet printing has a high potential to be an excellent alternative target production technique in cases where the conventional electrodeposition or molecular plating techniques are not able to sufficiently produce targets for neutron-induced reaction studies. For the case of a ^{48}V target for neutron-induced charged particle reaction measurements, microjet printing is the superior technique to electrodeposition because V could not be electrodeposited with a high yield and guaranteed to have any unexpected impurities, whereas these concerns are not apparent with microjet printing.

4.6 Concluding Remarks

Two potential thin film target fabrication techniques were examined for their capability to manufacture a thin and uniform V target for neutron-induced reaction studies. The more

conventional method of the two, electrodeposition, was found not to be effective for producing a ^{48}V target because the pH of the radioactive solution would need to be continuously monitored and altered by slowly adding a basic solution throughout the duration of the deposition. The other method was a new method that allowed for the direct deposition of an aqueous solution containing V onto a Au foil target backing. By using a small, rudimentary microjet printer, sample V targets could be made that consisted of a primarily V_2O_5 layer with no unexpected impurities and somewhat poor surface coverage (30.9(3)%) and thickness (11.7(27) μm). With a large, commercially available materials deposition platform, these same sample targets could be fabricated with improved surface coverage (68.0(22)%) and thickness (8.1(19) μm) despite having more material deposited. Fortunately, the prototype microjet printer does not need to be substantially increased in size to accommodate the improvements that are required for it to print autonomously, heat the substrate, and print with optimal droplet spacing. Thus, there is enormous potential for this method to be adopted to a hot cell and utilized to print radioactive targets for neutron-induced reaction measurements. Overall, the results of these studies suggest that microjet printing is the best technique for manufacturing a ^{48}V target for direct measurements on neutron-induced charged particle reactions.

CHAPTER 5: CONCLUSIONS AND RECOMMENDATIONS

The work in this dissertation examined possible protocols for producing a highly pure ^{48}V target for neutron-induced reaction measurements. These protocols include both the production of the highly pure ^{48}V in mCi quantities and the fabrication of a thin and uniform ^{48}V target. Overall, the results of this work suggest that the best methods for performing these tasks are isotope harvesting for producing mCi levels of ^{48}V in high isotopic purity relative to ^{49}V ($>10^4$ atoms of ^{48}V/atom of ^{49}V) and microjet printing for manufacturing a thin and uniform ^{48}V target for neutron-induced reaction studies. However, conducting these experiments also resulted in the identification of future pathways to investigate to either improve these protocols or allow for the fabrication a ^{48}V target for neutron reaction studies, which will be described henceforth.

The first step in the isotope harvesting process is to extract the desired radionuclides out of the aqueous beam dump. In this case, ^{48}Cr is the desired radionuclide because harvesting and purifying the ^{48}Cr would allow for the set-up of a $^{48}Cr/^{48}V$ generator and the generation of ^{48}V in high isotopic purity. Previous studies examining isotope harvesting for various radionuclides utilized packed ion exchange resin columns to extract the desired radionuclides. However, the glass wool used to hold the ion exchange resin in place may not always be able to sustain the high backpressure these columns will experience. Thus, the flow rate needs to be moderated, which lowers the accumulation rate for the radionuclide of interest. Novel 3D-printed polypropylene resin cages were fabricated to address this issue and were proven to be just as effective as packed ion exchange columns without the risk of introducing resin to the beam dump loop. Also, these cages allow for the possibility of performing batch elutions with the resins, which is not easy to conduct with packed columns. In these experiments, 1.5 g of anion exchange resin in a resin cage was able

to extract Cr at 27(3) µg/min while 1.5 g of anion exchange resin in a packed column could extract Cr at 26(2) µg/min.

One downside of using such a small amount of resin in parallel with a line containing two 50-gallon ion exchange resin drums is the final yield or daily production rate for the radionuclide of interest is significantly suppressed. For example, including a single 1.5 g cation exchange resin cage followed by a single 1.5 g anion exchange resin cage would only allow for ^{48}V of high isotopic purity to have a daily production rate of 350 µCi/day because only 0.33% of the ^{48}Cr that passes through the clean-up loop could be harvested with the 1.5 g anion exchange resin cage. There are a few possible solutions that could increase this amount. One is to utilize more parallel lines containing ion exchange resin cages. This would increase the production rate and can be quite significant (e.g. adding 25 lines containing a 1.5 g cation exchange resin cage in series with a 1.5 g anion exchange resin cage would increase the ^{48}V (with $>10^4$ ^{48}V/^{49}V atomic ratio) production rate from 350 µCi/day to 8.9 mCi/day). Another possible solution is to prevent any of the clean-up loop solution from passing through the 50-gallon ion exchange resin drums. This would allow radionuclides to accumulate in the FRIB beam dump loop over the duration of the attempt to harvest radionuclides of interest and also increase the production rate into the mCi/day level (e.g. for a single 1.5 g cation exchange resin cage in series with a 1.5 g anion exchange resin cage, the daily production rate for ^{48}V (with $>10^4$ ^{48}V/^{49}V ratio) would increase from 350 µCi/day to 2.1 mCi/day). However, an improved accumulation rate would be desired to minimize the time that is spent attempting to harvest radionuclides with the inserted ion exchange resin cage and maximize the yield of short-lived radionuclides that have less than about 24 hour half-lives, such as ^{48}Cr. A third possible solution to improve the low production rate issue is to examine other designs for the ion exchange resin cage or column. This could involve simply increasing the size

of the resin cage to be able to insert more resin, but certainly other types of equipment, such as a rotating packed bed reactor containing ion exchange resin, could be examined as well. The optimal solution may even involve a combination of the solutions described above. Regardless, the limited production rate due to the low extraction efficiencies of using small amounts of resin in parallel with a high throughput line containing two 50-gallon ion exchange resin drums needs to be addressed in the future to allow for isotope harvesting to reach its full potential.

The second step in the process for fabricating a pure ^{48}V target for neutron-induced reaction studies is to produce the ^{48}V in high isotopic purity with respect to ^{49}V (>10^4 atoms of ^{48}V/atom of ^{49}V). The isotope harvesting method of setting up a ^{48}Cr/^{48}V generator to generate pure ^{48}V was compared with a more traditional isotope production method. The traditional technique involved irradiating ^{nat}Sc foil with 24.3 MeV α particles and the measured atomic ^{48}V/^{49}V ratio was found to be >10^3. This would only allow total cross-section measurements to be made with a precision of 100 barns when using the activation method instead of the desired 10 barns. The results from studies investigating the production of ^{48}V via isotope harvesting suggest that ^{48}V can be produced in mCi quantities and high enough isotopic purity (up to >10^8 atoms of ^{48}V/atom of ^{49}V) that meets or even exceeds these purity requirements. However, the performance of a proof-of-concept study of this production technique at FRIB is foreseen to verify whether ^{48}V can be produced with these predicted purity levels. Regardless, the results from the studies performed in this dissertation suggest that isotope harvesting at FRIB is the best isotope production method for producing mCi levels of ^{48}V in high enough isotopic purity relative to ^{49}V to attain a down to 1 millibarn resolution on the total neutron capture cross-section measured via the activation method.

The last step at this point would involve manufacturing a ^{48}V target. A target for the activation method to measure the ^{48}V(n, γ)^{49}V total cross-section only requires mCi quantities of

^{48}V with a high enough ^{48}V/^{49}V atomic ratio (>10^4 atoms of ^{48}V/atom of ^{49}V). By evaporating the pure ^{48}V solution of 1 M HNO_3 to dryness in a quartz ampule and flame-sealing it shut would produce an adequate target. However, to be able to measure the cross-sections for the ^{48}V(n, p)^{48}Ti reaction, the outgoing protons need to be detected as the reactions occur. The evaporated salt or oxide in a quartz ampule would not suffice for studies on these reactions because the outgoing protons would be stopped by the walls of the quartz tube. To study these reactions, the ^{48}V target must be thin with good uniformity. Two target production techniques were evaluated for their capability of producing a thin, uniform ^{48}V target for direct measurements of neutron-induced charged particle reactions with the LENZ instrument at LANL. One of these techniques involved electrodepositing V onto a Au foil. Initial attempts successfully electrodeposited V onto a Au foil; however, the solution becomes more acidic the longer the potential is applied and the precipitated V species on the surface of the Au foil redissolves into the solution. The other target production method under study was microjet printing and showed more favorable results as a V layer could be fabricated on a Au foil. Microjet printing involves directly depositing an aqueous solution containing V onto a Au foil target backing. Printed sample V targets manufactured using a small, preliminary microjet printer were found to primarily consist of a V_2O_5 layer with no unexpected impurities. However, the surface coverage (30.9(3)%) and thickness (11.7(27) μm) require further improvements. Additional results with a commercially available materials deposition platform suggest that even better surface coverage (68.0(22)%) and thickness (8.1(19) μm) can be obtained with the deposition of more material if the prototype microjet printer is enhanced to be able to print autonomously, heat the substrate, and print with optimal droplet spacing. Future work should focus on incorporating the required changes to the microjet printer and further validating the target production technique. One test that could be performed after upgrading the prototype microjet

printer would be to print a solution containing enriched ^{50}V, which is an essentially stable nuclide [138], and analyze the resulting target via optical microscopy and neutron-induced charged particle spectroscopy. Outgoing protons from the ^{50}V(n, p)^{50}Ti reaction would not be obscured by the background contribution of the Au foil because the reaction has a higher Q value (2.99) than the Q value for the ^{16}O(n, α)^{13}C reaction (-2.21). Conducting this experiment would help identify any additional shortcomings that need to be addressed prior to attempting to fabricate a ^{48}V target and would validate the ability of microjet printing to fabricate thin and uniform radioactive targets for direct measurements of neutron-induced charged particle reactions. Overall, the result from the work in this dissertation is a recommended thin ^{48}V target manufacturing protocol covering all the steps from the initial extraction of ^{48}Cr from the aqueous beam dump to the separations and timing required to set up a ^{48}Cr/^{48}V generator and produce mCi quantities of ^{48}V in high isotopic purity relative to ^{49}V (>10^4 atoms of ^{48}V/atom of ^{49}V), and finally to the fabrication of a thin and uniform ^{48}V target for neutron-induced reaction studies.

REFERENCES

[1] G.L. Bennett, E.A. Skrabek, Power performance of US space radioisotope thermoelectric generators, in: Fifteenth International Conference on Thermoelectrics. Proceedings ICT '96, 1996: pp. 357–372. https://doi.org/10.1109/ICT.1996.553506.

[2] D.E. Walling, Q. He, W. Blake, Use of ^{7}Be and ^{137}Cs measurements to document short- and medium-term rates of water-induced soil erosion on agricultural land, Water Resour Res. 35 (1999) 3865–3874. https://doi.org/10.1029/1999WR900242.

[3] V. Pichler, N. Berroterán-Infante, C. Philippe, C. Vraka, E.-M. Klebermass, T. Balber, S. Pfaff, L. Nics, M. Mitterhauser, W. Wadsak, An Overview of PET Radiochemistry, Part 1: The Covalent Labels ^{18}F, ^{11}C, and ^{13}N, Journal of Nuclear Medicine. 59 (2018) 1350. https://doi.org/10.2967/jnumed.117.190793.

[4] P.H. Liem, H.N. Tran, T.M. Sembiring, Design optimization of a new homogeneous reactor for medical radioisotope Mo-99/Tc-99m production, Progress in Nuclear Energy. 82 (2015) 191–196. https://doi.org/10.1016/j.pnucene.2014.07.040.

[5] F. Rösch, Past, present and future of ^{68}Ge/^{68}Ga generators, Applied Radiation and Isotopes. 76 (2013) 24–30. https://doi.org/10.1016/j.apradiso.2012.10.012.

[6] E. Grady, Nuts and Bolts of ^{223}Ra-Dichloride Therapy, J Nucl Med Technol. 50 (2022) 215. https://doi.org/10.2967/jnmt.122.263812.

[7] E.E. Parent, B. Savir-Baruch, I.W. Gayed, F. Almaguel, B.B. Chin, A.R. Pantel, E. Armstrong, A. Morley, R.C. Ippisch, R.R. Flavell, ^{177}Lu-PSMA Therapy, J Nucl Med Technol. 50 (2022) 205. https://doi.org/10.2967/jnmt.122.263814.

[8] R.J. Robbins, M.J. Schlumberger, The Evolving Role of ^{131}I for the Treatment of Differentiated Thyroid Carcinoma, Journal of Nuclear Medicine. 46 (2005) 28S. http://jnm.snmjournals.org/content/46/1_suppl/28S.abstract.

[9] J. Chen, Nuclear Data Sheets for A=48, Nuclear Data Sheets. 179 (2022) 1–382. https://doi.org/10.1016/j.nds.2021.12.001.

[10] J.A. Shusterman, N.D. Scielzo, K.J. Thomas, E.B. Norman, S.E. Lapi, C.S. Loveless, N.J. Peters, J.D. Robertson, D.A. Shaughnessy, A.P. Tonchev, The surprisingly large neutron capture cross-section of ^{88}Zr, Nature. 565 (2019) 328–330. https://doi.org/10.1038/s41586-018-0838-z.

[11] P. Schillebeeckx, A. Borella, J.C. Drohe, R. Eykens, S. Kopecky, C. Massimi, L.C. Mihailescu, A. Moens, M. Moxon, R. Wynants, Target requirements for neutron-induced cross-section measurements in the resonance region, Nucl Instrum Methods Phys Res A. 613 (2010) 378–385. https://doi.org/10.1016/j.nima.2009.09.080.

[12] Z.Y. Bao, H. Beer, F. Käppeler, F. Voss, K. Wisshak, T. Rauscher, Neutron Cross Sections for Nucleosynthesis Studies, At Data Nucl Data Tables. 76 (2000) 70–154. https://doi.org/10.1006/adnd.2000.0838.

[13] V.H. Reis, R.J. Hanrahan, W.K. Levedahl, The Big Science of stockpile stewardship, Phys Today. 69 (2016) 46–53. https://doi.org/10.1063/PT.3.3268.

[14] M. Stoyer, NSAC Whitepaper on Applications and Nuclear Data, Lawrence Livermore National Laboratory, Livermore, CA (United States), 2014. https://doi.org/10.2172/1179413.

[15] L. Ahle, M. Hausmann, R. Reifarth, K. Roberts, M. Roeben, B. Rusnak, D. Vieira, Realizing the Opportunities of Neutron Cross-Section Measurements at RIA, AIP Conf Proc. 769 (2005) 796–799. https://doi.org/10.1063/1.1945127.

[16] G. Tagliente, K. Fujii, P.M. Milazzo, C. Moreau, G. Aerts, U. Abbondanno, H. Álvarez, F. Alvarez-Velarde, S. Andriamonje, J. Andrzejewski, P. Assimakopoulos, L. Audouin, G. Badurek, P. Baumann, F. Bečvář, E. Berthoumieux, S. Bisterzo, F. Calviño, M. Calviani, D. Cano-Ott, R. Capote, C. Carrapiço, P. Cennini, V. Chepel, E. Chiaveri, N. Colonna, G. Cortes, A. Couture, J. Cox, M. Dahlfors, S. David, I. Dillman, C. Domingo-Pardo, W. Dridi, I. Duran, C. Eleftheriadis, M. Embid-Segura, L. Ferrant, A. Ferrari, R. Ferreira-Marques, W. Furman, R. Gallino, I. Goncalves, E. Gonzalez-Romero, F. Gramegna, C. Guerrero, F. Gunsing, B. Haas, R. Haight, M. Heil, A. Herrera-Martinez, M. Igashira, E. Jericha, F. Käppeler, Y. Kadi, D. Karadimos, D. Karamanis, M. Kerveno, P. Koehler, E. Kossionides, M. Krtička, C. Lamboudis, H. Leeb, A. Lindote, I. Lopes, M. Lozano, S. Lukic, J. Marganiec, S. Marrone, T. Martínez, C. Massimi, P. Mastinu, A. Mengoni, M. Mosconi, F. Neves, H. Oberhummer, S. O'Brien, J. Pancin, C. Papachristodoulou, C. Papadopoulos, C. Paradela, N. Patronis, A. Pavlik, P. Pavlopoulos, L. Perrot, M.T. Pigni, R. Plag, A. Plompen, A. Plukis, A. Poch, J. Praena, C. Pretel, J. Quesada, T. Rauscher, R. Reifarth, C. Rubbia, G. Rudolf, P. Rullhusen, J. Salgado, C. Santos, L. Sarchiapone, I. Savvidis, C. Stephan, J.L. Tain, L. Tassan-Got, L. Tavora, R. Terlizzi, G. Vannini, P. Vaz, A. Ventura, D. Villamarin, M.C. Vincente, V. Vlachoudis, R. Vlastou, F. Voss, S. Walter, H. Wendler, M. Wiescher, K. Wisshak, Neutron capture cross section of ^{90}Zr: Bottleneck in the *s*-process reaction flow, Phys Rev C. 77 (2008) 35802. https://doi.org/10.1103/PhysRevC.77.035802.

[17] T.W. Burrows, Nuclear Data Sheets for A = 49, Nuclear Data Sheets. 109 (2008) 1879–2032. https://doi.org/10.1016/j.nds.2008.07.001.

[18] K. Kelley, R.D. Hoffman, F.S. Dietrich, R. Bauer, M. Mustafa, N. p., Neutron and Charged-Particle Induced Cross Sections for Radiochemistry for Isotopes of Scandium, Titanium, Vanadium, Chromium, Manganese, and Iron, Lawrence Livermore National Laboratory, United States, 2005. https://doi.org/10.2172/15016178.

[19] G.F. Knoll, Radiation detection and measurement, John Wiley & Sons, 2010.

[20] J.A. Shusterman, N.D. Scielzo, E.P. Abel, H.K. Clause, N.D. Dronchi, W.D. Frey, N. Gharibyan, J.A. Hart, C.S. Loveless, S.R. McGuinness, L.T. Sutherlin, K.J. Thomas, S.E. Lapi, J.D. Robertson, M.A. Stoyer, E.B. Norman, G.F. Peaslee, G.W. Severin, D.A. Shaughnessy, Aqueous harvesting of ^{88}Zr at a radioactive-ion-beam facility for cross-section measurements, Phys. Rev. C. 103 (2021) 24614. https://doi.org/10.1103/PhysRevC.103.024614.

[21] W.D. Loveland, D.J. Morrissey, G.T. Seaborg, Modern Nuclear Chemistry, 1st ed., John Wiley & Sons, Inc., Hoboken, New Jersey, 2006.

[22] A.J.M. Plompen, O. Cabellos, C. De Saint Jean, M. Fleming, A. Algora, M. Angelone, P. Archier, E. Bauge, O. Bersillon, A. Blokhin, F. Cantargi, A. Chebboubi, C. Diez, H. Duarte, E. Dupont, J. Dyrda, B. Erasmus, L. Fiorito, U. Fischer, D. Flammini, D. Foligno, M.R. Gilbert, J.R. Granada, W. Haeck, F.-J. Hambsch, P. Helgesson, S. Hilaire, I. Hill, M. Hursin, R. Ichou, R. Jacqmin, B. Jansky, C. Jouanne, M.A. Kellett, D.H. Kim, H.I. Kim, I. Kodeli, A.J. Koning, A.Yu. Konobeyev, S. Kopecky, B. Kos, A. Krása, L.C. Leal, N. Leclaire, P. Leconte, Y.O. Lee, H. Leeb, O. Litaize, M. Majerle, J.I. Márquez Damián, F. Michel-Sendis, R.W. Mills, B. Morillon, G. Noguère, M. Pecchia, S. Pelloni, P. Pereslavtsev, R.J. Perry, D. Rochman, A. Röhrmoser, P. Romain, P. Romojaro, D. Roubtsov, P. Sauvan, P. Schillebeeckx, K.H. Schmidt, O. Serot, S. Simakov, I. Sirakov, H. Sjöstrand, A. Stankovskiy, J.C. Sublet, P. Tamagno, A. Trkov, S. van der Marck, F. Álvarez-Velarde, R. Villari, T.C. Ware, K. Yokoyama, G. Žerovnik, The joint evaluated fission and fusion nuclear data library, JEFF-3.3, The European Physical Journal A. 56 (2020) 181. https://doi.org/10.1140/epja/s10050-020-00141-9.

[23] B.A. Broder, M.P. Bhuiyan, R. Freifelder, H.J. Zhang, A. Kucharski, M.W. Makinen, D.A. Rotsch, C.-T. Chen, Preliminary investigation of ^{48}V-labeled $VO(acac)_2$ for cancer imaging: An initial proof-of-concept study, Applied Radiation and Isotopes. 186 (2022) 110270. https://doi.org/10.1016/j.apradiso.2022.110270.

[24] C.S. Loveless, J.R. Blanco, G.L. Diehl, R.T. Elbahrawi, T.S. Carzaniga, S. Braccini, S.E. Lapi, Cyclotron Production and Separation of Scandium Radionuclides from Natural Titanium Metal and Titanium Dioxide Targets, Journal of Nuclear Medicine. 62 (2021) 131–136. https://doi.org/10.2967/jnumed.120.242941.

[25] S.K. Zeisler, T.J. Ruth, Preparation of [^{48}V]-VO^{2+} for biomedical studies, J Radioanal Nucl Chem. 200 (1995) 283–290. https://doi.org/10.1007/BF02163782.

[26] H.I. West Jr., R.G. Lanier, M.G. Mustafa, R.M. Nuckolls, R.J. Nagle, H. O`Brien, J. Frehaut, A. Adam, C. Philis, Some light-ion excitation-function measurements on titanium, yttrium, and europium, and associated results, Livermore, CA, 1993. https://doi.org/10.2172/10142277.

[27] M. Mamtimin, F. Harmon, V.N. Starovoitova, Sc-47 production from titanium targets using electron linacs, Applied Radiation and Isotopes. 102 (2015) 1–4. https://doi.org/10.1016/J.APRADISO.2015.04.012.

[28] C.H. Johnson, C.C. Trail, A. Galonsky, Thresholds for (p, n) Reactions on 26 Intermediate-Weight Nuclei, Physical Review. 136 (1964) B1719–B1729. https://doi.org/10.1103/PhysRev.136.B1719.

[29] A.J. Koning, D. Rochman, J.-Ch. Sublet, N. Dzysiuk, M. Fleming, S. van der Marck, TENDL: Complete Nuclear Data Library for Innovative Nuclear Science and Technology, Nuclear Data Sheets. 155 (2019) 1–55. https://doi.org/10.1016/j.nds.2019.01.002.

[30] C.H. Johnson, A. Galonsky, J.P. Ulrich, Proton Strength Functions from (p, n) Cross Sections, Physical Review. 109 (1958) 1243–1254. https://doi.org/10.1103/PhysRev.109.1243.

[31] M. Al-abyad, H.E. Hassan, A.H.M. Solieman, F. Ditrói, Z.A. Saleh, Deuteron and α-particle-induced nuclear reactions on ^{45}Sc: activation cross section measurement and thick target yield evaluation, Indian Journal of Physics. (2023). https://doi.org/10.1007/s12648-022-02574-y.

[32] V.N. Levkovskij, Activation cross section nuclides of average masses (A= 40–100) by protons and alpha-particles with average energies (E= 10–50 MeV), Moscow, Russia. (1991).

[33] V.Y. Hansper, C.I.W. Tingwell, S.G. Tims, A.F. Scott, D.G. Sargood, The ^{45}Sc(α, p)^{48}Ti and ^{45}Sc(α, n)^{48}V cross sections, Nucl Phys A. 504 (1989) 605–620. https://doi.org/10.1016/0375-9474(89)90560-5.

[34] P.A. Beeley, J. Aaronson, K. Kokkas, J.J. Hogan, ^{45}Sc(α,αn)^{44}Sc^{m+g}: a monitor reaction for alpha particle induced reactions, Can J Chem. 61 (1983) 641–645. https://doi.org/10.1139/v83-117.

[35] A.E. Vlieks, J.F. Morgan, S.L. Blatt, Total cross sections for some (α, n) and (α, p) reactions in medium-weight nuclei, Nucl Phys A. 224 (1974) 492–502. https://doi.org/10.1016/0375-9474(74)90551-X.

[36] K.L. Chen, J.M. Miller, Comparison Between Reactions of Alpha Particles With Scandium-45 and Deuterons with Titanium-47, Physical Review. 134 (1964) B1269–B1280. https://doi.org/10.1103/PhysRev.134.B1269.

[37] R. Weinreich, H.J. Probst, S.M. Qaim, Production of chromium-48 for applications in life sciences, Int J Appl Radiat Isot. 31 (1980) 223–232. https://doi.org/10.1016/0020-708X(80)90112-X.

[38] J. Wang, X. Huang, Nuclear Data Sheets for A=51, Nuclear Data Sheets. 144 (2017) 1–296. https://doi.org/10.1016/j.nds.2017.08.002.

[39] H. Junde, Nuclear Data Sheets for A = 55, Nuclear Data Sheets. 109 (2008) 787–942. https://doi.org/10.1016/j.nds.2008.03.001.

[40] H. Junde, H. Su, Y. Dong, Nuclear Data Sheets for A = 56, Nuclear Data Sheets. 112 (2011) 1513–1645. https://doi.org/10.1016/j.nds.2011.04.004.

[41] E.P. Abel, K. Domnanich, H.K. Clause, C. Kalman, W. Walker, J.A. Shusterman, J. Greene, M. Gott, G.W. Severin, Production, Collection, and Purification of ^{47}Ca for the Generation of ^{47}Sc through Isotope Harvesting at the National Superconducting Cyclotron Laboratory, ACS Omega. 5 (2020) 27864–27872. https://doi.org/10.1021/acsomega.0c03020.

[42] E.P. Abel, M. Avilov, V. Ayres, E. Birnbaum, G. Bollen, G. Bonito, T. Bredeweg, H. Clause, A. Couture, J. DeVore, M. Dietrich, P. Ellison, J. Engle, R. Ferrieri, J. Fitzsimmons, M. Friedman, D. Georgobiani, S. Graves, J. Greene, S. Lapi, C.S. Loveless, T. Mastren, C. Martinez-Gomez, S. McGuinness, W. Mittig, D. Morrissey, G. Peaslee, F. Pellemoine, J.D. Robertson, N. Scielzo, M. Scott, G. Severin, D. Shaughnessy, J. Shusterman, J. Singh, M. Stoyer, L. Sutherlin, A. Visser, J. Wilkinson, Isotope harvesting at FRIB: additional opportunities for scientific discovery, Journal of Physics G: Nuclear and Particle Physics. 46 (2019) 100501. https://doi.org/10.1088/1361-6471/ab26cc.

[43] J.D. Robertson, Preparing for Harvesting Radioisotopes from FRIB, University of Missouri, United States, 2018. https://doi.org/10.2172/1435725.

[44] T. Mastren, A. Pen, G.F. Peaslee, N. Wozniak, S. Loveless, S. Essenmacher, L.G. Sobotka, D.J. Morrissey, S.E. Lapi, Feasibility of Isotope Harvesting at a Projectile Fragmentation Facility: ^{67}Cu, Sci Rep. 4 (2014) 6706. https://doi.org/10.1038/srep06706.

[45] A.B. Balantekin, J. Carlson, D.J. Dean, G.M. Fuller, R.J. Furnstahl, M. Hjorth-Jensen, R.V.F. Janssens, B.-A. Li, W. Nazarewicz, F.M. Nunes, W.E. Ormand, S. Reddy, B.M. Sherrill, Nuclear theory and science of the facility for rare isotope beams, Mod Phys Lett A. 29 (2014) 1430010. https://doi.org/10.1142/s0217732314300109.

[46] M. Hausmann, A.M. Aaron, A.M. Amthor, M. Avilov, L. Bandura, R. Bennett, G. Bollen, T. Borden, T.W. Burgess, S.S. Chouhan, V.B. Graves, W. Mittig, D.J. Morrissey, F. Pellemoine, M. Portillo, R.M. Ronningen, M. Schein, B.M. Sherrill, A. Zeller, Design of the Advanced Rare Isotope Separator ARIS at FRIB, Nucl Instrum Methods Phys Res B. 317 (2013) 349–353. https://doi.org/10.1016/j.nimb.2013.06.042.

[47] K.A. Domnanich, C.K. Vyas, E.P. Abel, C. Kalman, W. Walker, G.W. Severin, Harvesting ^{62}Zn from an aqueous cocktail at the NSCL, New Journal of Chemistry. 44 (2020) 20861–20870. https://doi.org/10.1039/D0NJ04411C.

[48] K.A. Domnanich, E.P. Abel, H.K. Clause, C. Kalman, W. Walker, G.W. Severin, An isotope harvesting beam blocker for the National Superconducting Cyclotron Laboratory, Nucl Instrum Methods Phys Res A. 959 (2020) 163526. https://doi.org/10.1016/j.nima.2020.163526.

[49] M.D. Scott, J. Schorp, L. Sutherlin, J.D. Robertson, Isotope harvesting with Hollow Fiber Supported Liquid Membrane (HFSLM), Applied Radiation and Isotopes. 157 (2020) 109027. https://doi.org/10.1016/j.apradiso.2019.109027.

[50] C.S. Loveless, B.E. Marois, S.J. Ferran, J.T. Wilkinson, L. Sutherlin, G. Severin, J.A. Shusterman, N.D. Scielzo, M.A. Stoyer, D.J. Morrissey, J.D. Robertson, G.F. Peaslee, S.E. Lapi, Harvesting ^{48}V at the National Superconducting Cyclotron Laboratory, Applied Radiation and Isotopes. 157 (2020) 109023. https://doi.org/10.1016/j.apradiso.2019.109023.

[51] J. Fitzsimmons, L. Muench, C.S. Cutler, Fishing for Isotopes: Capturing Beryllium-7 from Brookhaven LINAC Isotope Producer's 300 gallons of Cooling Water, ACS Omega. 3 (2018) 3228–3234. https://doi.org/10.1021/acsomega.7b01757.

[52] T. Mastren, A. Pen, S. Loveless, B. V Marquez, E. Bollinger, B. Marois, N. Hubley, K. Brown, D.J. Morrissey, G.F. Peaslee, S.E. Lapi, Harvesting ^{67}Cu from the Collection of a Secondary Beam Cocktail at the National Superconducting Cyclotron Laboratory, Anal Chem. 87 (2015) 10323–10329. https://doi.org/10.1021/acs.analchem.5b02322.

[53] E.P. Abel, H.K. Clause, G.W. Severin, Radiolysis and radionuclide production in a flowing-water target during fast $^{40}Ca^{20+}$ irradiation., Applied Radiation and Isotopes. 158 (2020) 109049. https://doi.org/10.1016/j.apradiso.2020.109049.

[54] M. Avilov, A. Aaron, A. Amroussia, W. Bergez, C. Boehlert, T. Burgess, A. Carroll, C. Colin, F. Durantel, P. Ferrante, T. Fourmeau, V. Graves, C. Grygiel, J. Kramer, W. Mittig, I. Monnet, H. Patel, F. Pellemoine, R. Ronningen, M. Schein, Thermal, mechanical and fluid flow aspects of the high power beam dump for FRIB, Nucl Instrum Methods Phys Res B. 376 (2016) 24–27. https://doi.org/10.1016/j.nimb.2016.02.068.

[55] A. Pen, T. Mastren, G.F. Peaslee, K. Petrasky, P.A. DeYoung, D.J. Morrissey, S.E. Lapi, Design and construction of a water target system for harvesting radioisotopes at the National Superconducting Cyclotron Laboratory, Nucl Instrum Methods Phys Res A. 747 (2014) 62–68. https://doi.org/10.1016/j.nima.2014.02.010.

[56] A. Visser, N. Scielzo, Feasibility of Harvesting Radon from FRIB Beam Dump, Lawrence Livermore National Laboratory, Livermore, CA (United States), 2016. https://doi.org/10.2172/1346135.

[57] H.K. Clause, K.A. Domnanich, C. Kleinfeldt, M. Kalman, W. Walker, C. Vyas, E.P. Abel, G.W. Severin, Harvesting krypton isotopes from the off-gas of an irradiated water target to generate ^{76}Br and ^{77}Br, Sci Rep. 12 (2022) 1433. https://doi.org/10.1038/s41598-022-05500-8.

[58] S. Le Caër, Water Radiolysis: Influence of Oxide Surfaces on H_2 Production under Ionizing Radiation, Water (Basel). 3 (2011) 235–253. https://www.mdpi.com/2073-4441/3/1/235.

[59] J.A. LaVerne, Track Effects of Heavy Ions in Liquid Water, Radiat Res. 153 (2000) 487–496. http://www.jstor.org/stable/3580180.

[60] J.A. LaVerne, R.H. Schuler, W.G. Burns, Track effects in radiation chemistry: production of hydroperoxo radical within the track core in the heavy-particle radiolysis of water, J Phys Chem. 90 (1986) 3238–3242. https://doi.org/10.1021/j100405a037.

[61] M. Vankeerberghen, G. Weyns, S. Gavrilov, J. Henshaw, J. Deconinck, The electrochemistry in 316SS crevices exposed to PWR-relevant conditions, Journal of Nuclear Materials. 385 (2009) 517–526. https://doi.org/10.1016/j.jnucmat.2008.12.175.

[62] R. Sander, Compilation of Henry's law constants (version 4.0) for water as solvent, Atmos Chem Phys. 15 (2015) 4399–4981. https://doi.org/10.5194/acp-15-4399-2015.

[63] K.A. Domnanich, G.W. Severin, A Model for Radiolysis in a Flowing-Water Target during High-Intensity Proton Irradiation, ACS Omega. 7 (2022) 25860–25873. https://doi.org/10.1021/acsomega.2c03540.

[64] J. Meesungnoen, J.-P. Jay-Gerin, High-LET Radiolysis of Liquid Water with $^{1}H^{+}$, $^{4}He^{2+}$, $^{12}C^{6+}$, and $^{20}Ne^{9+}$ Ions: Effects of Multiple Ionization, J Phys Chem A. 109 (2005) 6406–6419. https://doi.org/10.1021/jp058037z.

[65] B. Pastina, J.A. LaVerne, Effect of Molecular Hydrogen on Hydrogen Peroxide in Water Radiolysis, J Phys Chem A. 105 (2001) 9316–9322. https://doi.org/10.1021/jp012245j.

[66] B. Pastina, J.A. LaVerne, Hydrogen Peroxide Production in the Radiolysis of Water with Heavy Ions, J Phys Chem A. 103 (1999) 1592–1597. https://doi.org/10.1021/jp984433o.

[67] J.R. Couper, W.R. Penney, J.R. Fair, S.M. Walas, 15 - Adsorption and Ion Exchange, in: J.R. Couper, W.R. Penney, J.R. Fair, S.M. Walas (Eds.), Chemical Process Equipment (Third Edition), Butterworth-Heinemann, Boston, 2012: pp. 529–559. https://doi.org/10.1016/B978-0-12-396959-0.00015-X.

[68] K.M. Krupka, D.I. Kaplan, G. Whelan, R.J. Serne, S. V Mattigod, N. p., Volume I: The K_d Model, Methods of Measurement, and Application of Chemical Reaction Codes, United States Environmental Protection Agency, United States, 1999.

[69] J. Korkisch, Handbook of Ion Exchange Resins: Their Applications to Inorganic Analytical Chemistry, 1st ed., CRC Press, Inc., Boca Raton, FL, 1989.

[70] F.G. Helfferich, Ion Exchange, McGraw-Hill, New York, 1962.

[71] P.M. Cummins, K.D. Rochfort, B.F. O'Connor, Ion-Exchange Chromatography: Basic Principles and Application, in: D. Walls, S.T. Loughran (Eds.), Protein Chromatography: Methods and Protocols, Springer New York, New York, NY, 2017: pp. 209–223. https://doi.org/10.1007/978-1-4939-6412-3_11.

[72] N. Takeno, Atlas of Eh-pH Diagrams. Intercomparison of thermodynamic databases, Geological Survey of Japan, 2005.

[73] K.A. Rubinson, I.M. Glynn, Concerning the form of biochemically active vanadium, Proc R Soc Lond B Biol Sci. 212 (1981) 65–84. https://doi.org/10.1098/rspb.1981.0025.

[74] G. Chen, H. Liu, Understanding the Reduction Kinetics of Aqueous Vanadium(V) and Transformation Products Using Rotating Ring-Disk Electrodes, Environ Sci Technol. 51 (2017) 11643–11651. https://doi.org/10.1021/acs.est.7b02021.

[75] S.D. Essenmacher, C.R. Kleinfeldt, K.A. Domnanich, V.S. Bodnar, C.K. Vyas, G.W. Severin, Proof-of-concept studies of novel protocols for producing highly pure ^{48}V from a ^{48}Cr/^{48}V generator, Applied Radiation and Isotopes. 199 (2023) 110855. https://doi.org/https://doi.org/10.1016/j.apradiso.2023.110855.

[76] Meeting Isotope Needs and Capturing Opportunities for the Future: The 2015 Long Range Plan for the DOE-NP Isotope Program, NSAC Isotopes Subcommittee, July 2015, (2015). https://www.osti.gov/biblio/1298983.

[77] S.M. Qaim, Use of cyclotrons in medicine, Radiation Physics and Chemistry. 71 (2004) 917–926. https://doi.org/10.1016/j.radphyschem.2004.04.124.

[78] J.F. Ziegler, M.D. Ziegler, J.P. Biersack, SRIM – The stopping and range of ions in matter (2010), Nucl Instrum Methods Phys Res B. 268 (2010) 1818–1823. https://doi.org/10.1016/j.nimb.2010.02.091.

[79] F. Ichikawa, S. Uruno, H. Imai, Distribution of Various Elements between Nitric Acid and Anion Exchange Resin, Bull Chem Soc Jpn. 34 (1961) 952–955. https://doi.org/10.1246/bcsj.34.952.

[80] K.A. Kraus, F. Nelson, Anion Exchange Studies of the Fission Products, in: R.A. Charpie, D.J. Dewar, A. Finkelstein, J. Gaunt, J.A. Goedkoop, E.O. Hughes, L.F. Lamerton, A. Milojević, C. Mosbacher, C.A. Sastre, B.E. Urquhart (Eds.), International Conference on the Peaceful Uses of Atomic Energy, United Nations, Geneva, 1955: pp. 113–125.

[81] T. Braun, G. Ghersini, eds., Extraction Chromatography, 1st ed., Elsevier Scientific Publishing Company, New York, 1975.

[82] T. Ishimori, E. Nakamura, Data of Inorganic Solvent Extraction. Part I, (1963). https://www.osti.gov/biblio/4715449.

[83] A. Pourmand, N. Dauphas, Distribution coefficients of 60 elements on TODGA resin: Application to Ca, Lu, Hf, U and Th isotope geochemistry, Talanta. 81 (2010) 741–753. https://doi.org/10.1016/j.talanta.2010.01.008.

[84] J. Thomson, Quench and Quench Curves, in: S. Möbius, J.E. Noakes, F. Schönhofer (Eds.), LSC 2001, Advances in Liquid Scintillation Spectrometry, Radiocarbon, 2002: pp. 65–73.

[85] L. Rodríguez Barquero, J.M. Los Arcos, F. Ortiz, A. Jiménez, ^{49}V Standardization by the CIEMAT/NIST LSC method, Applied Radiation and Isotopes. 49 (1998) 1077–1082. https://doi.org/10.1016/S0969-8043(97)10024-0.

[86] V.I.E. Bruyère, L.A. García Rodenas, P.J. Morando, M.A. Blesa, Reduction of vanadium(v) by oxalic acid in aqueous acid solutions, Journal of the Chemical Society, Dalton Transactions. (2001) 3593–3597. https://doi.org/10.1039/B103320B.

[87] R.I. Walter, Anion exchange studies of Sc(III) and V(IV). Separation of scandium, titanium and vanadium, Journal of Inorganic and Nuclear Chemistry. 6 (1958) 58–62. https://doi.org/10.1016/0022-1902(58)80100-1.

[88] J. Fons-Castells, V. Díaz, A. Badia, J. Tent-Petrus, M. Llauradó, Implications of quenching in efficiency, spectrum shape and alpha/beta separation, Applied Radiation and Isotopes. 128 (2017) 263–269. https://doi.org/10.1016/j.apradiso.2017.07.035.

[89] M. Takiue, Y. Matsui, H. Fujii, Activity determination of simultaneously chemical and color quenched samples using a liquid scintillation counter, Int J Rad Appl Instrum A. 42 (1991) 241–244. https://doi.org/10.1016/0883-2889(91)90083-D.

[90] R. Broda, P. Cassette, K. Kossert, Radionuclide metrology using liquid scintillation counting, Metrologia. 44 (2007) S36. https://doi.org/10.1088/0026-1394/44/4/S06.

[91] P. Cassette, R. Broda, D. Hainos, T. Terlikowska, Analysis of detection-efficiency variation techniques for the implementation of the TDCR method in liquid scintillation counting, Applied Radiation and Isotopes. 52 (2000) 643–648. https://doi.org/10.1016/S0969-8043(99)00224-9.

[92] O.B. Tarasov, D. Bazin, LISE++: Radioactive beam production with in-flight separators, Nucl Instrum Methods Phys Res B. 266 (2008) 4657–4664. https://doi.org/10.1016/j.nimb.2008.05.110.

[93] J.D. Burns, E.E. Tereshatov, G. Avila, K.J. Glennon, A. Hannaman, K.N. Lofton, L.A. McCann, M.A. McCarthy, L.A. McIntosh, S.J. Schultz, G.C. Tabacaru, A.L. Vonder Haar, S.J. Yennello, Rapid recovery of At-211 by extraction chromatography, Sep Purif Technol. 256 (2021) 117794. https://doi.org/10.1016/j.seppur.2020.117794.

[94] D.H. Woen, C. Eiroa-Lledo, A.C. Akin, N.H. Anderson, K.T. Bennett, E.R. Birnbaum, A.V. Blake, M. Brugh, E. Dalodière, E.F. Dorman, M.G. Ferrier, D.K. Hamlin, S.A. Kozimor, Y. Li, L.M. Lilley, V. Mocko, S.L. Thiemann, D.S. Wilbur, F.D. White, A Solid-State Support for Separating Astatine-211 from Bismuth, Inorg Chem. 59 (2020) 6137–6146. https://doi.org/10.1021/acs.inorgchem.0c00221.

[95] S. Shabbir, M. Hong, H. Rhee, Resin-supported palladium nanoparticles as recyclable catalyst for the hydrodechlorination of chloroarenes and polychlorinated biphenyls, Appl Organomet Chem. 31 (2017) e3552. https://doi.org/10.1002/aoc.3552.

[96] E.P. Horwitz, R. Chiarizia, M.L. Dietz, H. Diamond, D.M. Nelson, Separation and preconcentration of actinides from acidic media by extraction chromatography, Anal Chim Acta. 281 (1993) 361–372. https://doi.org/10.1016/0003-2670(93)85194-O.

[97] P.W. Lisowski, C.D. Bowman, G.J. Russell, S.A. Wender, The Los Alamos National Laboratory Spallation Neutron Sources, Nuclear Science and Engineering. 106 (1990) 208–218. https://doi.org/10.13182/NSE90-A27471.

[98] S.A. Kuvin, H.Y. Lee, B. DiGiovine, A. Georgiadou, S. Mosby, D. Votaw, M. White, L. Zavorka, Validation of neutron-induced reactions on natural carbon using an active target at neutron energies up to 22 MeV at LANSCE, Phys. Rev. C. 104 (2021) 14603. https://doi.org/10.1103/PhysRevC.104.014603.

[99] S.A. Kuvin, H.Y. Lee, T. Kawano, B. DiGiovine, A. Georgiadou, C. Vermeulen, M. White, L. Zavorka, H.I. Kim, Nonstatistical fluctuations in the ^{35}Cl(n,p)^{35}S reaction cross section at fast-neutron energies from 0.6 to 6 MeV, Phys Rev C. 102 (2020) 24623. https://doi.org/10.1103/PhysRevC.102.024623.

[100] H.Y. Lee, S. Mosby, R.C. Haight, M.C. White, ^{16}O(n,α) cross section investigation using LENZ instrument at LANSCE, EPJ Web Conf. 122 (2016) 5004. https://doi.org/10.1051/epjconf/201612205004.

[101] S.A. Kuvin, H.Y. Lee, B. DiGiovine, C. Eiroa-Lledo, A. Georgiadou, M. Herman, T. Kawano, V. Mocko, S. Mosby, C. Vermeulen, D. Votaw, M. White, L. Zavorka, G. Perdikakis, P. Tsintari, H.I. Kim, Direct measurement of ^{59}Ni(n,p)^{59}Co and ^{59}Ni(n,α)^{56}Fe at fast-neutron energies from 500 keV to 10 MeV, Phys. Rev. C. 105 (2022) 44608. https://doi.org/10.1103/PhysRevC.105.044608.

[102] T. Kawano, T. Sanami, M. Baba, H. Nakashima, Analysis of ^{58}Ni(n, α) Reaction Cross Sections with the Hauser-Feshbach Statistical Theory and the Bayesian Parameter Estimation Method, J Nucl Sci Technol. 36 (1999) 256–264. https://doi.org/10.1080/18811248.1999.9726206.

[103] H.I. Kim, H.Y. Lee, T. Kawano, A. Georgiadou, S.A. Kuvin, L. Zavorka, M.W. Herman, New evaluation on angular distributions and energy spectra for neutron-induced charged-particle measurements, Nucl Instrum Methods Phys Res A. 963 (2020) 163699. https://doi.org/10.1016/j.nima.2020.163699.

[104] A. Stolarz, Target preparation for research with charged projectiles, J Radioanal Nucl Chem. 299 (2014) 913–931. https://doi.org/10.1007/s10967-013-2652-2.

[105] A.H.F. Muggleton, Deposition techniques for the preparation of thin film nuclear targets, Vacuum. 37 (1987) 785–817. https://doi.org/10.1016/0042-207X(87)90180-1.

[106] S. Bjørnholm, J. Borggreen, L. Westgaard, V.A. Karnaukhov, Excitation energy of the spontaneously fissioning isomeric state in ^{240}Am, Nucl Phys A. 95 (1967) 513–525. https://doi.org/10.1016/0375-9474(67)90846-9.

[107] L. Yaffe, Preparation of thin Films, Sources, and Targets, Annu Rev Nucl Sci. 12 (1962) 153–188. https://doi.org/10.1146/annurev.ns.12.120162.001101.

[108] S. Heinitz, E.A. Maugeri, D. Schumann, R. Dressler, N. Kivel, C. Guerrero, U. Köster, M. Tessler, M. Paul, S. Halfon, the n_TOF Collaboration, Production, separation and target preparation of ^{171}Tm and ^{147}Pm for neutron cross section measurements, Radiochim Acta. 105 (2017) 801–811. https://doi.org/doi:10.1515/ract-2016-2728.

[109] C. Guerrero, J. Lerendegui-Marco, M. Paul, M. Tessler, S. Heinitz, C. Domingo-Pardo, S. Cristallo, R. Dressler, S. Halfon, N. Kivel, U. Köster, E.A. Maugeri, T. Palchan-Hazan, J.M. Quesada, D. Rochman, D. Schumann, L. Weissman, O. Aberle, S. Amaducci, J. Andrzejewski, L. Audouin, V. Bécares, M. Bacak, J. Balibrea, A. Barak, M. Barbagallo, S. Barros, F. Bečvář, C. Beinrucker, D. Berkovits, E. Berthoumieux, J. Billowes, D. Bosnar, M. Brugger, Y. Buzaglo, M. Caamaño, F. Calviño, M. Calviani, D. Cano-Ott, R. Cardella, A. Casanovas, D.M. Castelluccio, F. Cerutti, Y.H. Chen, E. Chiaveri, N. Colonna, G. Cortés, M.A. Cortés-Giraldo, L. Cosentino, H. Dafna, A. Damone, M. Diakaki, M. Dietz, E. Dupont, I. Durán, Y. Eisen, B. Fernández-Domínguez, A. Ferrari, P. Ferreira, P. Finocchiaro, V. Furman, K. Göbel, A.R. García, A. Gawlik, T. Glodariu, I.F. Gonçalves, E. González-Romero, A. Goverdovski, E. Griesmayer, F. Gunsing, H. Harada, T. Heftrich, J. Heyse, T. Hirsh, D.G. Jenkins, E. Jericha, F. Käppeler, Y. Kadi, B. Kaizer, T. Katabuchi, P. Kavrigin, V. Ketlerov, V. Khryachkov, D. Kijel, A. Kimura, M. Kokkoris, A. Kriesel, M. Krtička, E. Leal-Cidoncha, C. Lederer-Woods, H. Leeb, S. Lo Meo, S.J. Lonsdale, R. Losito, D. Macina, A. Manna, J. Marganiec, T. Martínez, C. Massimi, P. Mastinu, M. Mastromarco, F. Matteucci, E. Mendoza, A. Mengoni, P.M. Milazzo, M.A. Millán-Callado, F. Mingrone, M. Mirea, S. Montesano, A. Musumarra, R. Nolte, A. Oprea, N. Patronis, A. Pavlik, J. Perkowski, L. Piersanti, I. Porras, J. Praena, K. Rajeev, T. Rauscher, R. Reifarth, T. Rodríguez-González, P.C. Rout, C. Rubbia, J.A. Ryan, M. Sabaté-Gilarte, A. Saxena, P. Schillebeeckx, S. Schmidt, A. Shor, P. Sedyshev, A.G. Smith, A. Stamatopoulos, G. Tagliente, J.L. Tain, A. Tarifeño-Saldivia, L. Tassan-Got, A. Tsinganis, S. Valenta, G. Vannini, V. Variale, P. Vaz, A. Ventura, V. Vlachoudis, R. Vlastou, A. Wallner, S. Warren, M. Weigand, C. Weiss, C. Wolf, P.J. Woods, T. Wright, P. Žugec, Neutron Capture on the *s*-Process Branching Point ^{171}Tm via Time-of-Flight and Activation, Phys. Rev. Lett. 125 (2020) 142701. https://doi.org/10.1103/PhysRevLett.125.142701.

[110] C. Guerrero, M. Tessler, M. Paul, J. Lerendegui-Marco, S. Heinitz, E.A. Maugeri, C. Domingo-Pardo, R. Dressler, S. Halfon, N. Kivel, U. Köster, T. Palchan-Hazan, J.M. Quesada, D. Schumann, L. Weissman, The *s*-process in the Nd-Pm-Sm region:

Neutron activation of ^{147}Pm, Physics Letters B. 797 (2019) 134809. https://doi.org/10.1016/j.physletb.2019.134809.

[111] D.C. Aumann, G. Müllen, Preparation of targets of Ca, Ba, Fe, La, Pb, Tl, Bi, Th and U by electrodeposition from organic solutions, Nuclear Instruments and Methods. 115 (1974) 75–81. https://doi.org/10.1016/0029-554X(74)90427-3.

[112] F.A. Buford, J.H. Freeman, J.B. Reynolds, Electroplated isotopic targets, 1966.

[113] W. Parker, H. Bildstein, N. Getoff, Molecular plating I, a rapid and quantitative method for the electrodeposition of thorium and uranium, Nuclear Instruments and Methods. 26 (1964) 55–60. https://doi.org/10.1016/0029-554X(64)90049-7.

[114] S. Dede, S.D. Essenmacher, P. Gastis, K. V Manukyan, S.A. Kuvin, H.Y. Lee, J.M. Roach, P.C. Burns, A. Aprahamian, Electrospraying deposition and characterization of potassium chloride targets for nuclear science measurements, Nucl Instrum Methods Phys Res A. (2023) 168472. https://doi.org/10.1016/j.nima.2023.168472.

[115] E.A. Maugeri, S. Heinitz, R. Dressler, M. Barbagallo, N. Kivel, D. Schumann, M. Ayranov, A. Musumarra, M. Gai, N. Colonna, M. Paul, S. Halfon, L. Cosentino, P. Finocchiaro, A. Pappalardo, Preparation of ^{7}Be targets for nuclear astrophysics research, Journal of Instrumentation. 12 (2017) P02016. https://doi.org/10.1088/1748-0221/12/02/P02016.

[116] R. Haas, S. Lohse, C.E. Düllmann, K. Eberhardt, C. Mokry, J. Runke, Development and characterization of a Drop-on-Demand inkjet printing system for nuclear target fabrication, Nucl Instrum Methods Phys Res A. 874 (2017) 43–49. https://doi.org/10.1016/j.nima.2017.08.027.

[117] M. Weigand, T. Heftrich, Ch.E. Düllmann, K. Eberhardt, S. Fiebiger, J. Glorius, K. Göbel, R. Haas, C. Langer, S. Lohse, R. Reifarth, D. Renisch, C. Wolf, 66.7-keV γ-line intensity of ^{171}Tm determined via neutron activation, Phys. Rev. C. 97 (2018) 35803. https://doi.org/10.1103/PhysRevC.97.035803.

[118] D. Mampallil, H.B. Eral, A review on suppression and utilization of the coffee-ring effect, Adv Colloid Interface Sci. 252 (2018) 38–54. https://doi.org/10.1016/j.cis.2017.12.008.

[119] D. Lohse, Fundamental Fluid Dynamics Challenges in Inkjet Printing, Annu Rev Fluid Mech. 54 (2022) 349–382. https://doi.org/10.1146/annurev-fluid-022321-114001.

[120] H. Wijshoff, The dynamics of the piezo inkjet printhead operation, Phys Rep. 491 (2010) 77–177. https://doi.org/10.1016/j.physrep.2010.03.003.

[121] M.-H. Bai, T.-Y. Liu, F. Luan, Y. Li, X.-X. Liu, Electrodeposition of vanadium oxide–polyaniline composite nanowire electrodes for high energy density supercapacitors, J Mater Chem A Mater. 2 (2014) 10882–10888. https://doi.org/10.1039/C3TA15391F.

[122] K. Takahashi, S.J. Limmer, Y. Wang, G. Cao, Synthesis and Electrochemical Properties of Single-Crystal V_2O_5 Nanorod Arrays by Template-Based Electrodeposition, J Phys Chem B. 108 (2004) 9795–9800. https://doi.org/10.1021/jp0491820.

[123] A. Afkhami, B.E. Conway, Investigation of Removal of Cr(VI), Mo(VI), W(VI), V(IV), and V(V) Oxy-ions from Industrial Waste-Waters by Adsorption and Electrosorption at High-Area Carbon Cloth, J Colloid Interface Sci. 251 (2002) 248–255. https://doi.org/10.1006/jcis.2001.8157.

[124] J.R. Pretty, E.A. Blubaugh, J.A. Caruso, T.M. Davidson, Determination of Chromium(VI) and Vanadium(V) Using an Online Anodic Stripping Voltammetry Flow Cell with Detection by Inductively Coupled Plasma Mass Spectrometry, Anal Chem. 66 (1994) 1540–1547. https://doi.org/10.1021/ac00081a029.

[125] G. Steinhauser, S. Merz, F. Stadlbauer, P. Kregsamer, C. Streli, M. Villa, Performance and comparison of gold-based neutron flux monitors, Gold Bull. 45 (2012) 17–22. https://doi.org/10.1007/s13404-011-0039-0.

[126] A.J. Bard, L.R. Faulkner, Electrochemical Methods: Fundamentals and Applications, 2nd Edition, Wiley Textbooks, 2000. https://books.google.com/books?id=hQocAAAAQBAJ.

[127] M. Doerre, L. Hibbitts, G. Patrick, N.K. Akafuah, Advances in Automotive Conversion Coatings during Pretreatment of the Body Structure: A Review, Coatings. 8 (2018). https://doi.org/10.3390/coatings8110405.

[128] D.R. Lide, CRC Handbook of Chemistry and Physics, 85th ed., CRC Press, Boca Raton, FL, 2005.

[129] H. Guan, R.G. Buchheit, Corrosion Protection of Aluminum Alloy 2024-T3 by Vanadate Conversion Coatings, Corrosion. 60 (2004) 284–296. https://doi.org/10.5006/1.3287733.

[130] R.C. Furneaux, G.E. Thompson, G.C. Wood, An electronoptical study of the conversion coating formed on aluminium in a chromate/fluoride solution, Corros Sci. 19 (1979) 63–71. https://doi.org/https://doi.org/10.1016/0010-938X(79)90031-3.

[131] J. Sudagar, J.S. Lian, Y.Q. Liang, J.A. Liu, Electroless Ni–P deposition with vanadium based coating as pretreatment on AZ91D magnesium alloy, Transactions of the IMF. 90 (2012) 129–136. https://doi.org/10.1179/0020296712Z.00000000022.

[132] J. Mendialdua, R. Casanova, Y. Barbaux, XPS studies of V_2O_5, V_6O_{13}, VO_2 and V_2O_3, J Electron Spectros Relat Phenomena. 71 (1995) 249–261. https://doi.org/10.1016/0368-2048(94)02291-7.

[133] R. Lindström, V. Maurice, S. Zanna, L. Klein, H. Groult, L. Perrigaud, C. Cohen, P. Marcus, Thin films of vanadium oxide grown on vanadium metal: oxidation conditions to produce

V_2O_5 films for Li-intercalation applications and characterisation by XPS, AFM, RBS/NRA, Surface and Interface Analysis. 38 (2006) 6–18. https://doi.org/10.1002/sia.2141.

[134] B. Demri, D. Muster, XPS study of some calcium compounds, J Mater Process Technol. 55 (1995) 311–314. https://doi.org/10.1016/0924-0136(95)02023-3.

[135] H. Hu, R.G. Larson, Marangoni Effect Reverses Coffee-Ring Depositions, J Phys Chem B. 110 (2006) 7090–7094. https://doi.org/10.1021/jp0609232.

[136] V. Soulié, Sessile Droplets of Salt Solutions on Inert and Metallic Surfaces : Influence of Salt Concentration Gradients on Evaporation and Corrosion Behaviour, Université Montpellier ; Universität Potsdam, 2015. https://theses.hal.science/tel-01992174.

[137] N. Shahidzadeh, M.F.L. Schut, J. Desarnaud, M. Prat, D. Bonn, Salt stains from evaporating droplets, Sci Rep. 5 (2015) 10335. https://doi.org/10.1038/srep10335.

[138] J. Chen, B. Singh, Nuclear Data Sheets for A=50, Nuclear Data Sheets. 157 (2019) 1–259. https://doi.org/10.1016/j.nds.2019.04.001.

APPENDIX

A.1 Ultraviolet-Visible Spectroscopy of Cr and V in pH 8 Electrodeposition Solutions

Ultraviolet-visible (UV-Vis) spectroscopy was performed on 1 ppm Cr and 1 ppm V solutions prepared under N_2 atmosphere according to the procedure for the preparation of the 1 ppm V solutions in Section 4.3.1.1 with the substitution of an aliquot of the 3250(50) ppm Cr solution for the 7700(200) ppm V solution described in Section 2.3.1 and the addition of an equilibration time of 1 week. The obtained spectra were compared to UV-Vis spectra obtained for a freshly prepared 1 ppm Cr and 1 ppm V solution in absence of N_2 gas and freshly prepared 1 ppm Cr and 1 ppm V solutions made with diluted ICP standards (for samples that contain mostly Cr(III) and V(IV) respectively). The V concentration was too low to observe any peaks in their spectra; however, Cr could be detected and those results are shown in Figure A.1. The results from this study suggest that if Cr were in the electrodeposition solutions, then most of the Cr would be Cr(VI) for the deposition experiment because of the 7-day delay prior to the start of deposition. By extension, V would be primarily V(V) in the same solutions at the start of the deposition because the aqueous chemistry between Cr(VI) and Cr(III) is very similar to the aqueous chemistry between V(V) and V(IV) in pH 8 solutions [72].

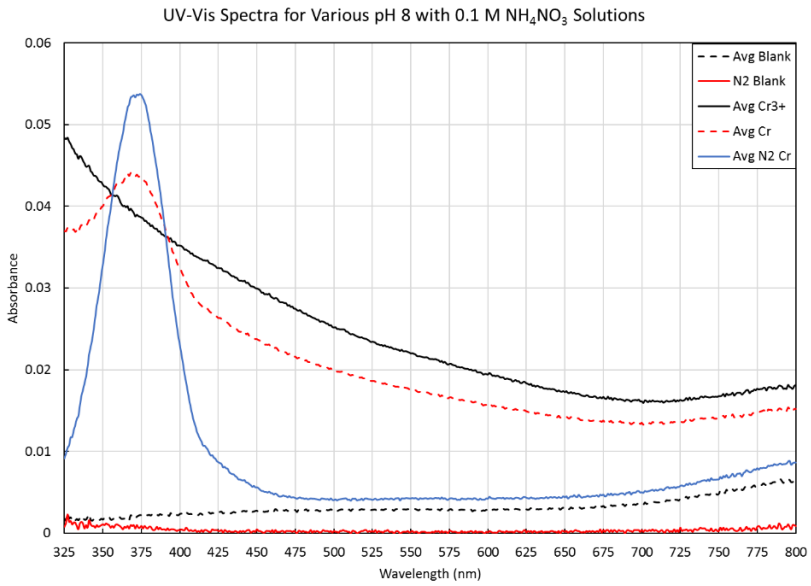

Figure A.1: UV-Vis spectra of 1 ppm Cr in 0.1 M NH_4NO_3 pH 8 solutions. Note that N2 denotes solutions that were prepared under purging with N_2 gas, allowed to equilibrate over 7 days in a vial, and were purged with N_2 again for 2 minutes prior to being measured.

A.2 Additional X-Ray Photoelectron Spectroscopy Images

The full window for the XPS spectra shown in Figure 4.8 can be seen in Figure A.2 on the next page. In addition to the peaks associated with V-O bonds and the O 1s peaks, there are some peaks associated with Ca-O bonds and a C 1s peak.

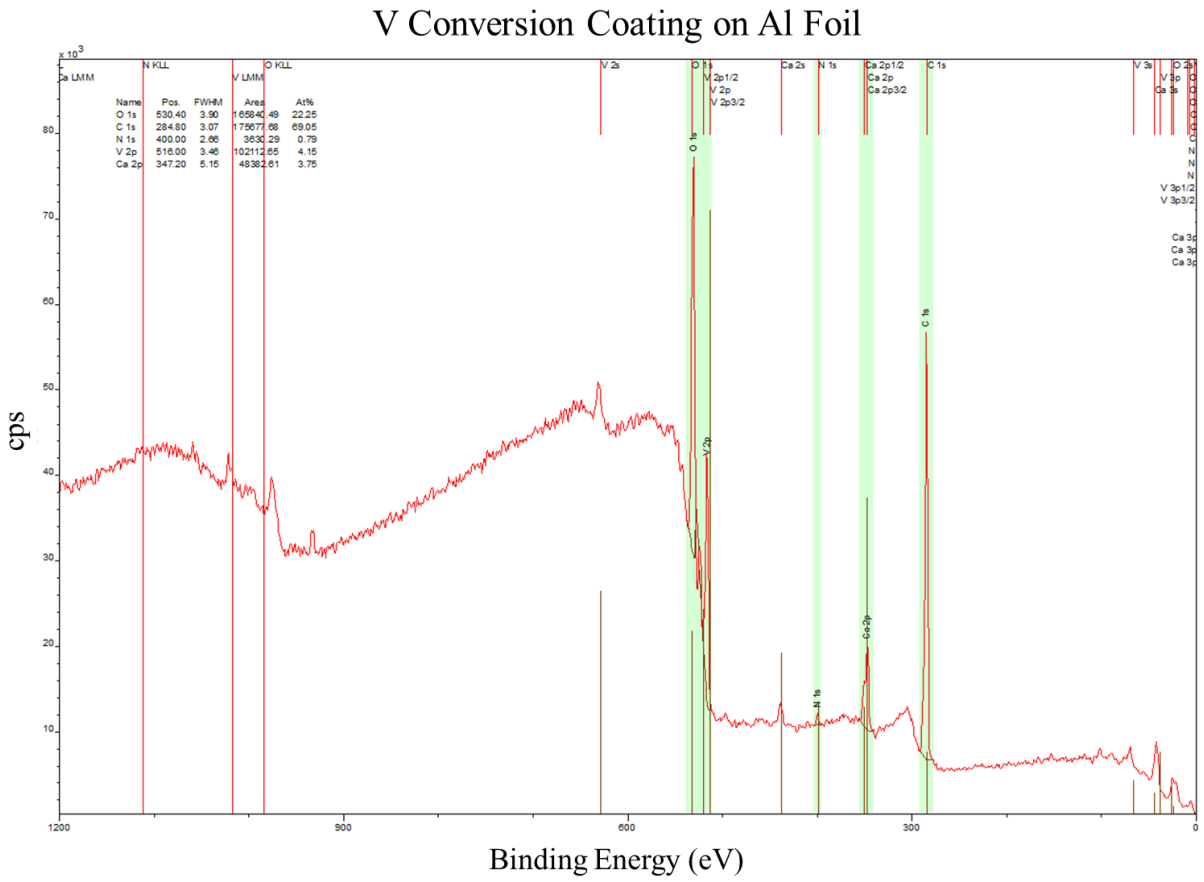

Figure A.2: X-ray photoelectron spectroscopy results for a V conversion coating on Al target fabricated at MSU. This target appears to have Ca and C as impurities.